Optical Transmission Systems based on the Nonlinear Fourier Transformation

Dissertation

zur Erlangung des akademischen Grades
Doktor der Ingenieurwissenschaften
(Dr.-Ing.)
der Christian-Albrechts-Universität zu Kiel

vorgelegt von
Jonas Koch
aus
Uelzen

Jahr
2022

1. Gutachter:	Prof. Dr.-Ing. Dipl.-Wirt. Ing. Stephan Pachnicke
2. Gutachter:	Univ.-Prof. Dr.-Ing. Christian G. Schäffer
Tag der mündlichen Prüfung:	18. November 2022

Vorwort

Die in dieser Dissertation vorgestellten Ergebnisse entstanden während meiner Arbeit am Lehrstuhl für Nachrichtenübertragungstechnik, beginnend mit der Masterarbeit im Mai 2017. Dies wurde fortgeführt im Rahmen meiner Anstellung als wissenschaftlicher Mitarbeiter im DFG Projekt „Nonlinear Fourier Transform based Optical Transmission using Electronic-Photonic Signal Processing“ im Rahmen des SPP 2111 „Electronic-Photonic Integrated Systems for Ultrafast Signal Processing“. Dafür möchte ich mich zuerst bei Herrn Prof. Pachnicke bedanken, der mir ermöglicht hat, dieses Thema an seinem Lehrstuhl zu bearbeiten und dabei immer ein offenes Ohr nicht nur für fachliche Themen hatte und mich während der Erstellung dieser Dissertation und der Arbeit im Projekt betreut hat. Mein weiterer Dank gilt Herrn Prof. Schäffer für die Erstellung des zweiten Gutachtens, aber auch für fruchtbare Diskussionen schon während gemeinsamen Veröffentlichungen und auf Konferenzen. Außerdem möchte ich mich bei Herrn Prof. Höher und Herrn Prof. Meurer bedanken, die die Prüfungskommission vervollständigt und eine gerechte mündliche Prüfung ermöglicht haben.

Ein besonderer Dank gilt aber auch allen KollegInnen innerhalb des Projektes von der RWTH Aachen. Allen voran Herrn Dr.-Ing. Alvaro Moscoso Mártir und Herrn Prof. Witzens. All dies wäre ohne diese enge und produktive Zusammenarbeit bei Projekttreffen, der Erstellung von Manuskripten und im Labor nicht möglich gewesen.

All meinen KollegInnen, die mich auf diesem Weg begleitet haben gilt auch mein Dank: Dennis, der mir die Tür zum Lehrstuhl geöffnet hat. Shi, der mit mir gemeinsam begonnen hat die NFT zu verstehen. Simon, mit dem ich viele interessante Gespräche in vielen Büro-, Labor-, Konferenz- und Abendstunden im gesamten Fachbereich der Nachrichtentechnik führen durfte (und natürlich für das Korrekturlesen). Olaf, für die gemeinsame Arbeit an der NFT und die Korrekturen an dieser Dissertation. Sebastian für die Hilfe beim Verstehen von neuronalen Netzen. Adrian, Lars, Mihail, Petra, Rebekka, Sandra, Tom für viele gemeinsame Stunden und Gespräche bei Kaffee und Grillen am Lehrstuhl.

Ein ganz besonderes Danke an meine Eltern, die mich von Beginn an nicht nur seelisch unterstützt, sondern auch schon vor dem Studium machen lassen haben.

Und zuletzt, doch eigentlich zuerst möchte ich mich bei Rebekka bedanken. Du und Magdalene habt mir den Rücken gestärkt und mir in nicht immer leichten Zeiten geholfen, geduldig gewartet und mich immer ausgehalten, mir Zeit geschenkt und so viel ermöglicht.

Abstract

For modern data links with high data rates, optical fibers are used, which are particularly characterized by their high usable bandwidth combined with low attenuation. Thus, with the help of dense wavelength multiplexing, a high number of channels can be transmitted over long distances on a bandwidth of more than 11.4 THz.

To keep spectral efficiency as high as possible over this bandwidth, a highly granular modulation format is also required in addition to said dense multiplexing. However, as the transmission distance increases, so does the noise power, which makes it necessary to use higher and higher transmission powers to be able to transmit high-level modulation formats.

But this is hindered by the inherent nonlinearity of the fiber-optic channel. Thus, as signal powers increase, so do the nonlinear interferences, which ultimately limits the transmit power in turn the maximum spectral efficiency. It is therefore necessary to control the influence of these nonlinearities.

One approach, which was already pursued in the 1980s and 1990s, was the use of so-called solitons. Solitons are stable pulse shapes, which propagate linearly and maintain their shape despite the highly nonlinear channel. A challenge in the use of these signal pulses in optical data transmission is to multiplex them with high efficiency.

One way to multiplex many solitons is the nonlinear Fourier transform (NFT). With the help of the NFT, signal spectra can be calculated which propagate linearly through a nonlinear channel. Thus, in perspective, it is possible to perform linear transmissions even in highly nonlinear regions with high signal power levels. The NFT decomposes a signal into a dispersive and a solitonic part. The dispersive part is similar to spectra of the conventional linear Fourier transform and dominates especially at low signal powers. As soon as the total power of a signal exceeds a certain limit, solitons arise.

A disadvantage of solitons generated digitally by the NFT is their complex shape due to, for example, high electrical bandwidths or a poor peak-to-average power ratio.

In the course of this work, a scalable system architecture of a photonic integrated circuit based on a silicon chip was designed, which allows to multiplex several simple solitons tightly together to push the complex electrical generation of higher order solitons into the optical domain. This photonic integrated circuit was subsequently designed and fabricated by the Institute of Integrated Photonics at RWTH Aachen University.

Using this novel system architecture and additional equalization concepts designed in this work, soliton transmissions with up to four channels could be successfully realized over more than 5000 km with a very high spectral efficiency of 0.5 b/s/Hz in the soliton range.

Kurzfassung

Für moderne Datenverbindungen mit hohen Datenraten werden Glasfasern verwendet, die sich besonders durch ihre hohe nutzbare Bandbreite bei gleichzeitig niedriger Dämpfung auszeichnen. So können mit Hilfe von dichtem Wellenlängenmultiplexing eine hohe Anzahl an Kanälen auf einer Bandbreite von mehr als 11,4 THz über Weitverkehrsdistanzen übertragen werden.

Um die spektrale Effizienz über diese Bandbreite möglichst hoch zu halten, ist neben besagtem dichtem Multiplexing außerdem ein feingranulares Modulationsformat nötig. Da mit steigender Übertragungsdistanz jedoch auch die Rauschleistung steigt, ist es nötig, immer höhere Sendeleistungen zu nutzen, um diese hochstufigen Modulationsformate empfangen zu können.

Dies wird jedoch durch die inhärente Nichtlinearität des faseroptischen Kanals behindert. Mit steigenden Signalleistungen steigen so auch die nichtlinearen Störungen. Dadurch werden schlussendlich die Sendeleistung und die maximale spektrale Effizienz begrenzt. Es ist daher nötig, den Einfluss dieser Nichtlinearitäten zu beherrschen.

Ein Ansatz, der bereits in den 1980er und 1990er Jahren verfolgt wurde, war der Einsatz von sogenannten Solitonen. Stabile Pulsformen, die sich trotz des hoch nichtlinearen Kanals linear ausbreiten und ihre Form aufrechterhalten, kennzeichnen Solitonen. Eine Herausforderung bei der Nutzung dieser Signalpulse in der optischen Datenübertragung ist es, diese hocheffizient zu multiplexen.

Eine Möglichkeit viele Solitonen zu multiplexen, ist die nichtlineare Fouriertransformation (NFT). Mit Hilfe der NFT lassen sich Signalspektren berechnen, welche sich linear durch einen nichtlinearen Kanal ausbreiten. So ist es perspektivisch möglich, auch in hoch nichtlinearen Bereichen mit hoher Signalleistung lineare Übertragungen durchzuführen. Die NFT zerlegt ein Signal in einen dispersiven und einen solitonischen Anteil. Der dispersive Anteil ist ähnlich zu Spektren der herkömmlichen, linearen Fouriertransformation und dominiert besonders bei niedrigen Signalleistungen. Sobald die Gesamtleistung eines Signals eine bestimmte Grenze überschreitet entstehen die Solitonen.

Ein Nachteil von digital durch die NFT erzeugten Solitonen ist ihre komplexe Form aufgrund der hohen elektrischen Bandbreiten oder einem schlechten Verhältnis von Spitzen- zu Durchschnittsleistung.

Im Laufe dieser Arbeit wurde eine skalierbare Systemarchitektur eines photonischen integrierten Schaltkreises auf Basis eines Siliziumchips entworfen, die es ermöglicht, mehrere einfache Solitonen eng miteinander zu multiplexen, um so die komplexe elektrische Erzeugung von Solitonen höherer Ordnung in die optische Domäne zu verlagern. Dieser Chip wurde anschließend vom Lehrstuhl für integrierte Photonik der RWTH Aachen entworfen und hergestellt.

Mit Hilfe dieser Systemarchitektur und zusätzlich in dieser Arbeit entwickelten Entzerrungskonzepten konnten Solitonübertragungen mit bis zu vier Kanälen mit einer im Solitonbereich sehr hohen spektralen Effizienz von 0,5 b/s/Hz über mehr als 5000 km erfolgreich realisiert werden.

Table of Contents

Chapter 1

Introduction

1.1 Development of Optical Communications

Fiber optic transmissions were first proposed and theoretically and experimentally conceived by Charles K. Kao in 1966 [1]. This can be seen as the early birth of an innovative and rapid development that led to the first fiber optic transmissions in 1978 [2]. In the early phases of fiber optic development, the focus was on minimizing fiber attenuation in order to increase amplifier distances. To amplify the optical signals, electrical amplifiers were initially used, which required an optical-electrical and vice versa conversion. Thus, the usable bandwidth in optical systems was limited by the electrical components. It was not until the discovery of optical amplifiers such as the Erbium-doped fiber amplifier (EDFA) in 1987 that the large available bandwidth in optical fiber could be used. This led to the first commercial wavelength division multiplexing (WDM) system in 1989 [3] (using two carriers) and impactful work in the scope of WDM in 1992 [2] and the first WDM systems with more than two carriers in 1995 [2] and up to 160 carriers in 2000 with also automatic reconfigurability using optical add-drop multiplexers (OADM). Hence, in combination with other inventions, the transmission rates of commercial systems doubled annually in the 1990s to 2000s [3]. Coherent detection then led since 2007 to the fact that not only the intensity, but also the phase as well as the polarization could be used as a degrees freedom, which leads us to our current transmission systems.

1.2 Motivation

Current transmission networks show exponential growth with estimated compound annual growth rates (CAGR) of 26 % [4] (Fig. 1.1) to 60 % [5] per year. This is characterised by almost daily record throughputs in internet hubs such as DE-CIX in Frankfurt as shown in Fig. 1.2.

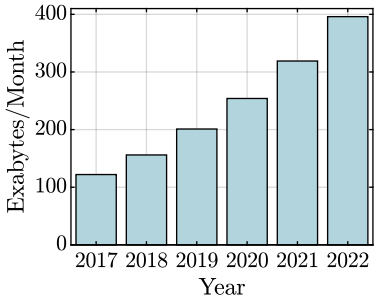

Figure 1.1: Global IP traffic growth [4].

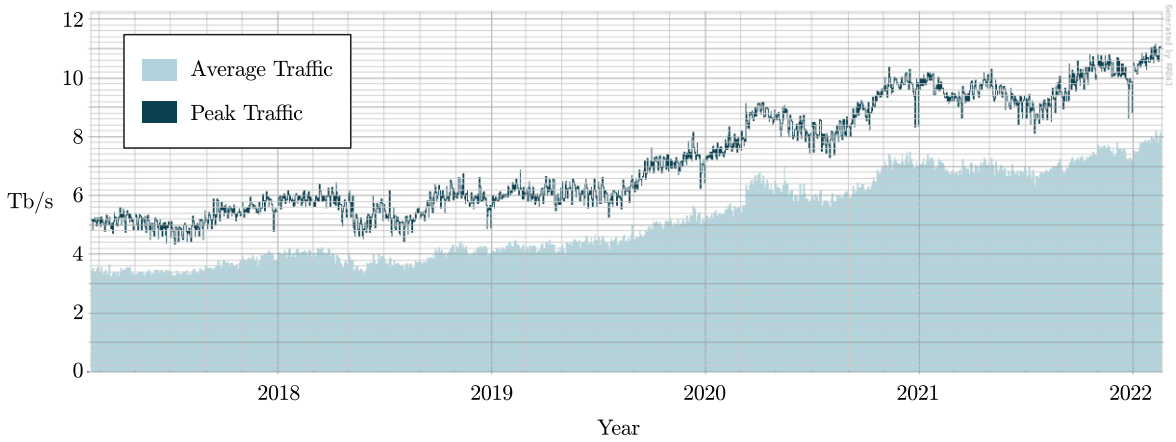

Figure 1.2: Traffic exchange at the internet exchange point DE-CIX in Frankfurt [6]. Copyright: DE-CIX Management GmbH.

1.2.1 Exponential Growth

In order to meet the exponential increase in demand for IT-supported communication, the capacity of transmission networks must grow exponentially in accordance to the speeds of electrical interfaces, devices and computing power. This technological scaling is conservatively estimated in the range of 40 % per year, while the scaling of optical interfaces and channel capacities is growing at only about 20 % [3][7] (Fig. 1.3a). Various approaches are proposed to increase this growth. One promising approach is space-division multiplexing (SDM)[3][8]. While the dimensions of time, quadrature, polarization and frequency have already been exhausted, the dimension of space is currently hardly used. So one approach is to deploy multi-core fibers, where the use of parallel spatial paths complements wavelength scalability (WDM). However, all approaches sooner or later run into the so-called non-linear Shannon capacity limit.

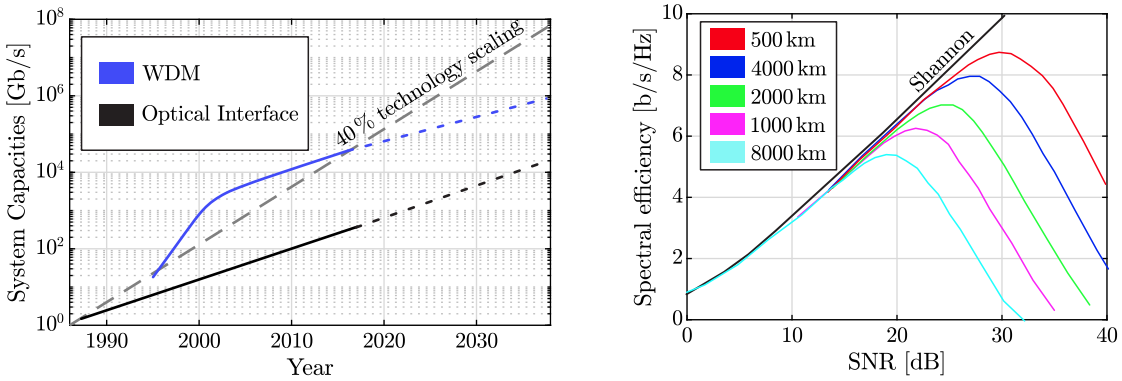

(a) Evolution of commercial optical systems and extrapolation for the coming years [3][7].

(b) Spectral efficiency after transmission for various distances.[9].

Figure 1.3: Development of commercial optical systems and one of the reasons for the relatively slow development. By increasing the transmit power, non-linearities lead to a reduction in efficiency despite increased SNR.

1.2.2 Capacity Limit

The conventional, linear Shannon limit describes the maximum capacity of a linear channel as a function of the signal-to-noise ratio (SNR). However, this can only be applied to the optical channel for low transmission powers, as the optical fiber is a non-linear medium. Thus, non-linear interferences prevent a further increase of the capacity along the linear Shannon limit and eventually even cause a drop of the capacity if the non-linear interferences are not compensated [9], as shown in Fig. 1.3b. In [9], five WDM channels were modulated using an APSK modulated sinc signal (ideal rectangular spectrum) with 16 amplitude levels. The number of points per ring was varied to change the spectral efficiency. It can be seen that above a certain SNR, the spectral efficiency no longer follows the linear efficiency limit. It can clearly be seen that this is also dependent on the transmission distance and thus the accumulated non-linearity. Hence, the SNR at which the capacity is highest decreases by 3 dB when the distance is doubled. In order to stay close to the linear Shannon limit, it is necessary to compensate for the emerging non-linearities, especially for long transmission distances.

One approach used in the past are solitons. Solitons can play off properties of the optical channel such as dispersion and nonlinearities to maintain their shape even at higher transmit powers. However, one disadvantage of solitons is their intrinsically low spectral efficiency, which is why research has turned away from them. A relatively new approach, however, is the so-called nonlinear Fourier transform (NFT)[10][11]. The NFT can decompose any signals into solitonic and dispersive components, which propagate linearly through the nonlinear channel. It has been shown that at high transmission

powers, a large proportion of the signal energy is solitonic in nature [12], and so signals with high transmission power are in fact made up of many superimposed solitons. Thus, with the help of solitons and the NFT, it may be possible to overcome the non-linear capacity limit and comply with exponential traffic growth.

The aim of this work is to show how soliton transmissions can be used and potentially improved in the NFT framework to eventually enable spectral efficiencies even in high power ranges.

1.3 Outline

This work is organized as follows: besides the introduction, there are six other chapters in this thesis. In chapter two, the optical transmission channel including optical transmission and reception concepts will be explained. Special attention will be paid to the fiber and the solitons and their physical background. Chapter three explains the mathematical concept of NFT. Subsequently, in chapter four, solitons in the framework of NFT will be explained. Possibilities to modulate and demodulate solitons with the help of NFT will be shown. This will be extended with multiplexing methods, which include digital, non-linear multiplexing as well as linear multiplexing. Chapter five shows possibilities to equalize solitons with the help of NFT and new digital equalizers and thus make them more robust against interfering channel influences and noise. Chapter six introduces electronic-photonic signal processing and shows how it can be used to create complex solitons to achieve high spectral efficiencies on scalable bandwidths to reach record spectral efficiencies in the area of soliton transmissions. Subsequently, this work is summarised and an outlook on further possibilities and research topics of NFT transmission is given in a conclusion.

Chapter 2

Fiber-Optic Transmission Systems

Just like any other transmission system, the fiber optic transmission system consists of a channel and components such as the transmitter, receiver, amplifiers and filters. The most indicative part of the fiber optic transmission system is the complex nature of pulse propagation of light through the fiber. In contrast to channels such as the radio- or electrical channel, the fiber optic channel is dispersive and nonlinear in nature. To mathematically describe the fiber optical channel, the nonlinear Schrödinger equation (NLSE) is used. This chapter is structured as follows: First, the characteristic effects of the pulse propagation through an optical fiber such as attenuation, dispersion and nonlinear effects are described and elaborated. Afterwards, these properties get summarized in the nonlinear Schrödinger equation and its solution being the solitons. To finalize this chapter, system components of the transmission channel shall be introduced and explained.

2.1 Transmission Channel

The main part of a long-haul fiber optic transmission system is the channel, which is described in this section. Since only single-mode fibers and only one polarization of light is used in later parts of this work, the focus in this section lays on the fiber losses, the group-velocity dispersion and nonlinear phase modulation. These effects get summarized by the NLSE, which can be solved by special pulse-shapes named solitons which keep their shape during transmission, by balancing the dispersion with nonlinear phase modulation.

2.1.1 Attenuation

During transmission, the propagating optical wave gets attenuated by effects such as Rayleigh scattering, material absorption and waveguide imperfections.

Microscopic local fluctuations in density lead to Rayleigh scattering, which is a fundamental loss mechanism [13]. These density fluctuations lead to changes of the refractive index, leading to the intrinsic loss of silica fibers α_R between 0.12 to 0.16 dB/km at $\lambda = 1550$ nm.
Material absorption is subdivided into intrinsic- (absorption by fused silica, the material used to make fibers) and extrinsic (losses due to impurities within silica) absorption losses. In modern *AllWave* fibers, this additional loss can be as low as 0.03 dB/km for wavelengths between 1300 to 1600 nm [13].
In addition to this, waveguide imperfections such as random core-radius variations and fiber bends lead to losses in the region of 0.03 dB/km [13].
In total, the attenuation of a standard single-mode fiber (SSMF) is in the region of $\alpha_{\mathrm{dB}} = 0.2$ dB/km for wavelengths in the region of $\lambda_c = 1550$ nm [2][13].

2.1.2 Dispersion

Dispersion in the context of fiber optic communications is the physical process, which leads to pulse broadening. This is mainly due to the chromatic dispersion, which describes dependence of the effective refractive index n_{eff} in an optical fiber on the frequency of the signal [13] and in turn leads to different phase velocities. Besides chromatic dispersion, there is also polarization mode dispersion due to different group velocities of the two polarization components and, in the case of multi-mode fibers, intermodal dispersion, which is based on the fact that different modes have different phase paths, has to be taken into account. In this chapter, chromatic dispersion will be discussed, since only single-mode fibers and the transmission on only one polarization was being studied.

Chromatic Dispersion

The chromatic dispersion D with the commonly used unit $[\frac{\mathrm{ps}}{\mathrm{nm \cdot km}}]$ is a combined effect of *material dispersion* and *waveguide dispersion*. Material dispersion (D_M) results from the refractive index of silica being dependent on the optical frequency ω, due to characteristic resonance frequencies at which the material absorbs electromagnetic radiation [13]. Waveguide dispersion (D_W) on the other hand is a result of the different refractive indices of the core and the cladding of a fiber. Due to the dependence of the mode field geometry on frequency, the percentage of energy of a wave which goes through the cladding or the core depends on the frequency. This leads to different effective refractive indices $n_{\mathrm{eff}}(\omega)$ for different frequencies. In SSMF, the waveguide dispersion leads to a dispersion shift of 30-40 nm. Since D_W is dependent on fiber parameters such as the core radius and refractive index differences, it is possible to design fibers with a zero dispersion close to 1550 nm. These kind of fibers are called dispersion shifted fiber (DSF). To compare the dispersion depending on the wavelength of SSMF and DSF, Fig. 2.1 shows dispersion curves for both fiber types. To describe the effect of dispersion on the

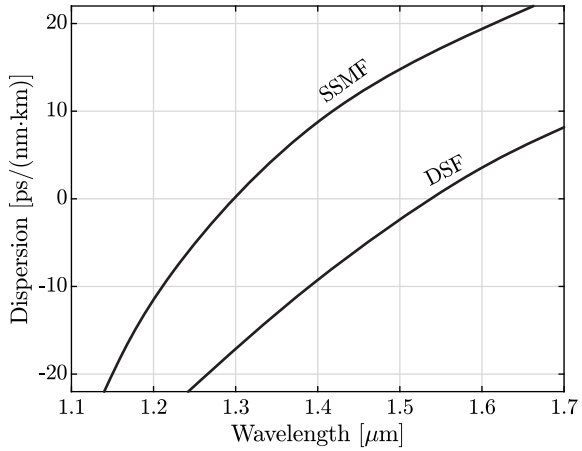

Figure 2.1: Approximated dispersion parameter D depending on the wavelength for standard single mode fiber and dispersion shifted fiber. [13]

phase velocity v_{ph}, the propagation constant $\beta(\omega)$ is used according to [13][14]

$$v_{ph}(\omega) = \frac{\omega}{\beta(\omega)} = \frac{c_0}{n_{\text{eff}}(\omega)}. \tag{2.1}$$

Mathematically, the dependence of the propagation constant $\beta(\omega)$ of the considered mode is described with the help of a Taylor series expansion around ω_0

$$\beta(\omega) = n_{\text{eff}}(\omega)\frac{\omega}{c_0} = \beta_0 + \beta_1(\omega - \omega_0) + \frac{1}{2}\beta_2(\omega - \omega_0)^2 + \frac{1}{6}\beta_3(\omega - \omega_0)^3 + ..., \tag{2.2}$$

with $\beta_m = (\mathrm{d}^m\beta/\mathrm{d}\omega^m)_{\omega=\omega_0}$. Here, β_1 leads to the group velocity $v_g = 1/\beta_1$ and β_2 to the resulting group velocity dispersion, which concludes in the dispersion parameter D according to [13][14]

$$D = \frac{\mathrm{d}\beta_1}{\mathrm{d}\lambda} = -\frac{2\pi c_0}{\lambda^2}\beta_2 \approx \frac{\lambda}{c_0}\frac{\mathrm{d}^2 n_{\text{eff}}}{\mathrm{d}\lambda^2}. \tag{2.3}$$

At normal dispersion ($D < 0$) waves with higher frequencies propagate slower, while at anomalous dispersion ($D > 0$) waves with higher frequencies propagate faster. Finally, the last relevant part of the Taylor series expansion β_3 is describing the dispersion slope.

2.1.3 Nonlinear Effects

If the system response, through which the light wave is sent, depends on the intensity of the light, one speaks of nonlinear transmission. One cause is the dependence of the refractive index of the medium on the intensity of the light wave, leading to a power dependent phase shift. This is called the Kerr effect

[13][14]. In addition, there are scattering processes resulting from an interaction of the light with the lattice structure of the medium. This results in Raman scattering and Brillouin scattering [13][14]. In the NLSE, only the Kerr effect and the resulting spectral broadening are considered. To describe these, the nonlinear coefficient γ is used. This coefficient is described as

$$\gamma = \frac{\omega n_2}{c_0 A_{\text{eff}}}, \tag{2.4}$$

and is commonly given in $[\frac{1}{\text{W}\cdot\text{km}}]$. Here, n_2 is the intensity dependent refractive index and A_{eff} the effective mode field size. The resulting nonlinear phase shift during transmission can then be described as follows

$$\Delta\Phi_{NL} = -\gamma P_0 L_{\text{eff}}, \tag{2.5}$$

where P_0 is the input power and L_{eff} the effective fiber length, which describes the length of an attenuation-free fiber with the same resulting nonlinear phase shift according to

$$L_{\text{eff}} = [1 - \exp(-\alpha L)]/\alpha. \tag{2.6}$$

Kerr effect (spectral broadening)

The most important outcomes of the Kerr effect are self-phase modulateion (SPM), cross-phase modulation (XPM) and four-wave mixing (FWM) [14].

Self-Phase Modulation

The effect SPM behaves similarly to the effect of dispersion, afterall it changes the phase of the light depending on some parameters. The effects of SPM and dispersion can reinforce each other, but at the same time they can also compensate each other as will be discussed in Section 2.1.5. The nonlinear phase rotation $\Delta\Phi_{NL}$ causes a frequency offset of the carrier light wave [14]:

$$\Delta f_{NL}(t) = \frac{1}{2\pi}\frac{\text{d}}{\text{d}t}\Delta\Phi_{NL}(t). \tag{2.7}$$

Due to a time-varying carrier envelope amplitude $A(t)$, the phase rotation is caused by the temporal change of the amplitude, which causes that also the frequency offset itself turns out to be time-dependent. This results in an intensity dependent phase modulation. This frequency change is called chirp [14]:

$$\Delta f_{NL}(t) = -\frac{1}{2\pi}\gamma L_{\text{eff}}\frac{\text{d}}{\text{d}t}|A(t,0)|^2. \tag{2.8}$$

From Eq. (2.8) follows that an increasing power results in a decrease of frequency, while decreasing power results in an increased frequency.

Cross-Phase Modulation and Four-Wave Mixing

In addition to self-phase modulation, there are other disturbances that occur in transmissions with multiple channels. XPM causes a mutual interference of several channels. Even if these channels have different wavelengths or propagation directions, they can influence each other in a power-dependent manner. Thus, the phases of several waves can be further changed.
Through FWM, new pulses are created with frequencies that were previously not used. Here, up to three light waves generate frequency components at frequencies which were not present before. This leads to a reduction in usable signal power and jitter.

2.1.4 Nonlinear Schrödinger Equation

To describe the pulse propagation through an optical fiber, the effects mentioned above can be summarized in the simplified, generalized NLSE including noise and loss according to [13]

$$\frac{\partial A(t,z)}{\partial z} = \frac{\mathrm{j}}{2}\beta_2 \frac{\partial^2 A(t,z)}{\partial t^2} - \mathrm{j}\gamma |A(t,z)|^2 A(t,z) - \frac{\alpha}{2}A + N(t,z), \tag{2.9}$$

which is valid for single polarization, single mode transmission using pulse length longer than 1 ps. Here $A(z,t)$ is the complex envelope of the signal, where z is the space coordinate along the fiber, measured in km, and t is the retarded time, measured in seconds. The terms from the left to the right hand side of the right side of the equation are the chromatic dispersion in [ps^2/km], the Kerr-effect induced nonlinear phase shift, the attenuation and noise.
For simplicity of the following discussions, it is preferable to write (2.9) without noise and loss in a normalized form by introducing

$$\tau = \frac{t}{T_0}, \qquad \xi = z/(\mathrm{sgn}(\beta_2)L), \qquad U = A/\sqrt{P_0}, \tag{2.10}$$

where $T_0 = \sqrt{|\beta_2|L/2}$, L is the link length and $P_0 = 2/(\gamma L)$. This changes equation 2.9 to

$$\mathrm{j}\frac{\partial U}{\partial \xi} = \frac{\partial^2 U}{\partial \tau^2} - 2s|U|^2 U. \tag{2.11}$$

Here, $s = \mathrm{sgn}(\beta_2)$ depends on normal ($s = 1$) or anomalous ($s = -1$) dispersion. Mind here, that the choice of parameter which the normalization is based on is arbitrary. For example it is also possible to

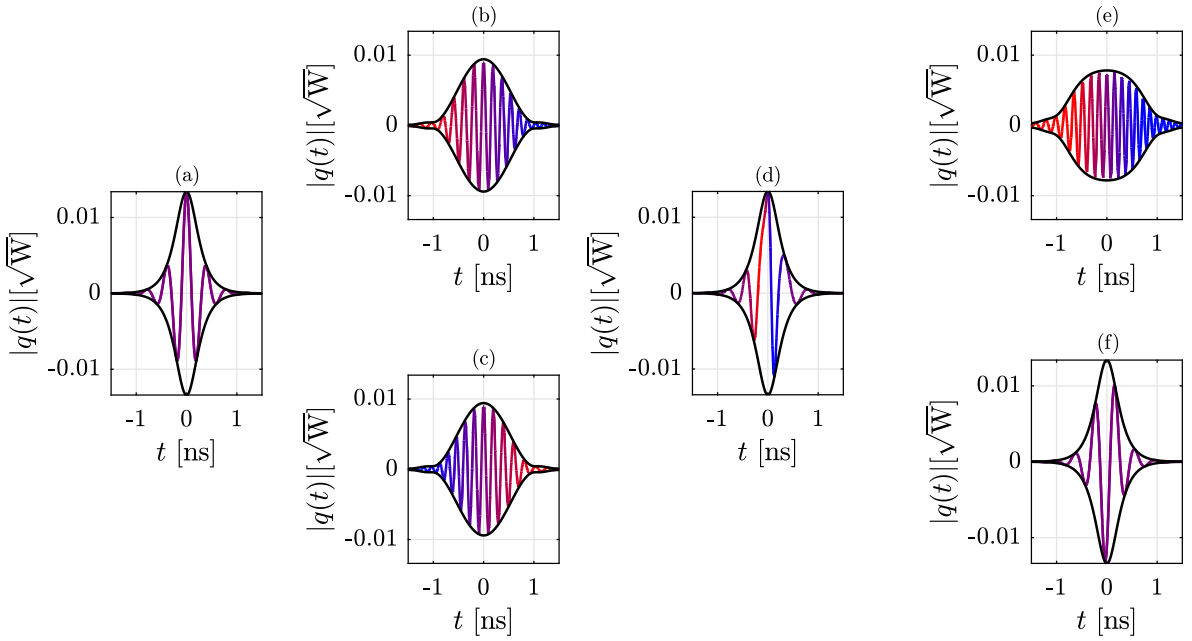

Figure 2.2: Interaction between dispersion and SPM for a sech-shaped pulse with $T_0 = 100\,\text{ps}$ and 1000 km transmission without attenuation ($|D| = 17\,{}^{\text{ps}}/_{\text{nm}\,\cdot\,\text{km}}, \gamma = 1.6\,\text{W}^{-1}\text{km}^{-1}$). Carrier frequency not at scale and color coded to show red/blue shift due to fiber effects. (a) Tx-pulse, (b) Impact of normal dispersion, (c) Impact of anomalous dispersion, (d) Frequency shift due to of SPM, (e) Combined impact of normal dispersion and SPM, (f) Combined impact of anomalous dispersion and SPM.

use T_0 as normalization parameter, which is often times used especially for soliton transmissions, as described in the next section.

2.1.5 Solitons

Solitons are wave packets, which keep their shape while propagating at a constant velocity through a dispersive, nonlinear medium. Optical, spacial solitons can mathematically be described by the sech-function [15].

To conceptually understand solitons, one has to look at the interactions of SPM and dispersion. SPM causes a power-dependent spectral pulse broadening, while the dispersion causes a temporal pulse broadening that is dependent on the frequency. Since the total pulse energy remains the same, the amplitude of the pulse is smaller, which weakens the effect of SPM. This shows how SPM and dispersion can influence each other. Due to SPM, the frequency changes depending on the instantaneous power according to (2.8). At the same time, the pulse width changes due to the dispersion in dependence on the frequency. Since the frequency turns out to depend on SPM, dispersion also depends on SPM.

A distinction must be made here between the influence of SPM on normal and anomalous dispersion.

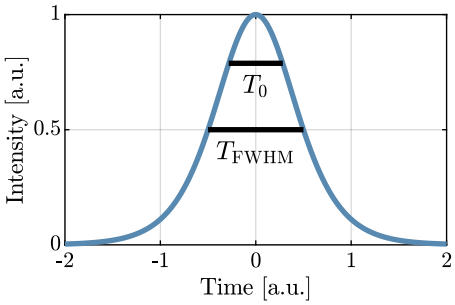

Figure 2.3: A fundamental soliton with $T_{\mathrm{FWHM}} = 1$ and its pulse width parameters.

This is depicted in Fig. 2.2. An exemplary pulse is shown in Fig. 2.2(a), which is broadened by normal or anomalous dispersion (Figs. 2.2(b) 2.2 (c), respectively). With normal dispersion, low-frequency signal components (shown here in red) of the signal propagate faster than the high-frequency signal components (shown here in blue). The red signal components are thus on the rising edge of the signal, which leads to the frequency being reduced even further by SPM (see Fig. 2.2(d)). Conversely, the blue signal components appear on the descending edge, which increases their frequency even further. These frequency shifts increase the effects of dispersion, resulting in further pulse broadening (Fig. 2.2(e)). Contrary to this, with anomalous dispersion, the high-frequency blue signal components move faster. These are then on the rising edge of the signal. This leads to their frequency being reduced. In addition, the low-frequency red signal components are slowed down. These are then on the descending edge. As a result, the frequency of these signal components is increased. Overall, this allows the effects of SPM and dispersion to compensate each other. Therefore, under optimal conditions (i.e. D, γ and soliton power), anomalous dispersion may result in no pulse broadening (Fig. 2.2(f)) [14].

Soliton Parameters

- **Pulse width**: The width of a soliton in time-domain is commonly given by the parameter T_0, which is related to the full width at half maximum (FWHM) power of a soliton as

$$T_{\mathrm{FWHM}} = 2T_0 \ln(1+\sqrt{2}) \backsimeq 1.763 T_0 \tag{2.12}$$

  and is depicted in Fig. 2.3. This leads to a 3-dB bandwidth of $B_{\mathrm{3dB}} = 0.1787/T_0 = 0.315/T_{\mathrm{FWHM}}$ and a 20-dB bandwidth of approximately $0.606/T_0$ [15].

- **Peak power**: To keep the equilibrium between dispersion and nonlinear phase-modulation, the pulse width and soliton peak power have to be linked according to [15][13]

$$N^2 = \gamma P_0 L_D = \gamma P_0 T_0^2 / |\beta_2|. \tag{2.13}$$

  Here, P_0 stands for the soliton peak power, N for the soliton order and L_D for the dispersion length.

- **Order and dispersion length**: The parameter N describes the order of a soliton with $U(\tau) = N\,\mathrm{sech}(\tau)$. If $N = 1$, the soliton is called fundamental soliton. Only fundamental solitons keep their sech-shape during transmission. If $N > 1$, the solitons' shape changes periodically with $L_D = T_0^2/|\beta_2|$ [15][13].

- **Lumped amplification**: Solitons are only defined for the NLSE without loss. By including loss with lumped amplification into the equation, the effective nonlinear index γ is dependent on the distance. Including attenuation and lumped amplification into the normalized NLSE changes (2.11) to [13]

$$\mathrm{j}\frac{\partial U}{\partial \xi} = \frac{\partial^2 U}{\partial \tau^2} - 2s|U|^2 U - \frac{\mathrm{j}}{2}\Gamma U + \frac{\mathrm{j}}{2} g(\xi) L_D U, \tag{2.14}$$

  where $\Gamma = \alpha L_D$ is the normalized fiber loss over one dispersion length and $g(\xi) = \sum_{m=1}^{N_A} g_m \delta(\xi - \xi_m)$, with N_A being the number of amplifiers, g_m the gain of the amplifier and ξ_m the amplifier location. It is then useful, to add the transformation [13]

$$U(\xi, \tau) = \sqrt{p(\xi)} v(\xi, \tau). \tag{2.15}$$

  Here $p(\xi)$, standing for the loss/gain is a rapidly varying function of ξ and $v(\xi, \tau)$, standing for the now changing soliton envelope is a slowly varying function of ξ. This changes (2.14) to [13]

$$\mathrm{j}\frac{\partial v}{\partial \xi} = \frac{\partial^2 v}{\partial \tau^2} - 2p(\xi) s |v|^2 v. \tag{2.16}$$

  If furthermore the normalized amplifier spacing $\xi_A = L_A/L_D \ll 1$, the soliton width stays the same, even with varying power levels due to attenuation. This is called a path-averaged or guiding-center soliton [15][13]. One can then replace $p(\xi)$ by its average value $\bar{p}$, introduce it into 2.16, and yield the standard NLSE. To create the path-averaged soliton, it is then needed to

increase the input peak power of the soliton: $P_S = P_0/\bar{p}$, leading to

$$f_{\mathrm{LM}} = \frac{P_S}{P_0} = \frac{1}{\bar{p}} = \frac{\Gamma\xi_A}{1-\exp(-\Gamma\xi_A)} = \frac{G\ln G}{G-1}, \tag{2.17}$$

where $G = \exp(\Gamma\xi_A)$ is the amplifier gain. For $\alpha = 0.2\,\mathrm{dB/km}$ and $L_A = 50\,\mathrm{km}$ this leads to $G = 10$ and $f_{\mathrm{LM}} \approx 2.56 = 4.08\,\mathrm{dB}$.

- **Soliton collisions**: Solitons from different channels collide during transmission due to different group velocities. After colliding, solitons keep their shape, albeit with changed phase, due to XPM occurring during collision [15]. This can have an effect especially in lumped amplification systems, due to uneven (power dependent) XPM. It is thus needed to take the collision length L_{coll} into account when designing a non dispersion managed system. The collision length can be calculated by [16][17]

$$L_{\mathrm{coll}} = \frac{2T_{\mathrm{FWHM}}T_0}{|\beta_2|\Omega_{\mathrm{ch}}} \tag{2.18}$$

with $\Omega_{\mathrm{ch}} = 2\pi f_{\mathrm{ch}}T_0$ being the normalized frequency spacing f_{ch} between two channels. L_{coll} is defined to be the distance over which two solitons overlap at their half power point. Since XPM leads to a time dependent phase shift, it in turn leads to a shift in frequency during collision, which, without attenuation, can be calculated by [16][17]:

$$\begin{aligned} \Delta\Omega(\Omega_{\mathrm{ch}},\xi) &= \frac{1}{\Omega_{\mathrm{ch}}}\int \mathrm{sech}^2(\tau - \frac{\Omega_{\mathrm{ch}}}{2}\xi)\,\mathrm{sech}^2(\tau + \frac{\Omega_{\mathrm{ch}}}{2}\xi)\,\mathrm{d}\tau \\ &= \frac{4}{\Omega_{\mathrm{ch}}}\frac{\Omega_{\mathrm{ch}}\xi\cosh(\Omega_{\mathrm{ch}}\xi) - \sinh(\Omega_{\mathrm{ch}}\xi)}{\sinh^3(\Omega_{\mathrm{ch}}\xi)}. \end{aligned} \tag{2.19}$$

The maximum frequency shift can be calculated to be $4/(3\Omega_{\mathrm{ch}})$, which leads to $\Delta f_{\max} = (3\pi^2 T_0^2 f_{\mathrm{ch}}^{-1})$ in physical units, but goes down to zero after the collision. For example, with $f_{\mathrm{ch}} = 10\,\mathrm{GHz}$ and $T_0 = 100\,\mathrm{ps}$ the maximum frequency shift is around $\Delta f = 338\,\mathrm{MHz}$. At first glance, this shift seems to be small, but compared to the 3-dB bandwidth of a 100 ps soliton, which is 1.7867 GHz, this should not be neglected, especially if the receiver is set at a point of collision.
Additional care needs to be taken, if a link using lumped amplification is used. If the condition $L_{\mathrm{coll}} \gg L_A$ is not met, a frequency shift can remain due to different power levels during the collision. These power levels have to even out over multiple amplifier spans, to keep the transmitted center frequency.

2.1.6 Common Fiber Types

Tab. 2.1 [18] exemplifies the parameters of an SSMF (OFS AllWave), an ordinary DSF, a non-zero dispersion shifted fiber (NZDSF) (OFS Truewave RS), which is a DSF with a shifted dispersion slope such that residual dispersion remains at wavelengths of 1550 nm and a dispersion compensating fiber (DCF) (Lycom DK, with normal dispersion) for the fiber types treated in this work. While the aforementioned NZDSF was used for all soliton transmissions [19][20] (see Chapter 6), the SSMF was used in [21],[22]. The DCF was not used here, but should be mentioned here as it finds relevance in a later chapter (Chapter 4).

Since in modern long-haul transmission systems strong DSP can be used to compensate for dispersion, SSMF is widely used as it has the lowest non-linearity of the common fiber types.

On the contrary, the low dispersion value of an NZDSF leads to longer dispersion lengths and, in the case of a soliton WDM transmission, longer collision distances. This is why NZDSF is often used for soliton transmissions.

DSF was widely deployed in the past (especially in Japan) when broadband dispersion compensation was not yet possible. However, later introduced WDM transmission over fibers without dispersion lead to very strong FWM effects, which are still a challenge today [3].

DCF is a way to compensate for dispersion without DSP and to achieve long transmission distances even with direct detection (which makes dispersion compensation difficult to impossible [23]).

Table 2.1: Exemplary parameters of different fiber types, with the AllWave being an SSMF, the TrueWave an NZDSF and the Lycom DK a DCF.

Fiber Type	Attenuation [dB/km]	D [ps/(nm)]	Nonlin. Ind. n_2 [(m_2/W)]	Eff. Core A_{eff} [μm^2]	Nonl. coeff. γ [1/(W·km)]
OFS AllWave	0.21	17.3	2.7e-20	86.6	1.46
OFS Truewave RS	0.21	4.4	2.7e-20	52.1	2.09
DSF	0.23	0	2.7e-20	55	1.99
Lycom DK	0.5	-102	2.2e-20	17	5.24

2.2 System Components

Further system components of the fiber optic transmission link are, for example, transmitters and receivers, which are used here for electro-optical conversion (or vice versa), but also optical amplifiers and filters.

This section will describe these devices. In addition, system parameters are mentioned which are also relevant in later experiments, as they correspond to the laboratory equipment used.

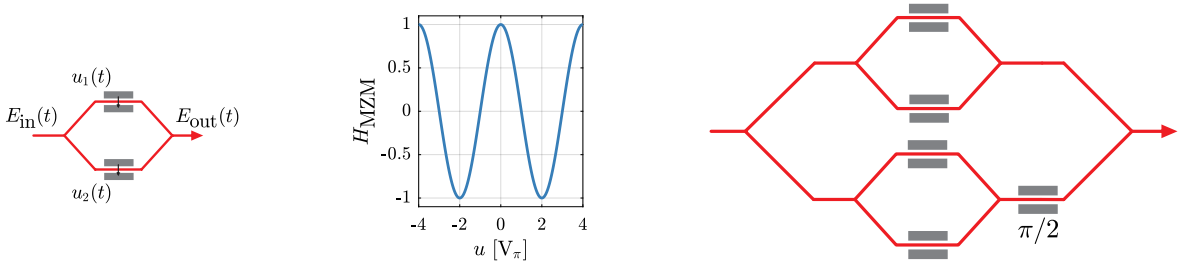

(a) MZM

(b) MZM transfer function.

(c) IQ-MZM consisting of two MZMs and an additional phase shifter for the quadrature part.

Figure 2.4: External Modulators

2.2.1 Transmitter Side

The transmitter (Tx) of a fiber optic transmission system is tasked with converting digital data signals into analog optical signals. In this work a digital-to-analog converter (DAC) is used to generate an analog electrical base-band signal. This is then externally modulated onto a continuous wave (CW) laser by using a combination of Mach Zehnder Modulators (MZMs).

Electrical Components

The electrical components on the transmitter side used in this work are an arbitrary waveform generator (AWG), which is used as DAC, and radio frequency (RF) amplifiers to increase the analog electrical peak-to-peak voltage (V_{PP}). The AWG used in this work was the Keysight M18196A [24], with a nominal resolution of 8 bits and an ENOB of around 5.5 bits. The sample rate can be set between $84 - 92\,\text{GS/s}$, and the V_{PP} can reach up to 1 V. Since the $1\,V_{\text{PP}}$ can be too low, especially if the signal paths are further split in later experiments, additional RF amplifiers have to be used to reach the required swing voltages for the modulators at the cost of additional noise. This adds to other impairments of the transmitter, such as quantization noise, bandwidth limitations of AWG, amplifiers and cables and timing offsets (skews) between different channels due to different cable lengths and signal paths.

Electro-Optical Conversion

There are two ways in which the optical carrier can be modulated: direct modulation and external modulation. The simplest type of direct modulation is so-called on-off keying. Here, a binary signal is represented by switching the laser on and off. With direct modulation, however, laser chirp occurs, which leads to unstable frequencies when the optical power is lowered or raised. With external modulation,

the laser does not change its output power. Here, the data is applied on the carrier by the optical modulator. Most common optical modulators are Mach-Zehnder modulators (MZMs) [2][13]. An MZM is formed by two optical phase modulators as depicted in Fig 2.4a.
In an MZM, the optical signal is split into two waveguides consisting of a Mach-Zehnder interferometer (MZI) each, which get combined subsequently. If an electrical field is applied to an MZI, the refractive index of the waveguide changes. This leads to a phase shift of the optical signal depending on the electrical field. The electrical field $u(t) = u_{\mathrm{DAC}}(t) + u_{\mathrm{bias}}$ applied to an MZI consists of the driving voltage (e.g. the (amplified) signal after the DAC) u_{DAC} and a constant bias voltage u_{bias}. The phase shift $\phi(t)$ is then linearly proportional to $u(t)$ according to

$$\phi(t) = \frac{\pi}{2 \cdot V_\pi} u(t). \tag{2.20}$$

Here, V_π is is the device-specific voltage, which leads to a phase shift of $\pi/2$.
The output of the MZM $E_{\mathrm{out}}(t)$ is then a recombination of differently phase modulated MZM input shares:

$$E_{\mathrm{out}}(t) = \frac{E_{\mathrm{in}}(t)}{2} \left[\exp\left(\mathrm{j} \frac{\pi}{2V_\pi} u_1(t) \right) + \exp\left(\mathrm{j} \frac{\pi}{2V_\pi} u_2(t) \right) \right]. \tag{2.21}$$

By using $u(t) = u_1(t) = -u_2(t)$ (the so-called *push-pull* mode) and the relation $\cos(x) = 0.5 \cdot (\exp(\mathrm{j}x) + \exp(-\mathrm{j}x))$ the transfer function of an MZM can be summarized to

$$H_{\mathrm{MZM}} = \frac{E_{\mathrm{out}}}{E_{\mathrm{in}}} = \cos\left(\frac{\pi}{2 \cdot V_\pi} u(t) \right), \tag{2.22}$$

which is depicted in Fig. 2.4b. By choosing a proper working point (for coherent detection: $u_{\mathrm{bias}} = -V_\pi$) and voltage swing of u_{DAC} (here: $V_{\mathrm{PP}} \ll 2V_\pi$) an approximately linear amplitude modulation is possible. The optimal V_{PP} to drive the MZM is use specific, since high V_{PP} leads to nonlinearly driven MZMs, but maximum output powers. If the transmitted signal is prone to nonlinear distortions, smaller V_{PP} with as linear as possible driven modulators is preferable at the cost of lower powers.
If a complex modulation is to be used, a second MZM can be used for the quadrature part of the signal. This is then followed by a fixed MZI, which shifts the quadrature part by $\pi/2$, as depicted in Fig. 2.4c.

2.2.2 Receiver Side

The receiver (Rx) of an optical transmission system consists of the optical-electrical (O/E) conversion and the electrical analog-to-digital converter (ADC). The simplest technique for O/E-conversion is a photo-diode (PD), which generates a photo-current proportional to the intensity of the input signal. This is called direct detection (DD). If standard DD is employed, the phase information is lost and the

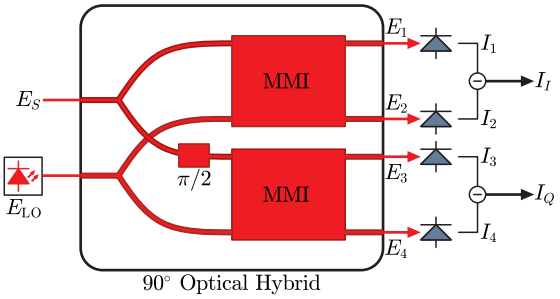

Figure 2.5: Coherent receiver for a single polarization.

carrier envelope has to be positive. To regain the phase, complex DSP schemes have to be used and additional requirements apply to the signal [23][25][26]. This is in contrast to coherent detection, which uses an optical local-oscillator (LO) as phase reference. This not only enables phase modulation, but also polarization multiplexing, hence quadrupling the spectral efficiency compared to DD. However, this comes at the cost of not only an additional LO, but also multiple PDs. Hybrid detection schemes such as Stokes-vector receivers, which can enable complex modulation formats without LOs or polarization-diverse DD can increase the spectral efficiency with less technical overhead, but are niche products or still under investigation.

Coherent Receiver

A possible way to build a phase-diversity coherent receiver is depicted in Fig. 2.5. An optical coherent receiver creates a lower frequency representation of the signal information by beating the optical signal with a continuous-wave local oscillator [27]. The main component of the coherent receiver is a 90° optical hybrid, which consists of two 2x2 multi-mode interference couplers (MMIs). In the MMIs, the direct-pass and cross-coupling outputs have a 90° phase shift between them. By introducing two photodiodes after each MMI a balanced detection is possible, which suppresses the DC component and maximizes the signal photocurrent. If an additional 90° phase shift is implemented in one arm, the quadrature components of the signal can be received. The optical fields after the MMIs can be described by a combination of the optical fields of the signal E_S and the LO E_{LO} by

$$E_1 = 0.5 \cdot (E_S + E_{\mathrm{LO}}) \qquad E_3 = 0.5 \cdot (E_S + \mathrm{j}E_{\mathrm{LO}})$$
$$E_2 = 0.5 \cdot (E_S - E_{\mathrm{LO}}) \qquad E_4 = 0.5 \cdot (E_S - \mathrm{j}E_{\mathrm{LO}})$$

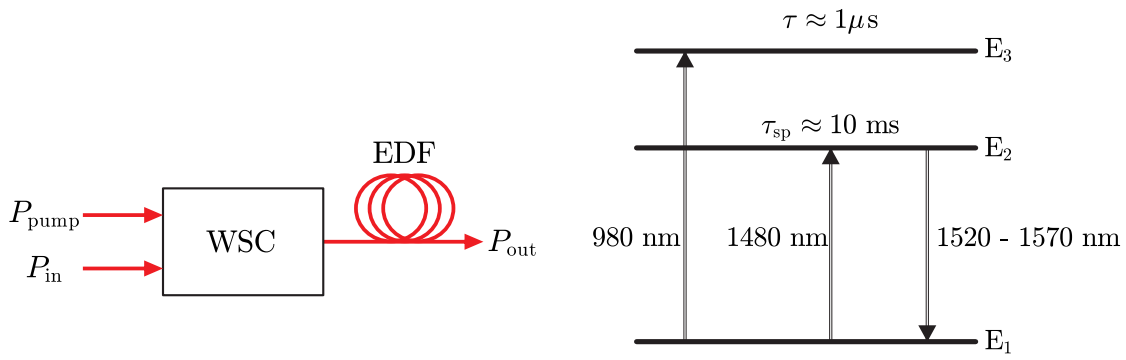

(a) Forward pumped EDFA setup.

(b) Er^{3+} ion energy levels.

Figure 2.6: EDFA Principle

leading to the photo currents

$$I_I(t) = I_1(t) - I_2(t) = R\sqrt{P_S P_{\text{LO}} \cos(\phi_s(t) - \theta_{\text{LO}})}$$
$$I_Q(t) = I_3(t) - I_4(t) = R\sqrt{P_S P_{\text{LO}} \sin(\phi_s(t) - \theta_{\text{LO}})}$$

where R is the responsivity of the photodiodes, and P_S and P_{LO} are the powers of the optical fields. If two 90° optical hybrids are used and the optical signal and local oscillator are split by a polarization beam splitter, both polarizations can be received to use all possible degrees of freedom of coherent detection.

2.2.3 Amplifiers

The introduction of purely optical, broad band amplifiers was one of the breakthrough events which lead to optical transmission replacing electrical ones. In this work two kinds of amplifiers will be adressed: erbium-doped fiber amplifiers (EDFAs) and distributed Raman amplifiers [13]. While EDFAs are based on a relatively short sections of erbium-doped fibers (EDFs), where the combination of a pump laser with the optical signal leads to an amplification of the signal [28][29][13]. Distributed Raman amplifiers are based on stimulated Raman scattering inside of the transmission fiber.

EDFA

The system setup of a forward pumping EDFA is depicted in Fig. 2.6a [2]. The optical signal and a pump laser are coupled by using a wavelength selective coupler (WSC). The amplification of the signal takes place in an EDF. The EDF is doped by Er^{3+} ions, which can take different energy levels as depicted in Fig. 2.6b. A carrier on the stable energy level E_1 is moved to E_3 due to the energy of a pump laser with a wavelength of 980 nm, leading to an inversion. The carrier lifetime at this level

is only around 1 μs, whereupon it moves to energy level E_2 by emission of heat, where it reaches a meta-stable state with a lifespan of multiple ms. Due to constant pumping, the carrier density at E_2 is higher than at E_1. If then a signal photon hits an Er-ion at laser level E_2, it transitions to ground level E_1 by emission of an additional photon with the same frequency, phase, polarization and direction of the impacting signal photon. This way transparent gains of up to 33 dB with saturation at 20-33 dBm can be reached. Since the pump energy levels are not discrete, but split in many sub-levels, a broad gain bandwidth can be achieved with wavelength dependent gain. One drawback of the EDFA are spontaneous emissions from E_2 to E_1, which also get reamplified inside the EDF and following amplifiers of the transmission link. This so called amplified spontaneous emission (ASE) is the main source of optical noise and can be considered white inside the channel bandwidth [2]. The noise added by the amplifier can be chacterized by the noise figure F_N, which describes the ratio of the SNR of the optical signal at the input and output of the EDFA as

$$F_\mathrm{N} = \frac{\mathrm{SNR}_\mathrm{in}}{\mathrm{SNR}_\mathrm{out}}. \tag{2.23}$$

The theoretical minimum of F_N is 3 dB, while most commercial EDFAs have a noise figure in the range of 5 dB. If the optical noise by the amplifiers is the dominant noise source, the performance of a system can be measured by the optical signal-to-noise ratio (OSNR). The OSNR can be measured by an optical spectrum analyzer (OSA) over both polarizations by measuring and integrating the signal- and noise power inside the signal bandwidth B_opt. Due to historical reasons, the OSNR gets further normalized to a reference bandwidth B_ref of 0.1 nm. The OSNR after an EDFA can be calculated by

$$\mathrm{OSNR} = \frac{P_\mathrm{in}}{F_\mathrm{N} \cdot h \cdot f_c} \cdot \frac{1}{B_\mathrm{ref}}. \tag{2.24}$$

with the Planck-constant h and the carrier frequency f_c [2]. Inserting the values for $h = 6.62607 \cdot 10^{-34}$ J·s, $f_c = 1550$ nm and B_ref the computation of the OSNR in dB can be broken down to [2]

$$\mathrm{OSNR}\ [\mathrm{dB}] \approx 58\,\mathrm{dBm} - F_\mathrm{N}\,[\mathrm{dB}] + P_\mathrm{in}\,[\mathrm{dBm}]. \tag{2.25}$$

For a multi-span system, where $P_\mathrm{in} = P_\mathrm{Launch} - \alpha_\mathrm{dB} L_A$, the total resulting OSNR at Rx can be computed by

$$\mathrm{OSNR}\ [\mathrm{dB}] \approx 58\,\mathrm{dBm} - F_\mathrm{N}\,[\mathrm{dB}] + P_\mathrm{Launch}\,[\mathrm{dBm}] - \alpha_\mathrm{dB} L_A - 10 \cdot \log_{10}(N_\mathrm{sp}). \tag{2.26}$$

Distributed Raman Amplifier

Raman amplifiers are based on stimulated Raman scattering (SRS) occurring in silica fibers. Similar to EDFAs, a pump and a signal beam at different wavelengths are injected into a fiber. During SRS a

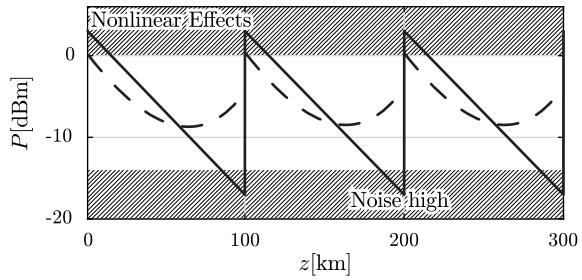

(a) Exemplary EDFA gain profile (solid line) and Raman gain profile (dashed line). Transmission without Raman amplifiers is prone to nonlinear distortions and leads to lower input powers into the EDFAs, decreasing the OSNR.

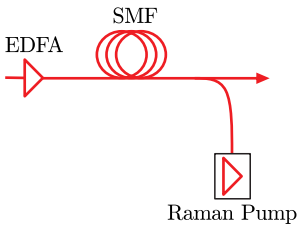

(b) System setup with forward pumping EDFA and backwards propagating Raman amplification.

Figure 2.7: Raman Principle

pump photon loses energy to create another photon of reduced energy at the signal frequency, while the remaining energy is absorbed by the material. The energy is then transferred continously, while the beams (counter-)propagate. The gain of a Raman amplifier can be described by [13]

$$g(\omega, z) = g_R(\omega) \cdot \frac{P_p(z)}{a_p}, \tag{2.27}$$

with a_p being the cross-sectional area of the pump beam, $P_p(z)$ is the pump power during propagation and g_R the Raman-gain coefficient. The Raman-gain coefficient is dependent on the frequency difference between the pump and the signal and has its peak at a frequency difference of around 13.2 THz [30], with a FWHM bandwidth of 6 THz. Since the overall gain is strongly dependent on the fiber core cross-section, the ratio g_R/a_P can be very different for different fiber types.

2.2.4 Filters

Filters in optical communications are mainly used for out-of band filtering of noise and for selecting and filtering out channels in optical add drop multiplexers. Additionally, more sophisticated filters can be used as gain-flattening filters of frequency dependent gains of EDFAs and Raman amplifiers.
In this work, three different filters were used in experiments namely the Finisar WaveShaper 4000S (WS), the Yenista X-Tract XTA-50 and the DiCon manually tunable bandpass filter (MTBF) in descending order of complexity. Different transfer characteristics of the filters are depicted in Fig. 2.8. The WaveShaper is a fully progammable filter, where the filter shape can be set in steps of 1 GHz. This enables, for example, gain-flattening and also dispersion compensation. The WS is based on a Liquid Crystal on Silicon (LCoS) technology [31], where the input signal is dispersed by a conventional grating before it hits the LCoS processor, which consists of a matrix of reflective elements. These elements

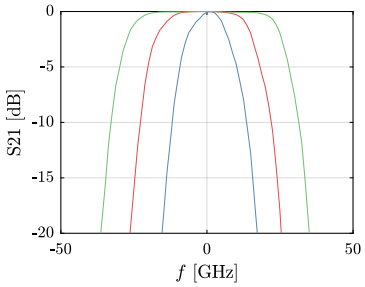

(a) Transfer characteristic for Finisar WS with (blue) 20, (red) 40 and (green) 60 GHz bandwidth and rectangular filter shape.

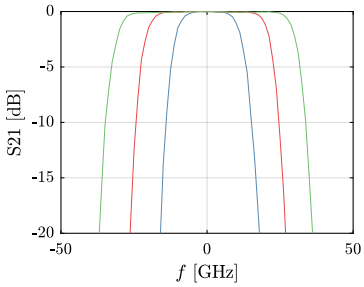

(b) Transfer characteristic for Yenista XTA with (blue) 20, (red) 40 and (green) 60 GHz bandwidth.

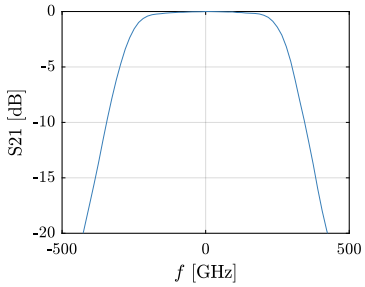

(c) Transfer characteristic for DiCon MTBF with 3.2 nm bandwidth.

Figure 2.8: Normalized transfer characteristics of experimentally measured optical filters.

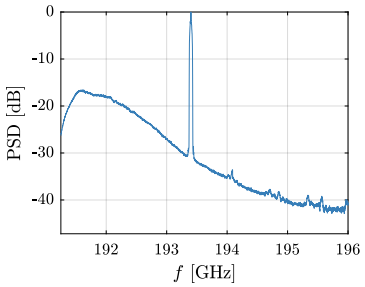

(a) PSD after four 50.5 km spans NZDSF with lumped amplification using EDFAs and transmitting a 40 GBd signal.

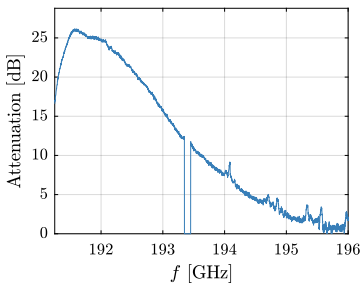

(b) Transfer characteristic for the WS to flatten the PSD.

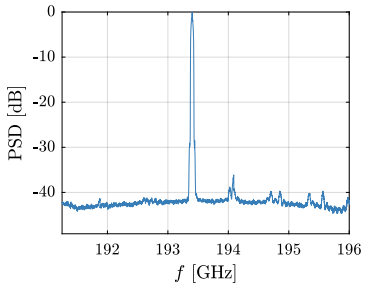

(c) Flattened PSD with gain-flattening WS employed.

Figure 2.9: Gain flattening of four EDFAs using the waveshaper.

can change the phase of the reflected signals depending on an applied voltage and hence enable beam steering [32].

The XTA-50 is a bandpass filter with configurable middle frequency and bandwidth from 6.25 GHz up to 158.54 GHz [33]. This is enabled by a diffraction grating. The XTA-50 was mainly used for channel selection and out-of-band noise filtering at the receiver.

To filter out-of-band noise inside the loop, the DiCon MTBF was used. The MTBF is a filter with a fixed bandwidth of 3.2 nm (around 400 GHz at 1550 nm) and tunable center frequencies, which uses a hard-coated thin film interference filter mounted between two angled fiber colimators. By adjusting the filter angle, the center wavelength can be selected.

To exemplary show the possibility of gain flattening using the WS, a 40 GBd signal was transmitted at 1550 nm. The received broad-band spectrum after four 50.5 km spans NZDSF with lumped amplification

using EDFAs is depicted in Fig. 2.9a. To flatten the EDFA gain (here: out-of-band noise), the transfer characteristic of the WS is depicted in Fig. 2.9b, which results in a flattened power spectral density (PSD), as depicted in Fig. 2.9c.

Chapter 3

The Nonlinear Fourier Transform

The nonlinear Fourier transform (NFT) is, just like the common linear Fourier transform, a mathematical tool to decompose functions that depend on time into functions depending on frequency (or wavelength). In the linear Fourier transform, complex exponential functions $e^{\mathrm{j}\omega t}$ are regarded as eigenfunctions. This means that after the transformation, a signal consists of a superposition of complex exponential functions, which in turn represent harmonic oscillations. It follows from this that the linear Fourier transformation divides a signal into harmonic wave solutions and plots them according to their frequency. In this frequency spectrum, the amplitudes and phases of the individual frequency components are plotted. On the other hand, the NFT is a composition of linear and non-linear wave solutions and therefore has two spectra. In the NFT, as it will be used here later, non-linear wave solutions called solitons are the eigenfunctions of the signal. The NFT serves as a tool to solve integrable-nonlinear-dispersive-partial differential equations such as the nonlinear Schrödinger equation [34]. It rewrites the nonlinearities with linear operators [10]. This means that the nonlinear effects along the optical channel on the spectrum of the nonlinear Fourier transform become independent linear effects. In comparison to the linear Fourier transform, which divides a linear convolution channel ($y(t) = x(t) * h(t)$) into many parallel channels ($Y(f) = X(f) \cdot H(f)$), the NFT divides a non-linear dispersive channel into a certain number of parallel scalar channels [10]. This makes it possible (analogous to OFDM), to encode information on the nonlinear spectra. In contrast to the linear Fourier transform, the NFT forms two spectra. The discrete spectrum, which forms solitons in the time domain, and the continuous spectrum, which represents harmonic and dispersive wave solutions in the time domain.

First linear solutions of nonlinear differential equations have been observed unknowingly by John Scott Russell in 1834 when he observed stable waves in water channels. He named the discovered stable wave, which we know as soliton today, as *the great wave of translation*. Only 61 years later in 1895 this phenomenon was mathematically proven by Drs. Korteweg and de Vries [35], when they famously

proved the existence of a solitonic solution for the nonlinear, dispersive partial differential Korteweg-de Vries (KdV) equation

$$\frac{\partial q}{\partial z} = q\frac{\partial q}{\partial t} + \frac{\partial^3 q}{\partial t^3}, \tag{3.1}$$

which describes a mathematical model of waves on shallow waters.

The term solitons was coined in 1965 by Zabusky and Kruskal [36], who also showed numerically that solitons only undergo a phase change, but stay otherwise unaffected by collisions. The first inverse scattering transform (IST) was introduced in 1967, when Gardner et al. solved the KdV equation with the external potential of a scattering problem and analytically predicted soliton solutions for the KdV equation [37].

In 1968 mathematician Peter Lax generalized IST solution of the KdV equation to other partial differential equations (PDEs) and showed the mathematical relationship between a nonlinear equation and auxiliary operators with invariant eigenvalues (Lax pairs)[38].

Finally, in 1972 Zakharov and Shabat found a Lax pair for the NLSE, which enabled the IST for the fiber-optical channel [39]. The term nonlinear Fourier transform was then coined by Ablowitz et al in 1973 while further developing the IST for the NLSE [34, 40, 41]. Parallely, in 1973 Hasegawa and Tappert solved the nonlinear Schrödinger equation and found solutions for solitons [42].

3.1 Mathematical Derivation of the NFT

As described above, the NFT is a mathematical tool to solve nonlinear partial differential equations. Such an equation for an unknown function $q(t, z)$ can be simplified by the form [10]

$$\frac{\partial q}{\partial z} = K(q), \tag{3.2}$$

where K is an operator which depends on q. If a Lax pair can be found with two operators L and M, which depend on $q(t, z)$, (3.2) can also be described by

$$\frac{\mathrm{d}L}{\mathrm{d}z} = ML - LM = [M, L], \tag{3.3}$$

where $[M, L]$ is called the commutator bracket [10, 38]. If we now assume the eigenvalues of $L(z)$ to be invariant with z and $L(z)$ to be diagonalizable, $L(z)$ is similar to Λ via $L(z) = G(z)\Lambda G^{-1}(z)$ [10]. Mind

here, that Λ is not depending on z. Using the product rule follows:

$$\begin{aligned}\frac{\mathrm{d}L(z)}{\mathrm{d}z} &= \frac{\mathrm{d}G(z)}{\mathrm{d}z}\Lambda G^{-1} + G\Lambda\left(-G^{-1}\frac{\mathrm{d}G(z)}{\mathrm{d}z}G^{-1}\right)\\ &= \frac{\mathrm{d}L(z)}{G}^{-1}\left(G\Lambda G^{-1}\right) - \left(G\Lambda G^{-1}\right)\frac{\mathrm{d}G(z)}{\mathrm{d}z}G^{-1}\\ &= M(z)L(z) - L(z)M(z),\end{aligned} \tag{3.4}$$

where

$$M = \frac{\mathrm{d}G(z)}{\mathrm{d}z}G^{-1}. \tag{3.5}$$

Now, the eigenvalues λ of the operator L can be defined together with the eigenvector v as

$$Lv = \lambda v, \tag{3.6}$$

which can be derived to z using (3.4) resulting in

$$\begin{aligned}\frac{\partial Lv}{\partial z} &= \frac{\partial L}{\partial z}v + L\frac{\partial v}{\partial z} = (ML - LM)\,v + L\frac{\partial v}{\partial z}\\ &= MLv - LMv + L\frac{\partial v}{\partial z} = \lambda\frac{\partial v}{\partial z}\\ \Leftrightarrow\quad &(L-\lambda I)\,\frac{\partial v}{\partial z} = LMv - MLv\\ &= LMv - M\lambda v = (L-\lambda I)\,Mv\\ \Leftrightarrow\quad &(L-\lambda I)(\frac{\partial v}{\partial z} - Mv) = 0.\end{aligned} \tag{3.7}$$

Assuming L to not be a diagonal matrix with its eigenvalues on the main diagonal and also keeping (3.5) in mind, follows

$$\frac{\partial v}{\partial z} = Mv. \tag{3.8}$$

The partial derivation of v to t can now be described by some operator P as

$$\frac{\partial v}{\partial t} = Pv. \tag{3.9}$$

Combining Eq. (3.6) (after rearranging to $\left(\frac{\partial}{\partial t}I - P\right)v = 0$) with Eq. (3.9) (after rearranging to $(L-\lambda I)\,v = 0$) leads to

$$P = \Sigma(L - \lambda I) + \frac{\partial}{\partial t}I \tag{3.10}$$

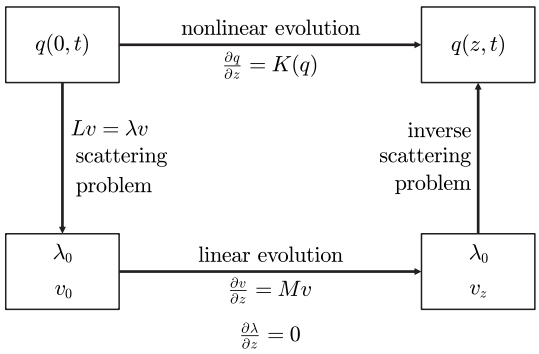

Figure 3.1: Lax approach for nonlinear evolution equations.

with some invertible operator Σ.
Using the Schwarz integrability condition $\left(\frac{\partial^2 v}{\partial t \partial z} = \frac{\partial^2 v}{\partial z \partial t}\right)$ Eqs. (3.8) and (3.9) can be combined into

$$\frac{\partial P}{\partial z} - \frac{\partial M}{\partial t} + [P, M] = 0, \tag{3.11}$$

which is called the zero-curvature condition. This shows that some nonlinear equations have hidden linearities, if fitting operators L, M, P can be found. This is exemplarily depicted in Fig. 3.1.
Those operators for the normalized NLSE have been found by Zakharov and Shabat [39] and Ablowitz et al [41]:

$$P = \begin{pmatrix} -\mathrm{j}\lambda & q(t,z) \\ -q^*(t,z) & \mathrm{j}\lambda \end{pmatrix}, \tag{3.12}$$

(together with Eq. (3.10))

$$L = \mathrm{j} \begin{pmatrix} \frac{\partial}{\partial t} & -q(t,z) \\ -q^*(t,z) & -\frac{\partial}{\partial t} \end{pmatrix}, \tag{3.13}$$

and

$$M = \begin{pmatrix} 2\mathrm{j}\lambda^2 - \mathrm{j}|q(t,z)|^2 & -2\lambda q(t,z) - \mathrm{j}q_t(t,z) \\ 2\lambda q^*(t,z) - \mathrm{j}q_t^*(t,z) & -2\mathrm{j}\lambda^2 + \mathrm{j}|q(t,z)|^2 \end{pmatrix}. \tag{3.14}$$

The nonlinear Fourier transform is then defined solely by the temporal P-equation (3.9). The M-equation is only used for the propagation of the spectrum and is not used for the transformation itself. Hence, we will proceed with the Zakharov-Shabat problem (ZSP)

$$\frac{\partial v}{\partial t} = \begin{pmatrix} -\mathrm{j}\lambda & q(t,z) \\ -q^*(t,z) & \mathrm{j}\lambda \end{pmatrix} v \tag{3.15}$$

as defined by Eqs. (3.9) and (3.12).

One can see that there are infinitely many solutions of v to (3.15) for a given $\lambda \in \mathbb{C}$, depending on the boundary conditions. These solutions form a subspace E_λ of continuously differentiable 2×1 vector functions of the vector space $\mathcal{H}$ [10]. The vector space $\mathcal{H}$ shall be equipped with a symplectic bilinear form $\mathcal{H} \times \mathcal{H} \mapsto \mathbb{C}$, which for a fixed $t \in \mathbb{R}$ is defined as

$$\langle u(t), w(t) \rangle_s = u_1(t)w_2(t) - u_2(t)w_1(t). \tag{3.16}$$

Additionally, the adjoint of any vector in $\mathcal{H}$ is defined as [10]

$$\tilde{u}(t) = \begin{pmatrix} u_2^*(t) \\ -u_1^*(t) \end{pmatrix} \tag{3.17}$$

and any two linearly independent solutions u and w form a basis for the solution space [10]. Finding two such solutions is possible at large $|t|$, if $q(t) \to 0$ as $|t| \to \infty$. This reduces (3.15) to

$$\frac{\partial v}{\partial t} = \begin{pmatrix} -\mathrm{j}\lambda & 0 \\ 0 & \mathrm{j}\lambda \end{pmatrix} v, \qquad \text{for large } |t| \tag{3.18}$$

and, keeping in mind $\frac{\partial}{\partial x} e^{kx} = k e^{kx}$, has the solutions

$$v^1(t, \lambda) \to \begin{pmatrix} 0 \\ 1 \end{pmatrix} e^{\mathrm{j}\lambda t}, \qquad t \to +\infty \tag{3.19}$$

$$v^2(t, \lambda) \to \begin{pmatrix} 1 \\ 0 \end{pmatrix} e^{-\mathrm{j}\lambda t}, \qquad t \to -\infty. \tag{3.20}$$

Using these boundary conditions and (3.15), one can calculate solutions for all $t \in \mathbb{R}$. In addition, one can use λ^* to calculate

$$v^1(t, \lambda^*) \to \begin{pmatrix} 0 \\ 1 \end{pmatrix} e^{\mathrm{j}\lambda^* t}, \qquad t \to +\infty \tag{3.21}$$

$$v^2(t, \lambda^*) \to \begin{pmatrix} 1 \\ 0 \end{pmatrix} e^{-\mathrm{j}\lambda^* t}, \qquad t \to -\infty. \tag{3.22}$$

Using (3.17) it is now possible to get $\tilde{v}^1(t, \lambda^*)$ and $\tilde{v}^2(t, \lambda^*)$, which are both elements of E_λ ($\tilde{v} \in E_{\lambda^*}$) [10]. These known elements of E_λ ($v^1(t, \lambda)$, $v^2(t, \lambda)$, $\tilde{v}^1(t, \lambda^*)$ and $\tilde{v}^2(t, \lambda^*)$) are called *canonical eigenvectors* or *Jost solutions*.

By choosing for example $\tilde{v}^1(t,\lambda^*)$ and $v^1(t,\lambda)$ at $t \to \infty$ as a basis of E_λ, one can calculate $v^2(t,\lambda)$ and $v^2(t,\lambda^*)$ and write

$$v^2(t,\lambda) = a(\lambda)\tilde{v}^1(t,\lambda^*) + b(\lambda)v^1(t,\lambda) \tag{3.23}$$

and

$$\tilde{v}^2(t,\lambda^*) = b^*(\lambda^*)\tilde{v}^1(t,\lambda^*) - a^*(\lambda^*)v^1(t,\lambda). \tag{3.24}$$

The time-independent [10] complex scalars $a(\lambda)$ and $b(\lambda)$ are called the nonlinear Fourier coefficients (NFCs) [10] and can be summarised by

$$\left[v^2(+\infty,\lambda), \tilde{v}^2(+\infty,\lambda)\right] = \left[\tilde{v}^1(+\infty,\lambda), v^1(+\infty,\lambda)\right] S, \tag{3.25}$$

where

$$S = \begin{pmatrix} a(\lambda) & b^*(\lambda^*) \\ b(\lambda) & -a^*(\lambda^*) \end{pmatrix} \tag{3.26}$$

is the so-called scattering matrix. The scattering-matrix contains all Fourier coefficients, which can in summary be computed using (3.20) and (3.15):

$$a(\lambda) = \lim_{t\to\infty} v_1^2 e^{\mathrm{j}\lambda t} \qquad b(\lambda) = \lim_{t\to\infty} v_2^2 e^{-\mathrm{j}\lambda t}. \tag{3.27}$$

Therefore, it is also a function of $q(t)$ (without spatial dependence). The scattering matrix describes how the solution of (3.15) is scattered from $t = -\infty$ to $t = \infty$. Figuratively, it symbolises how $v^2(-\infty,\lambda) = (1,0)^{\mathrm{T}} e^{-\mathrm{j}\lambda t}$ looks like at $t = \infty$ after it collides with the used signal $q(t,z)$. $v^2(-\infty,\lambda)$ is initially a complex oscillation. At a certain point in time it collides with $q(t,z)$. This collision causes the original wave to be scattered. The changed field is observed at $t = \infty$. On the basis of the change, conclusions can be drawn about the disturbance in the form of $q(t,z)$. With the parameters $a(\lambda)$ and $b(\lambda)$ that have now been obtained, the signal can be completely described.

The boundary conditions (3.19)-(3.22) and following the projection equations (3.23) and (3.24) are well-defined, if $\lambda \in \mathbb{R}$, which can be compared to wavelengths of the conventional Fourier transform. If $\lambda \in \mathbb{C}^+$, Eqs. (3.19) and (3.21) at $t = \infty$ decay and blow up, respectively, leading to the invalid solutions $v_2^1(t,\lambda) = 0$ and $v_2^1(t,\lambda^*) = \infty$. However, if $a(\lambda)$=0 for an $\lambda \in \mathbb{C}$, additional complex eigenvalues are part of the NFT spectrum. These complex eigenvalues are discrete points in $\mathbb{C}^+$, which are symmetric, i.e. if λ is an eigenvalue, then so is λ^* [10].

What follows, is that the Zakharov-Shabat operator for the NLSE has two types of spectra, which are the discrete spectrum on the positive complex plane $\mathbb{C}$ and the continuous spectrum, which includes the whole real line $\mathrm{Im}(\lambda) = 0$.

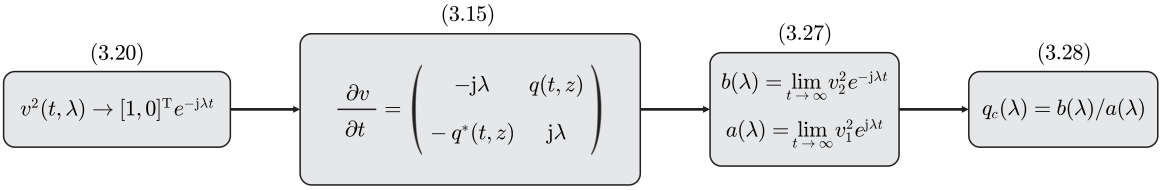

Figure 3.2: Summarized depiction of the transformation of a time-domain signal $q(t,z)$ into the continuous part of the NFT spectrum $q_c(\lambda)$, where the choice of λ is arbitrary, as long as $\lambda \in \mathbb{R}$.

Besides the eigenvalues, the ratios of the NFT coefficients are used to define the spectra:

$$q_c(\lambda) = \frac{b(\lambda)}{a(\lambda)}, \tag{3.28}$$

$$q_d(\lambda_k) = \frac{b(\lambda_k)}{\mathrm{d}a(\lambda)/\mathrm{d}\lambda|_{\lambda=\lambda_k}}, \qquad k = 1, 2, ...N. \tag{3.29}$$

Here, $q_c(\lambda)$ stands for the continuous spectrum, which represents the dispersive component of the signal, and $q_d(\lambda_k)$ stands for the discrete spectrum consisting of N solitons. To summarize, Fig. 3.2 shows the steps to transform a time-domain signal $q(t,z)$ into the nonlinear Fourier domain.
The composition of the energy of the signal is given by Parseval's identity [10]

$$\int_{-\infty}^{\infty} ||q(t)||^2 \mathrm{d}t = E_c + E_d, \tag{3.30}$$

with

$$E_c = \frac{1}{\pi} \int_{-\infty}^{\infty} \log\left(1 + |q_c(\lambda)|^2\right) \mathrm{d}\lambda \tag{3.31}$$

and

$$E_d = 4 \sum_{j=1}^{N} \mathrm{Im}(\lambda_k). \tag{3.32}$$

3.1.1 Spatial Evolution of the NFT Spectrum

So far, the NFT was introduced with only taking the retarding time into account. In this section the linear transfer function of the nonlinear Fourier spectrum shall be derived. As discussed earlier, the eigenvalues keep their properties and the eigenvectors propagate according to (3.8). Keeping in mind the boundary condition $q(t,z) \to 0$ for $|t| \to \infty$ and $z \leq L$ one can reduce (3.14) to

$$\frac{\partial v(t,z)}{\partial z} \to \begin{pmatrix} 2\mathrm{j}\lambda^2 & 0 \\ 0 & -2\mathrm{j}\lambda^2 \end{pmatrix} v(t,z). \tag{3.33}$$

Thus, the boundary conditions (3.19) and (3.20) at z need to be extended by a solution of (3.33):

$$v^1(t,\lambda;z) \to \begin{pmatrix} 0 \\ 1 \end{pmatrix} e^{\mathrm{j}\lambda t} e^{-2\mathrm{j}\lambda^2 z}, \qquad t \to +\infty \tag{3.34}$$

$$v^2(t,\lambda;z) \to \begin{pmatrix} 1 \\ 0 \end{pmatrix} e^{-\mathrm{j}\lambda t} e^{2\mathrm{j}\lambda^2 z}, \qquad t \to -\infty. \tag{3.35}$$

Due to the additional factors, these boundaries are not consistent with the boundary conditions (3.19) and (3.20) and hence are not canonical eigenvectors, if evolved according to (3.8) [10]. To circumvent this, an additional variable $u^2(t,\lambda;z) = v^2(t,\lambda;z)e^{-2\mathrm{j}\lambda^2 z}$ (which is now exactly $v^2(t,\lambda)$ from (3.20)) can be used and propagated according to (3.9). This leads to the evolution equation w.r.t z at $t = \infty$

$$\frac{\partial u^2(t,\lambda;z)}{\partial z} = \begin{pmatrix} 0 & 0 \\ 0 & -4\mathrm{j}\lambda^2 z \end{pmatrix} u^2(t,\lambda;z) \tag{3.36}$$

and in turn

$$u_1^2(\infty,\lambda;z) = u_1^2(\infty,\lambda;0)$$

$$u_2^2(\infty,\lambda;z) = u_1^2(\infty,\lambda;0)e^{-4\mathrm{j}\lambda^2 z}.$$

By using (3.27) the NFT coefficients during transmission can be calculated according to

$$a(\lambda,z) = \lim_{t\to\infty} u_1^2(t,\lambda;z)e^{\mathrm{j}\lambda t} = \lim_{t\to\infty} u_1^2(t,\lambda;0)e^{\mathrm{j}\lambda t} = a(\lambda,0)$$

$$b(\lambda,z) = \lim_{t\to\infty} u_2^2(t,\lambda;z)e^{-\mathrm{j}\lambda t} = \lim_{t\to\infty} u_2^2(t,\lambda;0)e^{-\mathrm{j}\lambda t}e^{-4\mathrm{j}\lambda^2 z} = b(\lambda,0)e^{-4\mathrm{j}\lambda^2 z}.$$

Finally, the transfer function of the NFT spectra $q_c(\lambda)$ and $q_d(\lambda_k)$ is

$$H = e^{-4\mathrm{j}\lambda^2 z}. \tag{3.37}$$

3.2 Mathematical Methods for Solving the INFT

The inverse nonlinear Fourier transformation (INFT) is used to create the time-domain signal $q(t)$ from the nonlinear spectrum $q_c(\lambda), q_d(\lambda_k)$ at the transmitter (or the receiver, if a digital backpropagation is used). To do this, for example the Gelfand-Levitan-Marchenko integral equations (GLME) or the Riemann-Hilbert Factorization can be used.

GLME

The GLME-method is based on solving two coupled integral equations [11][43]. The GLME are:

$$\begin{aligned} K_1^*(\tau,\tau') + \int_{-\infty}^{\tau} L(\tau'+y)K_2(\tau,y)\mathrm{d}y = 0, \\ -K_2^*(\tau,\tau') + L(\tau+\tau') + \int_{-\infty}^{\tau} L(\tau'+y)K_1(\tau,y)\mathrm{d}y = 0, \end{aligned} \tag{3.38}$$

with $\tau \geq \tau'$ and $L(\tau) = L_c(\tau) + L_d(\tau)$, where

$$L_c(\tau) = \frac{1}{2\pi}\int_{-\infty}^{\infty} q_c(\lambda)e^{-\mathrm{j}\lambda\tau}\mathrm{d}\lambda,$$

and

$$L_d(\tau) = -\mathrm{j}\sum_{k=1}^{N} q_d(\lambda_k)e^{-\mathrm{j}\lambda_k\tau}.$$

After solving the GLME for $K_{1,2}(\tau,\tau')$, the resulting time signal is $q(t) = -2K_2^*(t,t)$.

Riemann-Hilbert Factorization

The Riemann-Hilbert factorization problem is based on the projection equations (3.23) and (3.24) [44][45][46], which are rearranged to

$$\begin{aligned} &\begin{pmatrix} V^1(t,\lambda) & V^2(t,\lambda) \end{pmatrix} \\ &= \begin{pmatrix} \tilde{V}^1(t,\lambda) & \tilde{V}^2(t,\lambda^*) \end{pmatrix} \begin{pmatrix} \frac{b^*(\lambda^*)}{a^*(\lambda^*)}e^{-2\mathrm{j}\lambda t} & \frac{1}{a^*(\lambda^*)} \\ \frac{-1}{a^*(\lambda^*)} & -\frac{b(\lambda)}{a^*(\lambda^*)}e^{-2\mathrm{j}\lambda t} \end{pmatrix}, \end{aligned}$$

where $V^{1,2}$ and $\tilde{V}^{1,2}$ are functions of $v^{1,2}$ and $\tilde{v}^{1,2}$, respectively. To solve this problem, a Riemann-Hilbert system consisting of $2N+2$ linear equations for $2N+2$ discrete and continuous canonical eigenvectors, which lead to

$$\begin{aligned} q^*(t) = 2\mathrm{j}\sum_{i=1}^{N} q_d(\lambda_k)e^{2\mathrm{j}\lambda_k t}V_2^1(t,\lambda_k) \\ -\frac{1}{\pi}\int_{-\infty}^{\infty} q_c(\lambda)e^{2\mathrm{j}\lambda t}V_2^1(t,\lambda)\mathrm{d}\lambda \end{aligned}$$

is used.

3.3 Numerical Methods

The non-linear Fourier coefficients can only be calculated analytically in certain cases. In order to be able to use the NFT in any case, the numerical approximation is necessary. In this chapter multiple numerical methods for the I-/NFT and discretizations shall be briefly summarized.
For the numerical methods, the signal $q(t)$ is sampled in the interval $[T_1, T_2]$. It is assumed that $q(t)$ for $t < T_1$ and $t > T_2$ is equal to zero. The signal is then sampled on a uniform grid $T_1 < T_1 + \epsilon ... < T_1 + M\epsilon = T_2$ with M being the number of steps and ϵ the step-width, leading to the sampled signal $q[k] = q[T_1 + k\epsilon]$ with $k = 0, ..., M$.

3.3.1 NFT

The algorithms for the NFT are used to either compute the Jost solution $v[M]$, to calculate the spectral coefficients according to (3.27), or used to directly compute the NFCs $a(\lambda)$ and $b(\lambda)$. Most numerical methods are based on a discretization of the ZSP or on a combination of known analytic solutions of the NFT.

Forward Discretization

The most straight forward algorithm is based on the well-known forward Euler method, which is a simple first-order Runge-Kutta method [47]:

$$y[k+1] = y[k] + \epsilon f(t[k], y[k]). \tag{3.39}$$

Using $y = v$ and

$$f(t[k], y[k]) = P[k]v[k] = \begin{pmatrix} -\mathrm{j}\lambda & q[k] \\ -q^*[k] & \mathrm{j}\lambda \end{pmatrix} v[k]$$

we have the so called *forwad discretization*

$$v[k+1] = v[k] + \epsilon P[k]v[k], \qquad k = 0, ..., M, \tag{3.40}$$

with

$$v[0] = \begin{pmatrix} 1 \\ 0 \end{pmatrix} e^{-\mathrm{j}\lambda T_1}.$$

Since this is a first order discretization, this algorithm is inaccurate, if not a very high number of samples is being used. This can be improved upon by using the *central difference iteration*

$$v[k+1] = v[k-1] + 2\epsilon P[k]v[k],$$

which is a second-order discretization. In general, higher order Runge-Kutta methods can be used, which however are computationally complex and will not be regarded here further.

Ablowitz-Ladik Discretization

Discretization can break symmetries, which makes a discretized version of an integrable equation no longer integrable. The Ablowitz-Ladik (AL) algorithm is an integrable discrete version of the NLSE [47]. First, (3.40) can be rewritten to

$$\begin{aligned} v[k+1] &= A_{\mathrm{FD}}[k]v[k], \quad k = 0, ..., M, \\ A_{\mathrm{FD}}[k] &= \begin{pmatrix} 1 & 0 \\ 0 & 1 \end{pmatrix} + \epsilon \begin{pmatrix} -\mathrm{j}\lambda & q[k] \\ -q^*[k] & \mathrm{j}\lambda \end{pmatrix}, \end{aligned} \tag{3.41}$$

$1 \pm \mathrm{j}\lambda\epsilon$ replaced to $e^{\pm \mathrm{j}\lambda\epsilon}$ for small ϵ. Also, set $z = e^{-\mathrm{j}\lambda\epsilon}$ and $Q[k] = q[k]\epsilon$, which leads to

$$A_{\mathrm{AL}}[k] = \begin{pmatrix} z & Q[k] \\ -Q^*[k] & z^{-1} \end{pmatrix}. \tag{3.42}$$

The Ablowitz-Ladik iteration is then

$$v[k+1] = \frac{1}{\sqrt{1+|Q[k]|^2}} A_{\mathrm{AL}}[k]v[k], \qquad v[0] = \begin{pmatrix} 1 \\ 0 \end{pmatrix} e^{-\mathrm{j}\lambda T_1}. \tag{3.43}$$

Here, an additional normalization factor is introduced to make the solution numerically more accurate. To compute $\frac{\mathrm{d}a(\lambda)}{\mathrm{d}\lambda}$ for the calculation of the discrete spectrum, (3.27) has to be derived:

$$\frac{\mathrm{d}a(\lambda)}{\mathrm{d}\lambda} = \left(v_1'[M] + \mathrm{j}t[M]v_1[M]\right) e^{\mathrm{j}\lambda t[M]}, \tag{3.44}$$

leading to the iteration

$$\begin{aligned} v'[k+1] &= A'_{\mathrm{AL}}[k]v[k] + A_{\mathrm{AL}}[k]v'[k] \\ v'[0] &= \begin{pmatrix} -\mathrm{j}t[0] \\ 0 \end{pmatrix} e^{-\mathrm{j}\lambda t[0]} \end{aligned} \tag{3.45}$$

with

$$A'_{\mathrm{AL}}[k] = \begin{pmatrix} -\mathrm{j}\epsilon z & 0 \\ 0 & \mathrm{j}\epsilon z^{-1} \end{pmatrix}.$$

Continuous Layer-Peeling

The continuous layer-peeling (CLP), also called Boffetta-Osborne algorithm, is based on a known, analytic, solution of rectangular pulses and approximating the signal $q(t)$ as piece-wise constant, leading to M individual rectangles. The layer-peeling property states that the NFT coefficients $a_{1,2}(\lambda)$ and $b_{1,2}(\lambda)$ of two non-overlapping pulses can be combined to $a(\lambda)$ and $b(\lambda)$.
By using the CLP, the NFT coefficients can be calculated directly [48]

$$\begin{pmatrix} a[k+1,\lambda] \\ b[k+1,\lambda] \end{pmatrix} = C[k,\lambda,q] \begin{pmatrix} a[k,\lambda] \\ b[k,\lambda] \end{pmatrix}, \qquad \begin{pmatrix} a[0,\lambda] \\ b[0,\lambda] \end{pmatrix} = \begin{pmatrix} 1 \\ 0 \end{pmatrix}, \tag{3.46}$$

with

$$C[k,\lambda,q] \triangleq \begin{pmatrix} x[k] & -\tilde{y}[k] \\ y[k] & \tilde{x}[k] \end{pmatrix}, \qquad \det C[k,\lambda,q] = 1 \tag{3.47}$$

and

$$x[k] = \left(\cos(D\epsilon) - \mathrm{j}\frac{\lambda}{D}\sin(D\epsilon)\right) e^{\mathrm{j}\lambda(t[k+1]-t[k])} \tag{3.48}$$

$$y[k] = \frac{-q^*[k]}{D}\sin(D\epsilon)e^{-\mathrm{j}\lambda(t[k+1]+t[k])}, \tag{3.49}$$

where $D = \sqrt{\lambda^2 + |q[k]|^2}$, $\tilde{x}[k](\lambda) = x^*[k](\lambda^*)$ and $\tilde{y}[k](\lambda) = y^*[k](\lambda^*)$.

Trapezoid Discretization

The trapezoid discretization [49] is a numerical discretization scheme, which is based on the trapezoid rule of numerical integration ($h = T/N$, $0 \leq n \leq N$, $t_n = hn$)

$$\int_0^T f(\tau)\mathrm{d}\tau \approx h \sum_{n=0}^{N} \frac{1}{2}(f(t_n) + f(t_{n-1})). \tag{3.50}$$

To find such an integral in the ZSP (3.15), first variables need to be changed to

$$\psi(t;\lambda) = \begin{pmatrix} \psi_1 \\ \psi_2 \end{pmatrix} = \begin{pmatrix} v_1^2 e^{\mathrm{j}\lambda t} \\ v_2^2 e^{-\mathrm{j}\lambda t} \end{pmatrix} \tag{3.51}$$

and Eq. (3.15) to

$$\begin{aligned} \frac{\partial}{\partial t}\psi &= \begin{pmatrix} 0 & q(t)e^{\mathrm{j}2\lambda t} \\ -q^*(t)e^{-\mathrm{j}2\lambda t} & 0 \end{pmatrix} \psi \\ &= P_{\mathrm{TD}}(t;\lambda)\psi. \end{aligned} \tag{3.52}$$

Now, consider $\frac{\mathrm{d}}{\mathrm{d}t}x(t) = f(t)x(t)$ with $x(0) = 1$, which has the unique solution $x(T) = \exp\left(\int_0^T f(\tau)\mathrm{d}\tau\right)$. The solution of (3.52) can now be approximated as

$$\psi(t) = \exp\left(\int_{-T_1}^{t} P_{\mathrm{TD}}(\tau;\lambda)\mathrm{d}\tau\right) \begin{pmatrix} 1 \\ 0 \end{pmatrix}, \tag{3.53}$$

which leads, using the trapezoid discretization, to the following iteration

$$\psi(t_{n+1};\lambda) \approx \exp\left(P_{\mathrm{TD}}(t_{n+1};\lambda)\frac{h}{2}\right) \exp\left(P_{\mathrm{TD}}(t_n;\lambda)\frac{h}{2}\right) \psi(t_n;\lambda). \tag{3.54}$$

By defining

$$w_{n+1} = \exp\left(P_{\mathrm{TD}}(t_{n+1};\lambda)h\right) w_n, \qquad w_0 = \exp\left(P_{\mathrm{TD}}(t_0;\lambda)\frac{h}{2}\right) \begin{pmatrix} 1 \\ 0 \end{pmatrix}, \tag{3.55}$$

where $\psi(t_n) \approx \exp\left(-P_{\mathrm{TD}}(t_n;\lambda)\frac{h}{2}\right) w_n$, one can start an iteration, which leads to

$$\begin{pmatrix} a_N(\lambda) \\ b_N(\lambda) \end{pmatrix} = \exp\left(-P_{\mathrm{TD}}(t_N;\lambda)\frac{h}{2}\right) w_N. \tag{3.56}$$

Eq. (3.55) shows that, due to the $\frac{h}{2}$ term, the trapezoid discretization is a sort of a mid-point sampling method. Then,

$$\exp\left(P_{\mathrm{TD}}(t_n;\lambda)h\right) = \begin{pmatrix} \cos\left(|q_n|h\right) & \sin\left(|q_n|h\right) e^{\mathrm{j}\Phi_n + \mathrm{j}2\lambda t_n} \\ -\sin\left(|q_n|h\right) e^{-\mathrm{j}\Phi_n - \mathrm{j}2\lambda t_n} & \cos\left(|q_n|h\right) \end{pmatrix} = Q_n^{(h)}, \tag{3.57}$$

with $\Phi_n = \arg(q_n)$. To find $\left(Q_n^{(h)}\right)'$ to compute $a'(\lambda)$, the reader is referred to [49].

Forward-Backward Method

All the algorithms mentioned above are very accurate to find the roots of $a(\lambda)$ and estimate the discrete eigenvalues' positions. However, computing the spectral amplitude $q_d(\lambda_k)$ and $b(\lambda_k)$ can be very inaccurate, especially for many eigenvalues or a small number of samples. To improve the detection of $b(\lambda_k)$, the projection equation (3.23) is considered with $a(\lambda_k) = 0$, which reduces to

$$v^2(t,\lambda) = b(\lambda)v^1(t,\lambda). \tag{3.58}$$

Now, it is possible to compute $b(\lambda)$ at any time step by running the iteration of $v^2(t,\lambda)$ forward and $v^1(t,\lambda)$ backwards in time. By approaching the solution from two sides up to an arbitrary time-sample m and combining the solutions, the numerical error can be reduced drastically. m is commonly chosen to be in the middle of the window. However, an optimized point can be chosen to improve the results [49][50].

Eigenvalue Search

To compute the full nonlinear Fourier spectrum, the positions of the discrete eigenvalues have to be known. These are the zeros of $a(\lambda_k)$ in $\mathbb{C}^+$. Two methods have been used and combined in this work to find find the eigenvalues, namely a *plane method* and a Newton-Raphson scheme [47]. To elucidate these methods, 4 eigenvalues shall be found at $\lambda_k = [-1.5 + 0.5\mathrm{j},\ -0.5 + 0.5\mathrm{j},\ 0.5 + 0.5\mathrm{j},\ 1.5 + 0.5\mathrm{j}]$.

In a first step, the continuous spectrum in the bandwidth $[-\frac{0.5\pi}{\epsilon}, ..., \frac{0.5\pi}{\epsilon}]$ (or the known signal bandwith) has to be computed. Afterwards, using Parseval's theorem (Eq. (3.30)) the maximum imaginary value of the eigenvalues can be obtained. This leads to the first step of a the plane method. The plane method straight forwardly computes $|a(\lambda)|$ inside the bandwidth and up to the maximum possible imaginary value on a coarse grid. If wells in this grid are found, in an arbitrary number of following steps the grid resolution gets increased to get a finer estimate of the eigenvalue position.
To reduce the number of iterations of the plane method, a Newton Raphson search method can be used

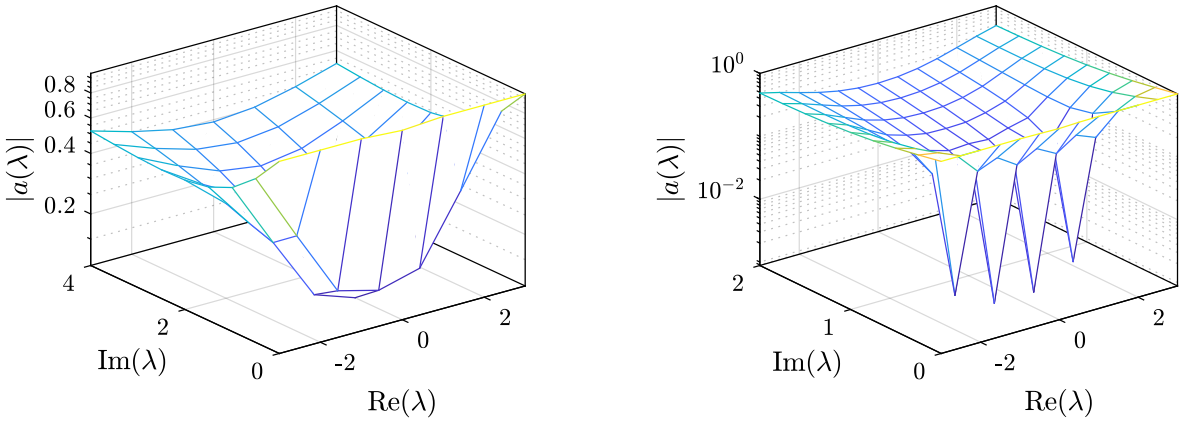

(a) Coarse grid, for rough estimation of eigenvalue positions.

(b) Finer grid on smaller plane.

Figure 3.3: Postive complex plane of λ of an exemplary pulse with $\lambda_k = [-1.5 + 0.5\text{j}, -0.5 + 0.5\text{j}, 0.5 + 0.5\text{j}, 1.5 + 0.5\text{j}]$.

to further improve the estimation of λ_i [47]. The method iteratively draws a gradient along

$$\lambda_{i,k+1} = \lambda_{i,k} - \frac{a(\lambda_{i,k})}{a'(\lambda_{i,k})}$$

with the iteration index k. The iteration stops after a maximum number of steps or when the remaining error $|a(\lambda_{i,k})/a'(\lambda_{i,k})|$ is smaller than a defined threshold. The plane method can be skipped altogether, if a rough estimate of the eigenvalues is known from the transmitter side and only the deviations due to e.g. noise needs to be known.

3.3.2 INFT

To transform a modulated NFT spectrum into a time domain signal $q(t)$ different algorithms can be used. Since this work focuses on solitons and the discrete spectrum, algorithms to transform the continuous spectrum shall only be discussed very briefly. The most commonly used algorithm to transform discrete eigenvalues into solitons is the Darboux transform, which shall be adressed in more detail.

INFT for the Continuous Spectrum

The continuous spectrum is assumed to be contained in the finite interval $[\Lambda_1, \Lambda_2]$ and discretized on a uniform grid with the step width μ $\Lambda_1 < \Lambda_1 + \mu, ... < \Lambda_1 + K\mu = \Lambda_2$ and $q_c[k] = q_c(\Lambda_1 + k\mu)$.

The Toeplitz inner bordering (TIB) algorithm is a solution of the GLME as given in (3.38), where the integrals are replaced with finite sums according to the trapezoidal rule. The reader is referred to [51] for a detailed solution of the TIB algorithm.

By inverting the Ablowitz-Ladik algorithm a signal can be reconstructed by running the algorithm backwards in time [52]. The resulting algorithm is also called discrete layer peeling [53]. To do this, the spectral coefficients $a(\lambda)$ and $b(\lambda)$ have to be computed, if only $q_c(\lambda)$ is given. Using the unimodularity condition

$$|a(\lambda)|^2+|b(\lambda)|^2= 1, \quad \lambda \in \mathbb{R} \tag{3.59}$$

one can solve by inserting $q_c = b/a$

$$\begin{aligned} 1 + |q_c(\lambda)|^2&= \frac{1}{|a(\lambda)|^2} \\ \Leftrightarrow |a(\lambda)|&= \frac{1}{\sqrt{1 + |q_c(\lambda)|^2}}. \end{aligned} \tag{3.60}$$

Now, the phase can be computed using the Hilbert transform $\mathcal{H}$ (similar to Kramers Kronig receivers [23][26]) as

$$\arg(a(\lambda)) = \mathcal{H}(\log|a(\lambda)|). \tag{3.61}$$

Having now $a(\lambda)$ and $q_c(\lambda)$, $b(\lambda)$ can be easily solved as $b = q_c a$. This leads to the backwards iteration

$$\begin{pmatrix} a[k] \\ b[k]z^{-(T_1/\epsilon+k)+0.5} \end{pmatrix} = \frac{1}{\sqrt{1 + |q[k]\epsilon|^2}} \begin{pmatrix} 1 & -q[k]\epsilon \\ q^*[k]\epsilon z & z \end{pmatrix} \begin{pmatrix} a[k+1] \\ b[k+1]z^{-(T_1/\epsilon+k+1)+0.5} \end{pmatrix}.$$

The time signal is then recovered as

$$Q^*[k] = -B_0[k+1]$$

where

$$B_0[k+1] = \frac{1}{\Lambda} \int_{\Lambda_1}^{\Lambda_2} b[k+1]z^{-(T_1/\epsilon+k+1)+0.5} e^{-2\mathrm{j}\epsilon\lambda} \mathrm{d}\lambda.$$

INFT for the Discrete Spectrum

To transform the discrete spectrum into a time-domain signal, as discussed above, the GLME can be used. A specialised algorithm which is able to transform only discrete eigenvalues into solitons at lower complexity as GLME or Riemann Hilbert methods is the Darboux transform. The Darboux transform takes one solution of an integrable equation ($q(t, z)$) and builds another solution ($\tilde{q}(t, z)$) on top. The complexity can then be nearly linear with regards to the amount of samples [53]. Summarized, the

Darboux transform in the framework of the NFT takes one known solution to the NLSE ($q(t,z)$) and creates a new solution according to [49]

$$\tilde{q}(t,z) = q(t,z) - 2\mathrm{j}(\lambda_0 - \lambda_0^*)\frac{\psi_2^*(t,z)\psi_1(t,z)}{|\psi_1(t,z)|^2+|\psi_2(t,z)|^2}, \tag{3.62}$$

where λ_0 is the newly added eigenvalue and $\psi(t,z)$ is a function of $v^2(t,\lambda_0)$ (see. Eq. (3.20)). Now, the eigenvalues of $q(t,z)$ and λ_0 are eigenvalues of $\tilde{q}(t,z)$ [10][49].

To begin the Darboux transform the initialization parameters A_i and B_i for all eigenvalues ($\lambda_k, \quad k = 1 \dots N$) have to be set. They can be chosen arbitrarily, but have to fulfil [49]

$$q_d(\lambda_k) = (\lambda_k - \lambda_k^*) \prod_{k=1,k\neq i}^{N} \frac{\lambda_k - \lambda_k^*}{\lambda_k - \lambda_k} \times \frac{-B_i}{A_i}. \tag{3.63}$$

A_i can be set to be 1 and B_i solved from (3.63) accordingly [49]:

$$B_i = -\frac{q_d(\lambda_k)}{\lambda_k - \lambda_k^*} \prod_{k=1,k\neq i}^{N} \frac{\lambda_k - \lambda_k}{\lambda_k - \lambda_k^*}. \tag{3.64}$$

Using these parameters, the eigenvectors for each eigenvalue and the first step of the recursion can be calculated (where the step of the recursion is in the superscript):

$$v_i^0(t) = \begin{pmatrix} A_i e^{-j\lambda_k t} \\ B_i e^{j\lambda_k t} \end{pmatrix}. \tag{3.65}$$

To start the recursion an initial NLSE $q(t,z)$ needs to be known. This can either be a modified solution of an INFT, which transformed a continuous spectrum or, if no continuous spectrum is present, $q_0(t,z) = 0$ (with the step of the recursion in the subscript). If a full modulation of the spectrum is to be used, the time-domain signal resulting from a continuous INFT has to be taken into account when calculating the Jost solutions/eigenvectors. This shall not be explained here, since only the discrete spectrum will be used later on. More in-depth explanations on this can be found in [54]. The first step of the recursion ($r = 1$) then computes a time-domain signal, which is only dependent on one eigenvalue-eigenvector pair:

$$(\psi_{r,1}(t), \psi_{r,2}(t))^T = v_r^{(r-1)}(t) \tag{3.66}$$

$$\tilde{q}_r(t) = q_{r-1}(t) - 2j(\lambda_r - \lambda_r^*)\frac{\psi_{r,2}^*(t)\psi_{r,1}(t)}{|\psi_{r,1}(t)|^2 + |\psi_{r,2}(t)|^2}. \tag{3.67}$$

Afterwards the eigenvectors of the $N-r$ unused eigenvalues ($k = r+1 \dots N$) are getting an update. $v_{k,p}^{r-1}$ now stands for the p-th vector element of the eigenvector v_k (belonging to the eigenvalue λ_k) from the recursion step $r-1$.

$$\forall k \in [r+1, r+2, \dots, N]:$$

$$v_{k,1}^{r} = \left(\lambda_k - \lambda_r^* - \frac{(\lambda_r - \lambda_r^*)|\psi_{r,1}(t)|^2}{|\psi_{r,1}(t)|^2 + |\psi_{r,2}(t)|^2}\right) v_{k,1}^{r-1}(t) - \frac{(\lambda_r - \lambda_r^*)\psi_{r,2}^*(t)\psi_{r,1}(t)}{|\psi_{r,1}(t)|^2 + |\psi_{r,2}(t)|^2} v_{k,2}^{(r-1)}(t) \tag{3.68}$$

$$v_{k,2}^{r} = -\frac{(\lambda_r - \lambda_r^*)\psi_{r,2}(t)\psi_{r,1}^*(t)}{|\psi_{r,1}(t)|^2 + |\psi_{r,2}(t)|^2} v_{k,1}^{r-1}(t) + \left(\lambda_k - \lambda_r + \frac{(\lambda_r - \lambda_r^*)|\psi_{r,1}(t)|^2}{|\psi_{r,1}(t)|^2 + |\psi_{r,2}(t)|^2}\right) v_{k,2}^{(r-1)}(t) \tag{3.69}$$

$$v_k^r = (v_{k,1}^r, v_{k,2}^r)^T \tag{3.70}$$

This is followed by the second step of the recursion. Using $r = 2$, Eqs. (3.66) up to (3.70) will be repeated, until $r = N$.

3.3.3 Fast I-/NFTs and Higher Order Discretizations

The algorithms and work mentioned above were the first results of intensive research in the mathematical field of NFT. Despite all this, more accurate and, above all, faster methods must be found in order to eventually be able to perform near real-time calculations. First publications on this topic employ the so-called fast NFTs (FNFTs, equivalent to the fast Fourier transformation (FFT)) that have a much lower computational complexity ($\mathcal{O}(M \log^2 M)$) [55, 56, 57, 58, 59], which is already close to the complexity of the FFT ($\mathcal{O}(M \log M)$ [60]) compared to the methods mentioned above with $\mathcal{O}(M^2)$. In addition, the higher order discretisations such as shown in [57] offer a higher numerical accuracy and are nowadays the state of the art.

Similar to the fast NFTs, fast INFTs must also be found. A faster version of the Darboux transformation [49] has already been implemented here. Further, fast INFTs for the continuous spectrum and combined NFT spectra have been developed [60, 61, 62, 63], which lead to numerical complexities down to $\mathcal{O}(M(N \log^2 M))$, with N being the number of discrete eigenvalues.

3.4 NFT of Conventional Pulses and Signals

In order to visualise the NFT, various well known pulses and signals will now be transformed and illustrated.

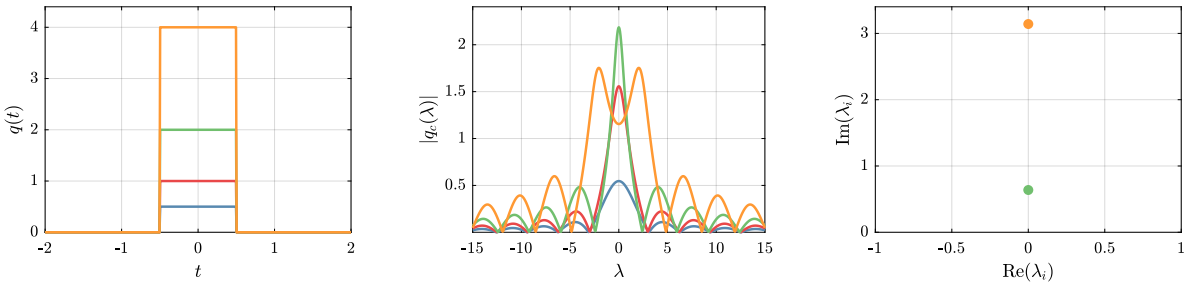

(a) Time-domain signals.

(b) Color-coded continuous spectra.

(c) Color coded discrete eigenvalues, no blue/red eigenvalues due to insufficient signal power.

Figure 3.4: Nonlinear Fourier transformations of rectangular pulses with a time width $T = 1$ and different amplitudes $A = 0.5$ (blue), 1 (red), 2 (green), 4 (orange).

3.4.1 Rectangular Pulse

The nonlinear tranformation of rectangular pulses

$$q(t) = \begin{cases} A,\ t \in [-T/2, T/2] \\ 0,\ \text{otherwise} \end{cases}$$

with different amplitudes is depicted in Fig. 3.4 and can also be computed analytically [10]. Here, one can see that for low powers, the continuous spectrum (depicted in Fig. 3.4b) indeed is similar to the spectrum of the conventional Fourier transform. However, if the amplitude doubles from $A = 0.5$ to $A = 1$, the peak amplitude of the continuous spectrum increases roughly by a factor of 3. A further increase in amplitude of the rectangular pulse causes less increase of the continuous spectrum, but instead lead to an emerging eigenvalue (as depicted in Fig. 3.4c). If the amplitude gets increased even further, the shape of the continuous spectrum gets disconnected from the conventional Fourier spectrum with even higher imaginary parts of the eigenvalues. If the amplitude of the rectangular signal is fixed and instead the width increases (depicted in Fig. 3.5a), one can see that even though the bandwidth of the main lobe in the continuous spectrum (depicted in Fig. 3.5b) decreases, the amplitude changes with additional eigenvalues emerging (Fig. 3.5c).

This exemplarily shows that discrete eigenvalues are not only dependent on the amplitude of the time-domain signal, but also from the width, i.e. total signal power. This can be problematic, especially if very long blocks of transmission shall be transformed, since many discrete eigenvalues have to be considered and their exact positions to be determined.

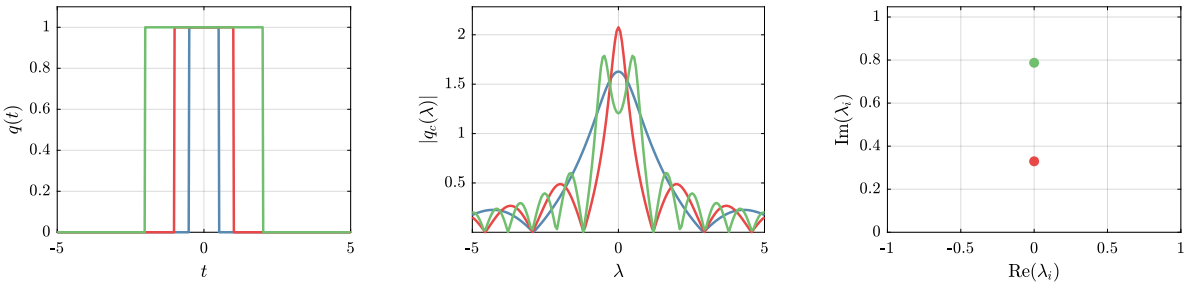

(a) Time-domain signals.

(b) Color-coded continuous spectra.

(c) Color coded discrete eigenvalues, no blue eigenvalue due to insufficient signal power.

Figure 3.5: Nonlinear Fourier transformations of rectangular pulses with an amplitude $A = 1$ and different widths: $T = 1$ (blue), 2 (red), 4 (green).

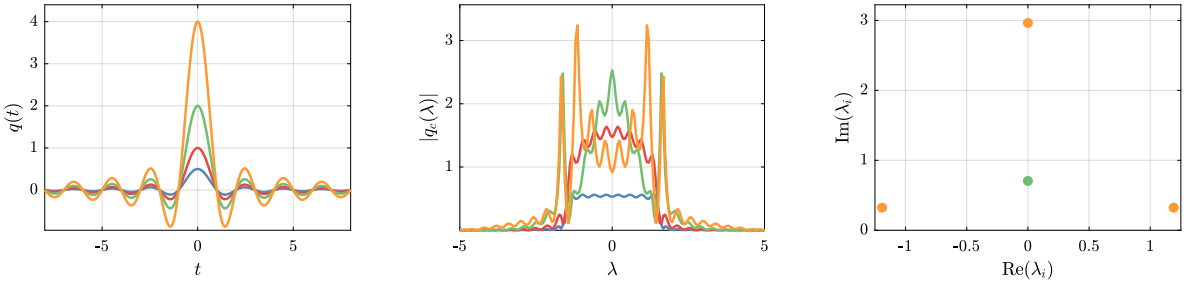

(a) Time-domain signals.

(b) Color-coded continuous spectra.

(c) Color coded discrete eigenvalues.

Figure 3.6: Nonlinear Fourier transformations of sinc-pulses ($q(t) = A \cdot \frac{\sin(t/\pi)}{(t/\pi)}$) and different amplitudes A=0.5 (blue), 1 (red), 2 (green), 4 (orange).

3.4.2 Si Pulse

Fig. 3.6 shows the non-linear transformation of sinc ($\sin(x)/x$) pulses. Here, for low powers the resulting spectrum is rectangular, and also shows the Gibbs phenomenon known from the linear transformation. But again, as the amplitude increases, the continuous spectrum changes and discrete eigenvalues emerge, which can also have a real-part.

3.4.3 Conventional Signals

To exemplarily investigate the nonlinear Fourier spectra of conventional linearly modulated transmissions, blocks of 16, 32 and 64 symbols with a symbol rate of 56 GBaud were transmitted over 12 spans of 80 km SSMF using lumped amplification. The symbols were modulated using a 16-QAM modulation format and shaped by a root-raised cosine filter with a roll-off factor of 0.1. Fig. 3.7 summarises the results.

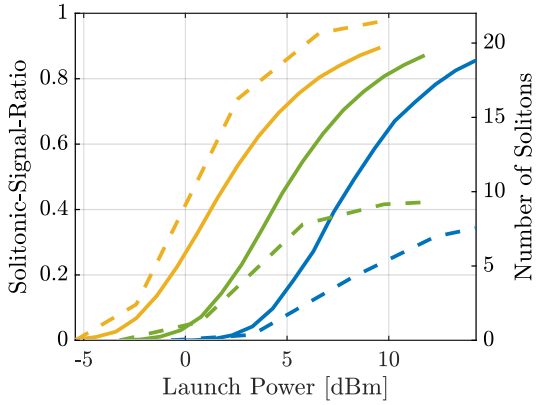

(a) Solitonic-signal-ratio (solid lines) and average number of solitons (dashed lines) for the conventional transmission format after transforming blocks of 16 (blue), 32 (green) and 64 (yellow) symbols.

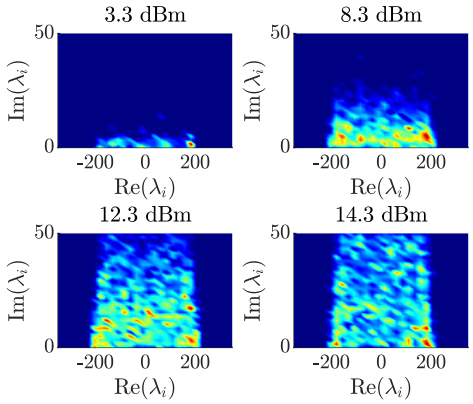

(b) Histogram of discrete eigenvalue positions after transforming 500 blocks of 16 symbols for different average block launch powers.

Figure 3.7: Properties of the nonlinear spectrum after transmission of a conventional signal with regards to discrete eigenvalues. The SSR and number of eigenvalues is not only dependent on the average launch power, but also the block length.

With increasing average launch power of the symbol blocks, the ratio of power stored in solitons to power in the continuous spectrum (here called solitonic-signal-ratio (SSR)) increases (Fig. 3.7a). In the simulations, the SSR asymptotically reaches 0.9. With rising SSR, the amount of discrete eigenvalues rises asymptotically, too [12]. This is shown by the dashed lines in Fig. 3.7a. To get an insight into the discrete eigenvalues' positions, Fig. 3.7b shows histograms of the positions after transforming 500 blocks of 16 symbols. Here, one can see that not only the eigenvalues span over the whole bandwidth of the transmission (here: $\lambda = [-200, ..., 200]$) but also get increasing imaginary parts with increasing launch-power. This can lead to problems, if e.g. a digital back-propagation in the NFT domain is intended, since to do this very exact knowledge of the eigenvalues' positions is needed. This can lead to the need for very large a-planes with very fine resolutions and hence high computational complexity.

However, the importance of solitons also for conventional transmission scenarios cannot be emphasised enough here. If signal powers in the highly non-linear regime are to be targeted at some point, the resulting signals will consist largely of solitons. Therefore, it is important to treat and understand solitons also in the NFT framework.

Chapter 4

Soliton Modulation and Multiplexing

As shown in the last section, very high power transmissions are mainly comprised of solitons. Hence, a deeper look into solitons in the framework of the NFT shall be given. This includes physical properties of eigenvalue modulation, where the impact of eigenvalue modulation on the time-domain soliton, also of higher order created by the Darboux transform, is reviewed. Afterwards linear multiplexing of solitons, which can reduce the hardware requirements will be discussed in depth. This is followed by a section about the impact of noise during transmission on the discrete, solitonic NFT spectrum.

4.1 Soliton Transmissions in the Framework of the NFT

Early soliton transmissions in the 1980s to 1990s were based on on-off keying of solitons and direct detection. These transmissions suffered from timing jitters caused by collisions between WDM channels [16][15] and EDFA noise [64][65]. As described in Chapter 2.1.5, collisions between solitons in a system using lumped EDFA amplification lead to timing shifts, if the collisions are not spread over multiple spans [16]. This effect was further amplified because the number of collisions was directly influenced by the OOK modulation of the individual channels and was therefore dependent on the data sent. The noise of the EDFAs can minimally change the center frequency of a soliton, which can also lead to random runtime differences. This effect can also be observed in single-channel transmissions and is also called Gordon-Haus jitter [64][65].

To circumvent some of these effects, Hasegawa *et al.* [66] proposed adiabatic dispersion profiles. By reducing the dispersion between two amplifiers, the ratio between dispersion and non-linearities remains almost stable and an improvement in the transmission characteristics is achieved. These sorts of transmissions where realised using dispersion decreasing fiber maps or even dispersion compensating

fibers and were called *dispersion managed solitons* [17, 67, 68, 69, 70].
The idea of dispersion management is still relevant today, as dispersion decreasing fibers entail an exact solution of the NFT, despite fiber losses [71][72].

The term eigenvalue communication was first used by Hasegawa *et al.* in 1993 [73, 74]. Here, the idea of transmitting data not on individual solitons but on discrete eigenvalues of the ZSP scattering problem was already proposed (which was already an early stage of NFT transmission) and up to three eigenvalues were modulated by on-off keying. However, due to the aforementioned problems, soliton transmission, and with it eigenvalue communication, did not initially gain traction.

Only with the help of coherent detection and improved digital signal processing (DSP) possibilities did eigenvalue communication, now referred to as NFT transmission, gain in significance [75, 76]. Several eigenvalues were complexly modulated using the NFCs, which increased the spectral efficiency compared to on-off keying (OOK) [77, 78, 79, 80]. Other approaches use first-order solitons with very high-order modulation types [81, 82] or expanded the soliton modulation to multiple polarizations [83, 84, 85, 86]. This was quickly followed up by first developments of equalization techniques based on the NFT spectrum [81, 87, 88, 89, 90].

4.2 Physical Properties of Eigenvalue Modulation

In this section the impact of different modulation degrees of freedom of the discrete NFT spectrum onto time-domain solitons shall be descibed. Especially if higher order solitons are taken into account, the resulting pulses and their propagation are non-trivial.

4.2.1 First Order

A first order soliton can be analytically described by

$$q(t) = -2\mathrm{j}\mathrm{Im}(\lambda_i) e^{-\mathrm{j}\angle q_d(\lambda_i)} \mathrm{sech}\left(2\mathrm{Im}(\lambda_i)\left(t - \frac{1}{2\mathrm{Im}(\lambda_i)} \ln\left(\frac{|q_d(\lambda_i)|}{2\mathrm{Im}(\lambda_i)}\right)\right)\right) e^{-2\mathrm{j}\mathrm{Re}(\lambda_i)t}. \tag{4.1}$$

To denormalize the solitons properties from dimensionless NFT units into physical units, an arbitrarily chosen time parameter T_0 can be chosen. From (4.1), one can see that the imaginary part of the discrete eigenvalue linearly modulates the amplitude, as well as the width of the soliton as depicted in Fig. 4.1a. Since the width decreases linearly with the imaginary part of the eigenvalue, the bandwidth increases linearly. For this reason, the imaginary value of a first order soliton does not change the spectral efficiency. The physical width of a soliton is $2\mathrm{Im}(\lambda_i)T_0$. If $\mathrm{Im}(\lambda_i) = 0.5$, this leads to a soliton with a characteristic time-width (see Eq.(2.12)) equal to the normalization parameter. The real part of the

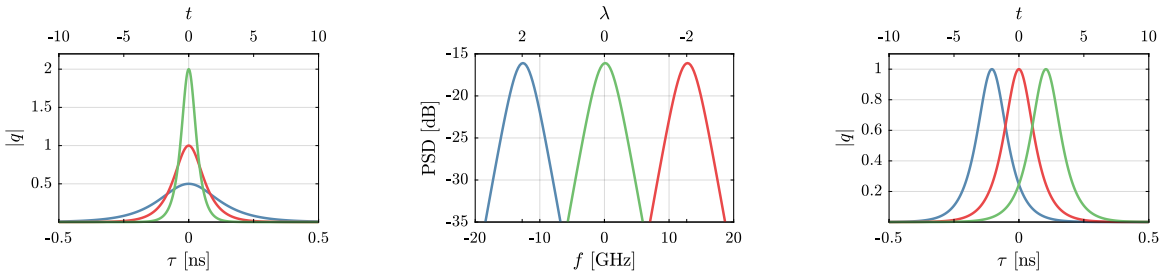

(a) Modulation of $\mathrm{Im}(\lambda_i)$: 0.25j (blue), 0.5j (red), 1j (green).

(b) Modulation of $\mathrm{Re}(\lambda_i)$: 2 (blue), 0 (green), 2 (red).

(c) Modulation of $|q(\lambda_i)|$: 1/8 (blue), 1 (red), 8 (green)

Figure 4.1: Resulting soliton pulses in time- and linear frequency domain after modulation of (a) the imaginary part of λ_i, (b) the real part of λ_i and (c) the amplitude of $q_d(\lambda_i)$. Top x-axis represents the normalized NFT units and bottom x-axis physical units, denormalized by $T_0 = 50\,\mathrm{ps}$.

eigenvalue modulates the center frequency of the soliton, which is transformed by (see also Fig. 4.1b)

$$\Delta f = -\frac{\mathrm{Re}(\lambda_i)}{\pi T_0}. \tag{4.2}$$

Finally, the discrete spectral parameter $q_d(\lambda_i)$ gives rise to the phase of the soliton and (together with the imaginary value of λ_i) to the position inside the time-window t_0 (as depicted in Fig. 4.1c), since $|q(\lambda_i)|$ changes t_0 logarithmically, $|q(\lambda_i)| \overset{!}{>} 0$. Moreover, it is advantageous to modulate $|q(\lambda_i)|$ nonlinearly, to get an equal distribution inside the time window. Hence, commonly amplitude phase-shift keying (APSK) based modulation formats are being chosen where the unipolar, linear amplitudes A_{APSK} are modulating $|q(\lambda_i)|$ according to $|q(\lambda_i)| \in e^{A_{\mathrm{APSK}}}$. In physical units, the time shift can be described as

$$\Delta\tau = \ln(|q_d|) \cdot \frac{1}{2\mathrm{Im}(\lambda_i)} \cdot T_0. \tag{4.3}$$

4.2.2 Higher Order

If multiple discrete eigenvalues are multiplexed using an INFT, nonlinear solutions arise which are not as straight forwardly described as a first order soliton. Analytical solutions can so far only be derived for a soliton consisting of up to two eigenvalues. Hence, numerical algorithms to solve the INFT have to be employed.

The first questions to be answered for designing a higher order soliton system is how the eigenvalues shall be placed inside the complex plane. If e.g. the eigenvalues are "stacked" (they have the same real part) with different imaginary parts, the influence of the highest eigenvalue leads to a very broad

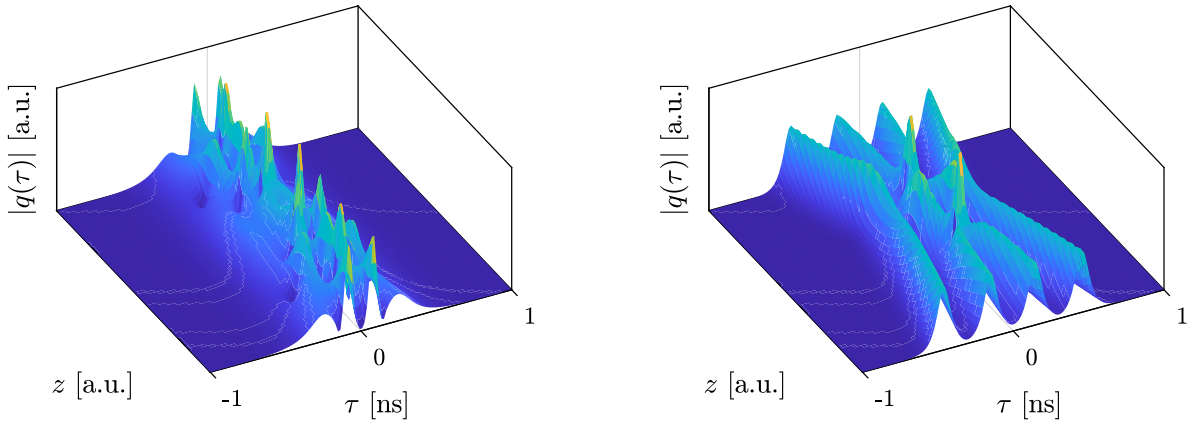

(a) Vertical stacking: $\lambda_i = (1\mathrm{j}\ 2\mathrm{j}\ 3\mathrm{j}\ 4\mathrm{j})$

(b) Horizontal stacking

Figure 4.2: Fourth order solitons during transmission according to Eq. (3.37) with different multiplexing schemes.

bandwidth and high peak-to-average power ratios. However, all eigenvalues stay at their transmitted position in the retarding time-window. Contrary, if the eigenvalues are placed "next to each other" (with the same imaginary part) on different real parts, the overall signal bandwidth can rise due to different center frequencies. Additionally, the eigenvalues travel with different speeds and will escape the retarding time window after a certain transmission distance.

This is depicted in Fig 4.2, where four eigenvalues are stacked vertically with the same real-part and $|q_d(\lambda_i)|= 1$ (Fig. 4.2a) and stacked horizontally with the same imaginary part (Fig. 4.2b) and different $|q_d(\lambda_i)|$ to get separated pulses at Tx. For comparisons sake, the eigenvalues were chosen such that the average powers and bandwidths of the resulting solitons are on average the same. All eigenvalues were transmitted with the same phase and then propagated along a normalized fiber according to Eq. (3.37). One can see that during transmission the shape of a vertically stacked fourth order soliton varies strongly. Besides strongly varying peak-to-average power ratios, this also has an effect on the linear bandwidth. This in turn leads to different time-bandwidth products during transmission. In contrast, horizontally stacked solitons merge and separate during transmission leading to more stable time-bandwidth products, if not at a point of collision. In summary, the multiplexing of eigenvalues is a very sophisticated optimization problem [91].

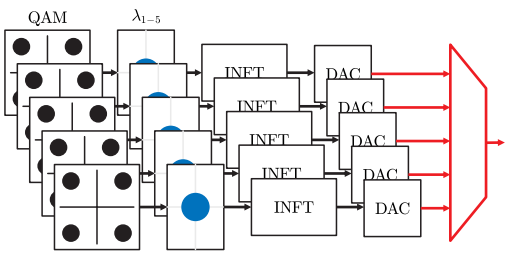

(a) Linear multiplexing of solitons. Each INFT creates one modulated single order soliton.

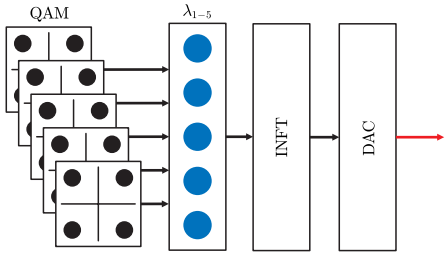

(b) Nonlinear multiplexing of solitons. One INFT creates one modulated higher order soliton.

Figure 4.3: Visualization of both used multiplexing schemes.

4.3 Linear multiplexing

In general, very high order solitons can have high requirements on the DAC and also ADC hardware such as high sampling rates, bandwidths and quantization resolutions. To circumvent this, one solution not only to keep the hardware requirements lower, but also fill the whole frequency band with solitons is linear multiplexing [92][93]. In this work, linear multiplexing of solitons means creation and modulation of simple first-order solitons in the digital domain and a following DAC and E/O conversion. Afterwards, the solitons can be linearly multiplexed by an optical coupler. This is depicted in Fig. 4.3a. This is in contrast to digital multiplexing by e.g. the Darboux transformation and subsequent D/A conversion of a higher order soliton as depicted in Fig. 4.3b.

However, linearly multiplexing solitons contradicts the fact that solitons are a result of a nonlinear evolution equation such as the NLSE. In other words: If two solitons, which have their temporal middle centered above each-other shall still be a solution to the NLSE, their centering has to be a result of a collision during evolution through the NLSE. This obviously leads to nonlinear interactions, which cannot be described by a simple addition. The superposition of fields does not correspond to a superposition in the NFT domain, as opposed to the linear Fourier transform. Hence, the use of an INFT to compute the result "nonlinear collision" and conserve the eigenvalues and NFT coefficients is needed. Mind that this collision would only occur for solitons with the same center frequency (i.e. $\mathrm{Re}(\lambda_1) = \mathrm{Re}(\lambda_2)$) for very specific scenarios. However, the INFT still calculates such a case.

4.3.1 Effects of Linear Multiplexing

In this section, the effects of linear multiplexing on the resulting solitons and their eigenvalues in the NFT domain shall be discussed. Superposing multiple solitons can lead to a modification of their propagation properties and in turn change of discrete eigenvalues, and also has an impact onto the continuous

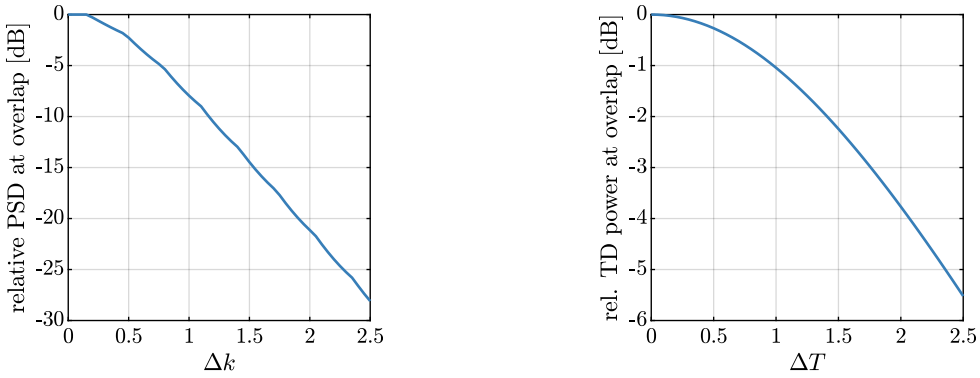

(a) PSD (relative to peak) at which the spectra of the solitons overlap depending on Δk.

(b) Time-domain power (relative to peak-power) at which the solitons overlap depending on ΔT.

Figure 4.4: Visualization of multiplexing density depending on Δk and ΔT.

spectrum. To explain this, we will start with superposing two eigenvalues $\lambda_{m,n}$ and their spectral amplitudes $q_d(\lambda_{m,n})$. To fully conserve the eigenvalues' properties, one of two boundary conditions have to be met. The first boundary condition is the time difference between the solitons. If this is chosen to be very high, the propagation of the solitons resembles that of a solitary fundamental soliton transmission using only one carrier with

$$\lim_{\Delta T_{m,n}\to\infty}(\Delta\hat{\lambda}_{m,n}) = 0, \tag{4.4}$$

where $\Delta T_{m,n} = |T_m(q_{d,m}, \mathrm{Im}(\lambda_m)) - T_n(q_{d,n}, \mathrm{Im}(\lambda_n))|$ is the time difference between the center positions $T_{m,n}$ of the solitons and $\Delta\hat{\lambda}_{m,n}$ is the deviation of λ_m after superposition with λ_n.
The second condition is the frequency spacing in linear Fourier domain. If this value is high, a WDM-like transmission is present with

$$\lim_{\Delta k_{m,n}\to\infty}(\Delta\hat{\lambda}_{m,n}) = 0, \tag{4.5}$$

where $\Delta k_{m,n}$ is the difference between the real-part of the eigenvalues.
To visualize this concept, Fig. 4.4 shows the PSD and time domain power (relative to the respective peaks) at the point where the solitons overlap. For example, if Δk is set to 1, the PSD of the solitons is attenuated by 8 dB relative to the peak. Or, to have the solitons overlap in the time domain at their FWHM point (-3 dB), a ΔT of 1.763 must be chosen.
In summary, four effects, depending on the frequency- (Δk), time- (ΔT) and phase- ($\Delta\phi$) offsets between two eigenvalues can occur after superposing multiple eigenvalues, which are *co-propagation*, *fusion*, *merging* and *destruction* [93, 94] and will be discussed in the next section.

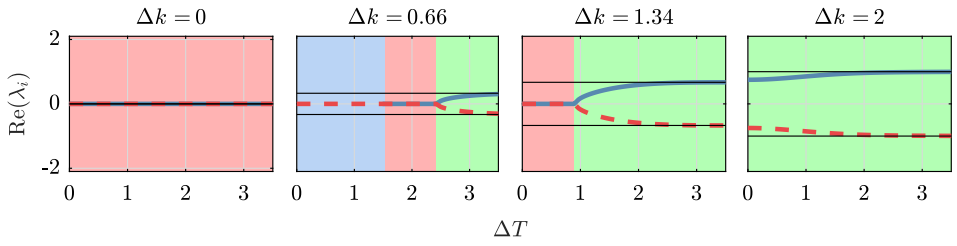

Figure 4.5: Real parts of two eigenvalues (blue/red lines) after superposition depending on Δk and ΔT, $\Delta\phi = 0$. Black lines show the real parts before superposition. Red underlay shows soliton co-propagation, blue stands for soliton fusion and green for soliton merging.

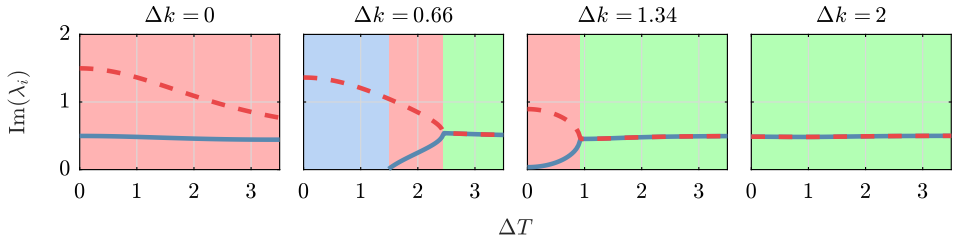

Figure 4.6: Imaginary parts of two eigenvalues (blue/red lines) after superposition depending on Δk and ΔT, $\Delta\phi = 0$. Red underlay shows soliton co-propagation, blue stands for soliton fusion and green for soliton merging.

Two Eigenvalues

To exemplarily demonstrate the eigenvalue positions after multiplexing, Figs. 4.5 and 4.6 give a closer look onto the eigenvalues' developments in dependence on the multiplexing parameter ΔT. Here, Δk and $\Delta\phi$ were fixed, while ΔT is swept. In the figures, one can see that for $\Delta k = 0$ a co-propagation results for all $\Delta T \in [0; 3.5]$. In the case of co-propagation, multiplexing two eigenvalues results in a higher-order soliton with two vertically stacked eigenvalues on the same frequency as depicted in Fig. 4.7a. This can also happen, if the eigenvalues had originally different real-parts as can be seen in Figs. 4.5 and 4.6 for $\Delta k = 0.66$ or 1.34. The resulting eigenvalues co-propagate at the same speed through an optical fiber with a repeating pulse shape after shedding the energy stored in the continuous spectrum.

At $\Delta k = 0.66$ for very low ΔT a fusion occurs (blue underlay) with one very high eigenvalue. If a fusion occurs, the eigenvalues fuse into one eigenvalue with high imaginary value as depicted in Fig. 4.7b, which again results in a resonating soliton. With increasing $\Delta T = 0$, the eigenvalues' imaginary part lowers, until at $\Delta T \approx 1.5$ a very low power eigenvalue emerges, leading again to a co-propagation. Both eigenvalues now converge, until they "collide" at $\Delta T \approx 2.4$, as depicted in Fig. 4.8a. One can see that at a point of colliding eigenvalues, very small changes in ΔT lead to relatively large steps in the eigenvalue development. In fact, the eigenvalues do not touch, but jump from a co-propagation into the merging phenomenon.

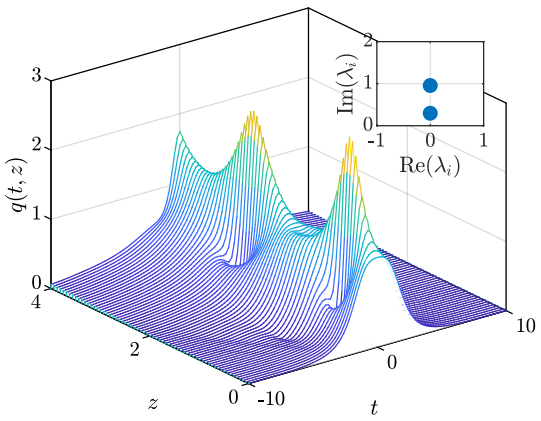

(a) Co-propagation resulting from $\Delta T = 2T_0$, $\Delta\phi = 0$, $\Delta k = 0.5$.

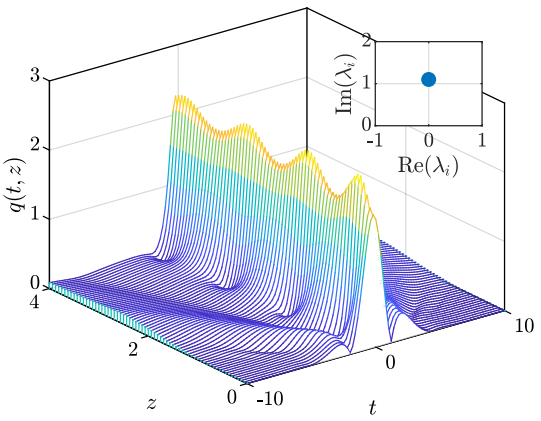

(b) Fusion resulting from $\Delta T = 0$, $\Delta\phi = \pi/4$, $\Delta k = 1$.

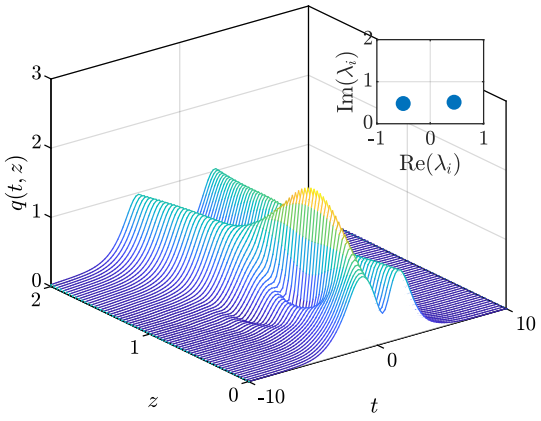

(c) Merging resulting from $\Delta T = 3T_0$, $\Delta\phi = \pi/2$, $\Delta k = 1$.

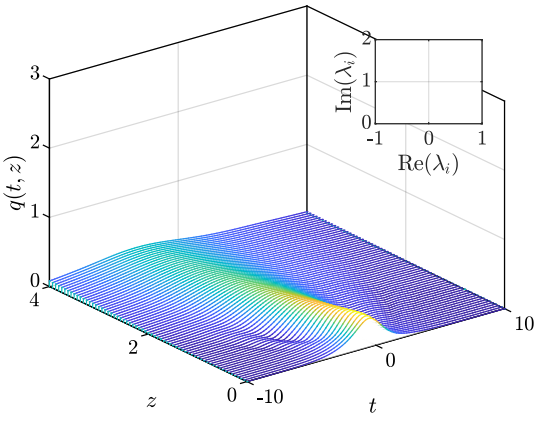

(d) Merging resulting from $\Delta T = 0.25T_0$, $\Delta\phi = 2.78$, $\Delta k = 0.1$.

Figure 4.7: Resulting linear multiplexing phenomena during transmission: (a) Co-Propagation, (b) Fusion, (c) Merging, (d) Destruction. The inset shows the resulting eigenvalues after linear multiplexing of $\lambda_{m,n} = \pm\frac{\Delta k}{2} + 0.5\text{j}$.

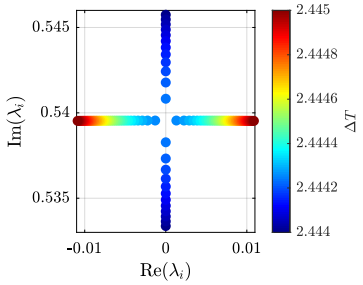

(a) Resulting eigenvalues for changing ΔT and fixed $\Delta k = 0.66$ and $\Delta\phi = 0$. ΔT step length between dots is $2.13e-5$.

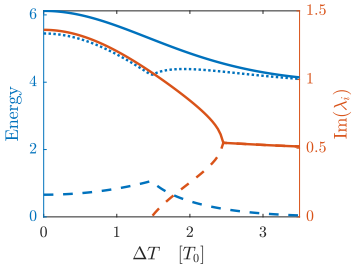

(b) (Blue:) Energy distribution of the NFT spectra: (dotted) continous spectrum, (dashed) discrete spectrum, (solid) both spectra. (Red:) Imaginary part of the eigenvalues depending on ΔT.

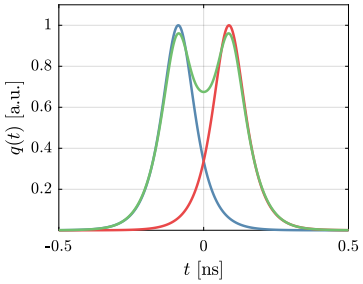

(c) Two first order solitons (blue, red) and their linear superposition result for $\Delta T = 3.5$ and $\Delta k = 0.66$.

Figure 4.8: Detailed view onto developments of (a) the discrete spectrum and (b) energy distribution of the NFT spectra after linear superposition, as well as (c) resulting time-domain soliton after dense multiplexing.

In the case of merging, the eigenvalues stay on different real-parts and merge inside the fiber due to different group velocities and eventually separate before merging with other eigenvalues (see Fig. 4.7c). As already stated in (4.4) and (4.5), if perfect merging occurs, the eigenvalues keep their position from before superposition. For smaller ΔT and Δk the eigenvalues' positions change and with increasing superposing parameters asymptotically reach their position before superposition. If a merging transmission is used, straight forward data de-/modulation is possible if e.g. the eigenvalues themselves (e.g. on-off-keying) are used as data carriers, since the amount of eigenvalues and spectral center positions are constant. If a modulation of the spectral amplitude is desired, further conditions have to be met as will be discussed later.

To calculate the dispersive wave energy after linear superposition Eqs. (3.30) and (3.32) can be used. Fig. 4.8b shows that as soon as a merging occurs, the amount of dispersive energy is very low and reaches 0 in this example with $\Delta T = 3.5$ and $\Delta k = 0.66$. The resulting time-domain pulse at this point is depicted in Fig. 4.8c.

The last superposition phenomenon is the destruction, which is a result of inversely phased addition with close frequency spacing and resulting destructive interference.

To give an overview over the needed soliton spacings for the resulting phenomena, Fig. 4.9 shows a three dimensional representation of the outcomes. If e.g. a merging in combination with a phase modulation of the solitons is desired and no control over the time-difference is possible (i.e. $\Delta T = 0$), a Δk of 1.53 is needed. In this case, independent of $\Delta\phi$, merging results. If, however, denser multiplexing in frequency domain is preferred (i.e. $\Delta k = 0.5$), ΔT has to be increased to at least three, to again gain a phase

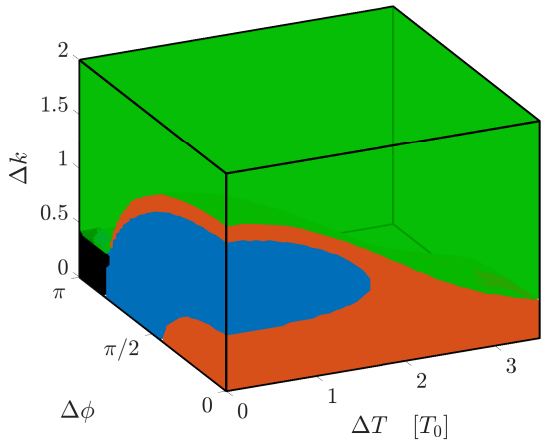

Figure 4.9: Three dimensional representation of the outcome of two-eigenvalue combinations depending on Δk, ΔT and $\Delta\phi$. Green stands for merging, red for co-propagation, blue for fusion and black for destruction.

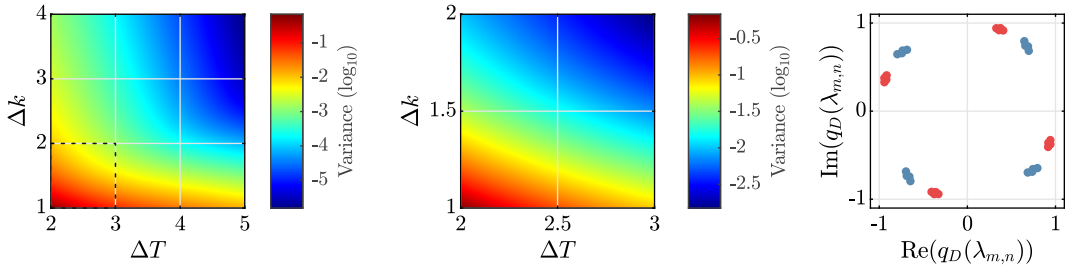

Figure 4.10: Variance of $q_D(\lambda_{m,n})$ after linear multiplexing, depending on ΔT and Δk. (left) The phase-independent merging regime until close to perfect merging occurs. (middle) Zoomed in version of left plot, indicated by dashed box. (right) Resulting $q_D(\lambda_{m,n})$ (colorcoded) at $\Delta T = 2.5$ and $\Delta k = 1.5$.

independent merging.

The most straight-forward way to use linear multiplexing in this framework, is merging with a modulation of the NFT coefficients. If the amplitude (here: time-shift) is to be modulated, the unmodulated ΔT has to be increased accordingly. However, to also modulate the phase, one has to look not only at the impact of the superposition on the eigenvalues, but also on the phase. This is depicted in Fig. 4.10. Derived from this, a combination of $\Delta T = 2.5$ and $\Delta k = 1.5$ leads to a variance of $q_D(\lambda_{m,n})$ in the region of 1e−1.5, which is negligible in a noisy environment.

Extension to Four Eigenvalues

If more than two eigenvalues are being used for information transmission, multiple superposition phenomena can occur at the same time. This is exemplarily depicted in Figs. 4.11 - 4.12 for different

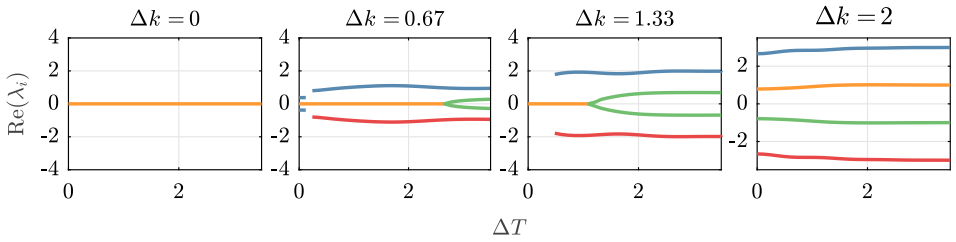

Figure 4.11: Real parts of four eigenvalues (orange/green/red/blue lines) after superposition depending on Δk and ΔT, $\Delta\phi = 0$.

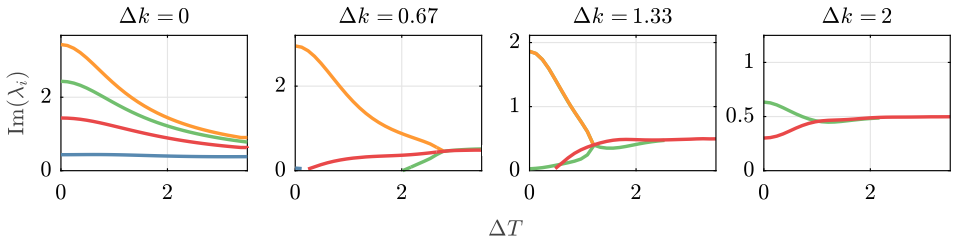

Figure 4.12: Imaginary parts of four eigenvalues (orange/green/red/blue lines) after superposition depending on Δk and ΔT, $\Delta\phi = 0$.

fixed Δk, $\Delta\phi = 0$ and swept ΔT. If $\Delta k = 0$ a full co-propagation of four eigenvalues occurs for all $\Delta T \leq 3.5$. This changes after increasing Δk to 0.67. Here, the two middle eigenvalues fuse until $\Delta T = 2$, whereafter they form a co-propagation, which finally changes into merging at $\Delta T \geq 2.6$. Meanwhile, the outermost eigenvalues are in a merging constellation from $\Delta T = 0.25$ onwards with increasing imaginary parts. If $\Delta k = 2$, all eigenvalues are merging independently of the time difference. However, for low ΔT, an energy transfer between eigenvalues occurs, leading to higher/lower eigenvalues.

4.3.2 Requirement Reduction Using Linear Multiplexing

To evaluate a possible gain by multiplexing solitons linearly, five bit streams were mapped into 4-QAM symbols and subsequently fed into five parallel INFTs, which created first order solitons with eigenvalue positions according to Tab. 4.1. The fixed spectral shift of 10 GHz in linear Fourier domain led to

Table 4.1: Eigenvalue and Soliton Properties from [93]

Eigenvalue	Position	Spectral Shift	Time Delay
1	$-1.1344 + 0.5$j	20 GHz	250 ps
2	$-0.5672 + 0.5$j	10 GHz	125 ps
3	0.5j	0	0
4	$0.5672 + 0.5$j	-10 GHz	-125 ps
5	$1.1344 + 0.5$j	-20 GHz	-250 ps

$\Delta k = 0.5672$. The width of each pulse was $T_0 = 17.82\,\text{ps}$, which leads in combination with physical unit time delays of 125 ps to $\Delta T = 7.24$. Hence, in this simulations the frequency difference was chosen to be small and the timing difference to be high. This leads to more stable conditions during transmissions, due to longer collision distances as described in Section 2.1.5. After transmission through a 200 km SSMF, which included one collision of the solitons, the eigenvalues were split using narrow filters (19 GHz bandwidth) and received independently. After A/D conversion ($f_s = 160\,\text{GS/s}$, 8 bit quantization), each single order soliton was either computed using one NFT or directly sampled at the peak to regain the phase.

This was compared to a transmitter using digital multiplexing of solitons by employing one 5-eigenvalues Darboux transform as INFT, with the same eigenvalue parameters as the linear multiplexing transmitter. Since an eigenvalue-based demodulation using one large NFT was not possible with the used NFT methods, a brute-force correlation of the received pulses with training sequences was done to show a possible data transmission. Additionally, all filter bandwidths in the broad-band case were increased to 65 GHz to regain all eigenvalues. Fig. 4.13 shows an excerpt of the results from [93]. For Fig. 4.13a all devices' parameters were set as before, but the bandwidths of Tx and Rx filters were changed. It can be seen that for the parallel transmitter variant bandwidths as low as 16.5 GHz were sufficient to reach BERs below the hard-decision forward error correction (HD-FEC) limit of BER = 3.8e−3. Here, simple sampling of single solitons leads to the same results as the DSP heavy NFT, making it obsolete. In comparison, a minimum bandwidth of 55 GHz is needed in the case of the setup using digital multiplexing to reach the HD-FEC.

The required sampling rate is analogous to the required bandwidth. Here, one can see that sampling rates as low as 31 GS/s are sufficient for the linear multiplexing approach, compared to approximately 133 GS/s for the Darboux transform.

To compare the stability against noise-induced perturbations, noise loading at the receiver was changed. Again, the linear multiplexing scheme performs better, reaching the HD-FEC limit at 5 dB for the sampling receiver and 7 dB for the single eigenvalue NFT receiver. The multi-eigenvalue receiver reaches the HD-FEC limit after increasing the OSNR to 10 dB.

To evaluate the needed effective number of bits instead of using a bit error rate (BER) as quality criterion, the mean squared error (MSE) between the received pulse-shapes and the transmitted ones was computed. This was done, because a correlation receiver does not take into account, if the generated symbol is really consisting of multiple solitons. In the simulations, all stochastic imperfections such as noise and laser linewidths were turned off. The criterion for a succesful generation of a higher-order soliton was the resulting pulse shape after transmission, where the signal should consist of split solitons due to de-merging. Here, the bandwidths were set to 19 GHz for the parallel transmitters and 65 GHz for the multi-soliton transmitter. For the parallel transmitters the sampling rates of Tx and Rx were

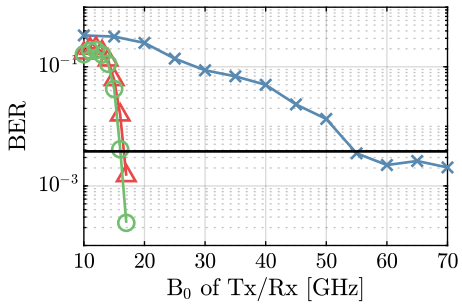

(a) BER depending on bandwidth of Tx and Rx.

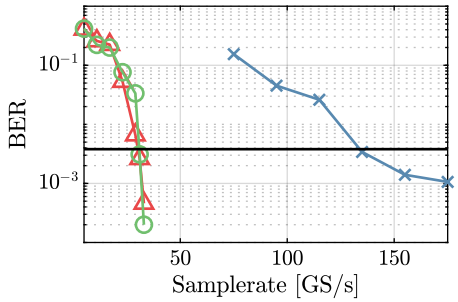

(b) BER depending on sampling rate of Tx and Rx.

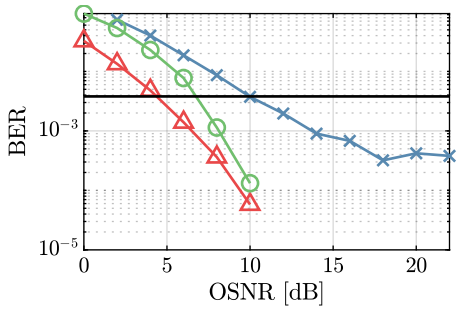

(c) BER depending on Bandwidth.

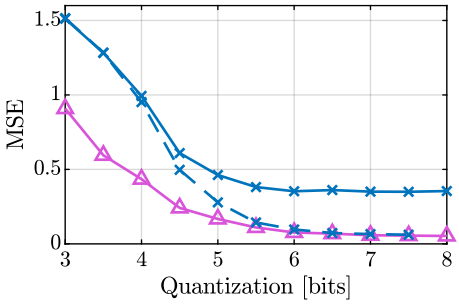

(d) MSE depending on Quantization

Figure 4.13: (a)-(c)BER depending on different hardware parameters for multiple coupling and detection methods. Direct creation of a 5th-order soliton using the Darboux transformation and correlation (blue, x). Parallel creation of first order solitons using parallel transmitters and subsequent coupling inside a fiber with direct sampling of soliton peaks after division (red, triangle) and NFT eigenvalue phase detection (green, circle). HD-FEC limit (black, no marks). (d) MSE of received absolute envelope (normalized to a mean of 1) after transmission depending on quantization of Tx and Rx with a single Darboux transmitter using 91 GS/s (blue, x), with a single Darboux transmitter using 170 GS/s (blue, x, dashed), and parallel transmitters using 91 GS/s (magenta triangle) [93].

Table 4.2: Resulting Hardware Requirements from [93]

Parameters	Parallel Transmitters	Darboux Transformation
Bandwidth	17 GHz	55 GHz
Sampling Rate	33 GS/s	133 GS/s
DAC/ADC Resolution	5.5 bit	7.5 bit
Tx Linewidth	30 kHz	1 kHz
OSNR	4 dB / 6.8 dB	10 dB

set to 91 GS/s. For the multi-soliton transmitter, two sampling rates were examined: 91 GS/s and 170 GS/s. It can be seen in Fig. 4.13d that, if a parallel transmitter is assumed, resolutions between 6 and 7 bits lead to almost perfect solitons. A comparable MSE for the multi-eigenvalue transmitter can also be reached with 6-7 bits of resolution, if 170 GS/s are assumed. However, for lower resolutions, the transmitters' MSE is about 50% higher than the MSE of the parallel transmitter and comparable to a multi-eigenvalue transmitter using only 91 GS/s.

To conclude, the reduction of hardware requirements simulated in [93] is summarised in Table 4.2.

Chapter 5

System Impairments & Equalisation

Practical optical transmission systems suffer from multiple distortions, which are distributed between the transmitter, the channel and the receiver. Many impairments are well studied in linear transmission systems and can be pre-distorted or compensated by DSPs at the receiver. If e.g. the highest frequencies of the transmitted signals are attenuated by low-pass characteristics, using a pre-compensation, the outer flanks of the signal spectrum can be boosted. On the other hand, IQ-imbalances (deviations of the quadrature phase between I- and Q-parts and mismatches of the amplitudes of the real and imaginary parts of the signal) due to imperfect biasing of transmitter MZMs, which lead to non quadratic constellations can be equalized at the receiver, if a linear channel is assumed. Similarly distortions due to nonlinear behaviour of electrical amplifiers and MZMs (see Eq.(2.22)) do not necessarily lead to an error propagation during transmission. Inside the channel, the impact of attenuation and lumped amplification leads to the added white Gaussian noise by the EDFAs.

Unfortunately, due to the nonlinear behaviour of the NFT, the mentioned distortions lead to non-trivial effects onto the modulated NFT coefficients and eigenvalues. For example, IQ-imbalances at the transmitter can result in amplitude mismatches, which due to the nonlinearity lead to changing eigenvalue positions. These changes in turn lead to different propagation properties and error propagations.

Inside the channel, lumped amplification can lead to broadening and contracting of solitons. The broadening in combination with very narrow transmission windows relative to the soliton width can lead to nonlinear interactions between solitons during transmission. This has to be considered when designing the system and power profile during transmission. This is in combination with soliton collisions in WDM systems as described in Section 2.1.5. This can be explained mathematically by the fact that the NFT is based on the integrability of the lossless and noiseless NLSE. However, this does not apply to a real link with lumped amplification, due to the nonuniform loss and gain evolution [95].

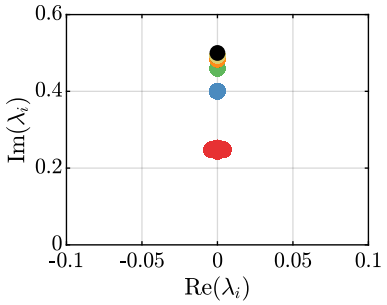

(a) Computed discrete eigenvalues.

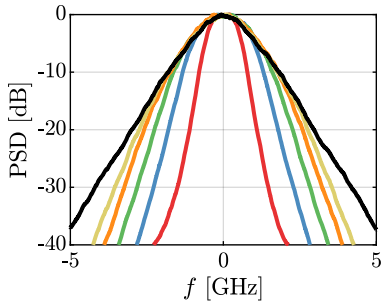

(b) Linear Fourier domain spectrum.

Figure 5.1: Computed eigenvalues and linear spectra of first order solitons after filtering with a 3$^{\text{rd}}$-order Butterworth filter. The filters' 3 dB bandwidth was set to be (red) 20 %, (blue) 40 %, (green) 60 %, (orange) 80 % and (yellow) 100 % of the 20 dB bandwidth of the soliton, which contains 99% of the power. The black dot/line shows the unfiltered eigenvalue/spectrum. $T_0 = 100$ ps, window width 1 ns.

5.1 Impact of Bandwidth Limitations on the Discrete NFT Spectrum

A limiting factor of almost every transmission system is at some point the bandwidth of the components. To give a brief insight into how bandwidth limitations affect the discrete spectrum, Fig. 5.1 shows the spectra of first order solitons. Here, a 3$^{\text{rd}}$-order Butterworth filter with a bandwidth normalized to the solitons' -20 dB bandwidth of $B_{-20\text{dB}} = 0.606/T_0 \cdot \frac{\text{Im}(\lambda_i)}{0.5}$ has been used. One can see, that very narrow filtering at and below 20% of the 20 dB bandwidth leads not only to lower imaginary parts, but also changes of the real-parts of the eigenvalues. This is because in this case the solitons, after filtering, were too broad in time domain, leading to interference between solitons. Increasing the filters' bandwidths leads to increasing imaginary parts of the eigenvalues. Here, if the bandwidth of the filter reaches around 80% of the -20 dB bandwidth of the soliton, the resulting eigenvalues converge on the transmitted position.

5.2 Impact of Noise on the Discrete NFT Spectrum

The influence of noise on soliton transmissions has been extensively studied since their first discovery in the late 1970s [64][15][96][97] and is still a topic of studies [98][99][100]. To give a small example on the impact of noise onto the NFT spectrum, a simplified channel model with complex additive noise shall be used [88, 90].

If a noisy soliton is transformed into the NFT domain, we get a disturbed eigenvalue $\lambda_{i,N}$ and $q_{d,N}(\lambda_i)$,

where

$$\lambda_{i,N} = \lambda_i + n_{\lambda,i} + \mathrm{j}n_{\lambda,q} \tag{5.1}$$

$$q_{d,N}(\lambda_i) = q_d(\lambda_i) + n_{q,i} + \mathrm{j}n_{q,q}, \tag{5.2}$$

where $n_{\lambda,i}$, $n_{\lambda,q}$, $n_{q,i}$ and $n_{q,q}$ denote real-valued noise without any specific assumptions regarding statistical properties [88, 90].

As described earlier in Eq. (4.3) the time shift t_0 of a soliton $q(t-t_0)$ corresponds to an amplitude scaling of the NFT coefficient. Let $q_{d,N}(\lambda_i, t_0)$ be the received $q_{d,N}$ of a soliton which is shifted by t_0. Furthermore, $n_{q,i}$ and $n_{q,q}$ denote the disturbance on $q_{d,N}(\lambda_i, 0)$. This leads to

$$\begin{aligned} q_{d,N}(\lambda_i, t_0) &= q_{d,N}(\lambda_i, 0)\exp(-\mathrm{j}2\lambda_{i,N}t_0) \\ &= (q_d(\lambda_i, 0) + n_{q,i} + \mathrm{j}n_{q,q}) \times \exp(-\mathrm{j}2(\lambda_i + n_{\lambda,i} + \mathrm{j}n_{\lambda,q})t_0) \\ &= q_d(\lambda_i, t_0)\left(1 + \frac{n_{q,i} + \mathrm{j}n_{q,q}}{q_d(\lambda_i, 0)}\right) \times \exp(-\mathrm{j}2n_{\lambda,i}t_0)\exp(2n_{\lambda,q}t_0), \end{aligned} \tag{5.3}$$

which shows that $q_d(\lambda_i, t_0)$ suffers from phase and amplitude noise of the eigenvalue, depending on the time-shift t_0 [88].

5.2.1 b-Modulation

Since the $a(\lambda_i)$ coefficient of discrete eigenvalues is independent of the phase and time-shift of the associated soliton [81][101], also $a'(\lambda_i)$ is independent of the phase and time-shift. Hence, information about theese modulated degrees of freedom of a soliton can fully be recovered from $b(\lambda_i)$. This can improve the detection performance, since the error from impaired $a'(\lambda_i)$ does not matter.

To exemplify this, an idealized transmission was simulated, where as distortions only distributed ASE noise and attenuation with lumped amplification were considered. A train of solitons modulated by a 4ASK-4PSK constellation was transmitted over 200 spans of 50 km NZDSF. After each span, an EDFA (noise figure of 5 dB) was used to compensate for the fiber loss. The results can be seen in Fig. 5.2. Here, one can see an increased amplitude noise for the q_d constellation. This is due to the impact of the amplitude noise of a', as depicted in Fig. 5.2b.

Due to the improved performance of b-modulation, from here on onwards only this modulation type is considered.

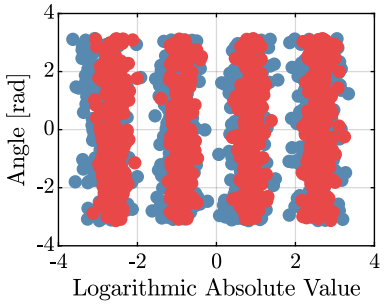

(a) Received constellations for (blue) q_d-modulation, (red) b-modulation.

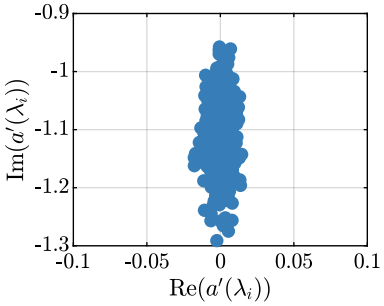

(b) Received $a'(\lambda_i)$.

Figure 5.2: Received $b(\lambda_i)$ and $q_d(\lambda_i)$ constellations after 10,000 km transmission, using 50 km spans of NZDSF with lumped amplification (NF=5dB).

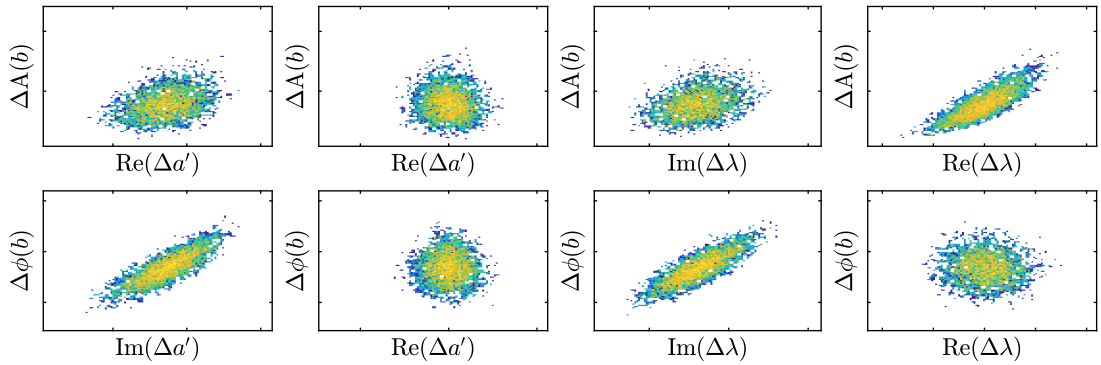

Figure 5.3: Correlations between deviations of the NFT coefficient $b(\lambda_i)$ and $a'(\lambda_i)$ or λ_i.

Table 5.1: Empirical Pearson correlations after 180 spans of 50 km NZDSF from [87]

	$\mathrm{Im}(\Delta a')$	$\mathrm{Re}(\Delta a')$	$\mathrm{Im}(\Delta\lambda)$	$\mathrm{Re}(\Delta\lambda)$
$\Delta\mathrm{A}(b(\lambda_i))$	0.34	-0.04	0.35	0.82
$\Delta\phi(b(\lambda_i))$	0.83	-0.01	0.83	-0.06

5.2.2 Correlations

As already mentioned in the introduction to this chapter, the NFT is tailored to a system without any disturbances such as loss or noise. In disturbed systems however, the eigenvalues differ from their transmitted value. This can partly be deterministic due to e.g. low-pass characteristics (an eigenvalue with lower imginary value has a lower bandwidth), or stochastic due to noise. The deviations of the eigenvalues lead to altered transmission properties of the NFT coefficients through the fiber. This leads to correlations of the eigenvalue deviations and the deviations of the coefficients. In addition, the loss of diagonalisability can lead to correlations between discrete eigenvalues and coefficients of different eigenvalues.

Again, to exemplify this, a simulation was conducted [87]. This time, 15,000 ideally created, QPSK modulated solitons affected by distributed Gaussian noise and attenuation (180 spans with a length of 50 km, EDFA NF=5 dB) were transmitted. The deviations of $b(\lambda_i)$ versus the deviations of λ_i and $a'(\lambda_i)$ are depicted in Fig. 5.3. Here the amplitude deviation

$$\Delta\mathrm{A}(b(\lambda_i)) = \mathrm{A}(b_N(\lambda_{i,N})) - \mathrm{A}(b(\lambda_i)), \tag{5.4}$$

where A is the amplitude and the subscript N stands for a received, distorted value and the phase deviation

$$\Delta\phi(b(\lambda_i)) = \phi(b_N(\lambda_{i,N})) - \phi(b(\lambda_i)), \tag{5.5}$$

where ϕ stands for the phase are depicted in the top and bottom row, respectively. The empirical Pearson correlation coefficients $\rho_{\vec{x},\vec{y}}$ computed by

$$\rho_{\mathbf{x},\mathbf{y}} = \mathrm{cov}(\mathbf{x},\mathbf{y})/(\sigma_{\mathbf{x}}\sigma_{\mathbf{y}}) \tag{5.6}$$

are summarized in Tab. 5.1.

Reasons for these correlations are manyfold and lie within the physical properties of the channel and calculations of the NFT. For example, a deviation of the real part of λ_i leads to a frequency offset and consequently a change in the propagation speed. After a sufficient transmission distance, this leads to an offset of the soliton inside the time window and consequently a change in the absolute value of $b(\lambda_i)$. Similarly, a change in the imaginary part of lambda leads to a change in the peak power of the soliton.

This in turn leads to a change in the strength of the nonlinear Kerr effect and SPM and accordingly an influence on the phase deviation of $b(\lambda_i)$.
The rather small but not negligible correlation between the imaginary part of lambda and the absolute value of b is mainly due to the influence of the calculation of the absolute value $|b(\lambda_i)|= \exp(2 \cdot t_0 \cdot \mathrm{Im}(\lambda_i))$ (as already seen in Eq. (4.3)).
Other works [54][102] additionally show correlations between discrete eigenvalues and the continuous spectrum [54] and furthermore between polarizations [102].

5.3 Equalizers

Due to the non-linearity of the NFT, many already very sophisticated equalizer concepts cannot be transferred directly. In order to be able to use the NFT efficiently, it is therefore necessary to develop new or adapted equalizers. A new way to equalize the discrete spectrum are the correlations mentioned above. If it is assumed that the transmitted eigenvalues are known, the deviations of the modulated NFT coefficient can be inferred with the help of the known deviation of the eigenvalues.
In the long run, it will be optimal to determine an analytical joint probability distribution for this [81]. However, equalizers using, for example, the minimum mean squared error (MMSE) criterion can also be trained to improve transmission performance [81]. These can be linear or non-linear [90] and will be explained later in this chapter. Another possibility for equalization are neural networks [102, 87, 89]. In this work feed forward neural networks are being trained, which can approximate nonlinear mappings as will be explained later.

5.3.1 Linear MMSE Equalizer

Calculation of the MMSE Coefficients

The MMSE criterion can be calculated as [103]

$$F_{\mathrm{MSE}} = \mathrm{E}\left\{|d(i) - y(i)|^2\right\} \Rightarrow \min_{e}, \tag{5.7}$$

where $y(i) = \mathbf{x}^T\mathbf{e}$ and $y^*(i) = \mathbf{e}^H\mathbf{x}^*$. Here, d, y and $\mathbf{x}$ are random processes and $\mathbf{e}$ is the vector of the equalizer coefficients. Using these expressions we get

$$\begin{aligned} F_{\text{MSE}} &= \mathrm{E}\left\{|d(i) - y(i)|^2\right\} \\ &= \mathrm{E}\left\{[y^*(i) - d^*(i)][y(i) - d(i)]\right\} \\ &= \mathrm{E}\left\{[\mathbf{e}^H\mathbf{x}^* - d^*(i)][\mathbf{x}^T\mathbf{e} - d(i)]\right\} \\ &= \mathrm{E}\left\{\mathbf{e}^H\mathbf{x}^*\mathbf{x}^T\mathbf{e} - \mathbf{e}^H\mathbf{x}^*d(i) - d^*(i)\mathbf{x}^T\mathbf{e} + d^*(i)d(i)\right\} \\ &= \mathbf{e}^H\mathrm{E}\left\{\mathbf{x}^*\mathbf{x}^T\right\}\mathbf{e} - \mathbf{e}^H\mathrm{E}\left\{\mathbf{x}^*d(i)\right\} - \mathrm{E}\left\{d^*(i)\mathbf{x}^T\right\}\mathbf{e} + \mathrm{E}\left\{d^*(i)d(i)\right\}, \end{aligned} \tag{5.8}$$

which shall be minimized using the equalizer coefficients $\mathbf{e}$. Since this is a stationary process, the term $\mathrm{E}\left\{\mathbf{x}^*\mathbf{x}^T\right\}$ is the auto-correlation matrix

$$\mathrm{E}\left\{\mathbf{x}^*\mathbf{x}^T\right\} = \mathbf{R}_{xx} \tag{5.9}$$

and $\mathrm{E}\left\{\mathbf{x}^*d(i)\right\}$ is the cross-correlation vector

$$\mathrm{E}\left\{\mathbf{x}^*d(i)\right\} = \mathbf{r}_{xd}. \tag{5.10}$$

If $d(i)$ is assumed to be zero mean,

$$\mathrm{E}\left\{d^*(i)d(i)\right\} = \mathrm{E}\left\{|d(i)|^2\right\} = p^2 \tag{5.11}$$

is the mean power of the training sequence. This leads to the simplification of Eq. (5.8) to

$$F_{\text{MSE}} = \mathbf{e}^H\mathbf{R}_{xx}\mathbf{e} - \mathbf{e}^H\mathbf{r}_{xd} - \mathbf{r}_{XD}^H\mathbf{e} + p^2, \tag{5.12}$$

which can be brought to the form [103]

$$F_{\text{MSE}} = (\mathbf{e}^H\mathbf{R}_{xx} - \mathbf{r}_{xd}^H)\mathbf{R}_{xx}^{-1}(\mathbf{R}_{xx}\mathbf{e} - \mathbf{r}_{xd}) - \mathbf{r}_{xd}^H\mathbf{R}_{xx}^{-1}\mathbf{r}_{xd} + p^2, \tag{5.13}$$

which is minimized if for example

$$\mathbf{R}_{xx}\mathbf{e} - \mathbf{r}_{xd} = 0 \tag{5.14}$$

leading to the calculation of the coefficients according to

$$\mathbf{e} = \mathbf{R}_{xx}^{-1} \cdot \mathbf{r}_{xd}. \tag{5.15}$$

Application to the NFT

For the application in equalization of the discrete NFT spectrum, the mentioned correlations between $\Delta\lambda_i$ or $\Delta a'(\lambda_i)$ and $\Delta b(\lambda_i)$ are to be used. Since only the b-coefficient is being modulated, $a'(\lambda_i)$ is fixed and its' deviations can be used to improve the equalization performance. Since deviations of λ_i and $a'(\lambda_i)$ have a different impact on the phase and amplitude of b, two real valued equalizers are designed for each [81].
The vector $\mathbf{x}$ in this use case writes as the real-valued vector

$$\mathbf{x}_n = [\mathrm{Re}(\Delta a'_n),\, \mathrm{Im}(\Delta a'_n),\, \mathrm{Re}(\Delta\lambda_{i,n}),\, \mathrm{Im}(\Delta\lambda_{i,n})] \tag{5.16}$$

where n is the soliton index and

$$d_{n,\mathrm{A}} = \Delta A(b_n(\lambda_i)) \qquad \text{or} \qquad d_{n,\phi} = \Delta\phi(b_n(\lambda_i)), \tag{5.17}$$

for amplitude and phase equalization respectively. The cross-corelation vector $\mathbf{r}_{xd}$ can then be computed using N_t training solitons according to

$$\mathbf{r}_{xd} = \frac{1}{N_t}\sum_{n=1}^{N_t} \mathbf{x} d_n. \tag{5.18}$$

The auto-correlation matrix $\mathbf{R}_{xx}$ is computed accordingly:

$$\mathbf{R}_{xx} = \frac{1}{N_t}\sum_{n=1}^{N_t} \mathbf{x}_n \mathbf{x}_n^T. \tag{5.19}$$

Now, the coefficients $\mathbf{e}_A$ and $\mathbf{e}_\phi$ can be calculated according to 5.15. Finally, the estimated deviations of any $b_n(\lambda_i)$, which is not part of the training sequence read

$$\Delta\hat{A}(b_n(\lambda_i)) = \mathbf{x}_n \mathbf{e}_A \qquad \text{and} \qquad \Delta\hat{\phi}(b_n(\lambda_i)) = \mathbf{x}_n \mathbf{e}_\phi. \tag{5.20}$$

Since this equalizer is purely linear, an improvement of the equalization of the nonlinearly scaling amplitude can be gained, if the amplitude of $b_n(\lambda_i)$ is scaled logarithmically before calculating the coefficients.
To expand this equalizer to higher order solitons, the vector $\mathbf{x}$ can be extended by deviations of the remaining eigenvalues of the soliton or different soliton channels [104].

5.3.2 Nonlinear MMSE Equalizer

MMSE equalizers are a widely used tool also in conventional fiber optic communications. For example, with the help of a digital feed forward equalizer it is possible to minimise intersymbol interference caused by dispersion according to

$$z[k] = \sum_{n=0}^{N_e-1} e[n]y[k-n],$$

where N_e is the number of coefficients, adjusted to the accumulated dispersion of the system, and z and y are the respective filter outputs and inputs. The idea behind Volterra filters is to represent the non-linear phase rotation by the Kerr effect $\exp(-\mathrm{j}\gamma L_{\mathrm{eff}}|A(t)|^2)$ as a Taylor series $\sum_{n=0}^{\infty} \frac{1}{n!}\left(-\mathrm{j}\gamma L_{\mathrm{eff}}|A(t)|^2\right)^n$ [105][106]. It has been shown that for a compensation of the nonlinear Kerr effects, kernels up to $n = 1$ are sufficient in power regimes up to $P = 10\,\mathrm{dBm}$ to describe the signal propagation.
This in combination with the linear feed forward equalizer (FFE) leads to the nonlinear Volterra equalizer in time-domain:

$$z_{\mathrm{NLVE}}[k] = \sum_{n=0}^{N_e-1} e_1[n]y[k-n] + \sum_{l=0}^{N_e-1}\sum_{m=0}^{N_e-1}\sum_{n=0}^{N_e-1} e_3[l,m,n]\cdot y[k-l]\cdot y[k-m]\cdot y^*[k-n], \tag{5.21}$$

which not only considers linear interference, but also nonlinear interference between symbols.
The idea of nonlinear equalization shall now be expanded on the NFT domain linear MMSE equalizer to combat nonlinear dependencies of $b(\lambda_i)$ and λ_i in e.g. the computation of the amplitude (4.3) or the spatial evolution (3.37). To start, the deviation vector $\mathbf{x}$ gets expanded by the amplitude and the phase of the received $b(\lambda_i)$:

$$\mathbf{x}_{\mathrm{A}} = [|b(\lambda_i)|,\, \mathrm{Re}(\Delta a_n'),\, \mathrm{Im}(\Delta a_n'),\, \mathrm{Re}(\Delta\lambda_{i,n}),\, \mathrm{Im}(\Delta\lambda_{i,n})], \tag{5.22}$$

$$\mathbf{x}_{\phi} = [\angle b(\lambda_i),\, \mathrm{Re}(\Delta a_n'),\, \mathrm{Im}(\Delta a_n'),\, \mathrm{Re}(\Delta\lambda_{i,n}),\, \mathrm{Im}(\Delta\lambda_{i,n})]. \tag{5.23}$$

These vectors then get expanded according to Fig. 5.4. The resulting $\mathbf{x}_{\mathrm{A,NL}}$ can then be used in combination with Eqs. (5.18), (5.19) and (5.15) to calculate $\mathbf{e}_{\mathrm{A},1\ldots O_{\mathrm{NL}}}$, where O_{NL} is the order of

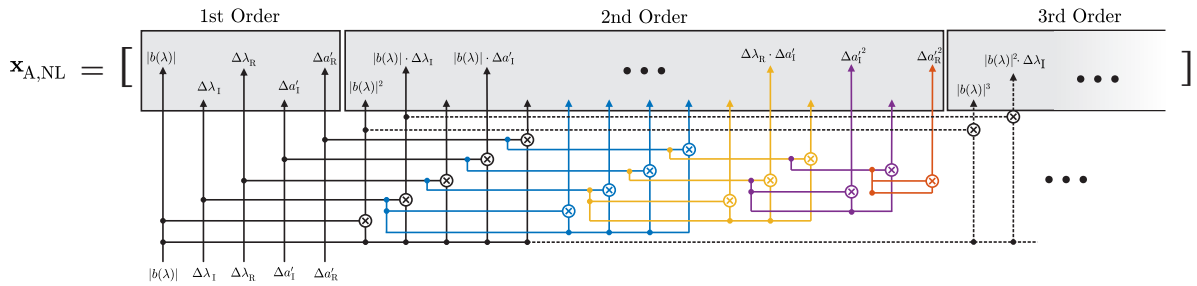

Figure 5.4: Schematic depiction of $\mathbf{x}_{\mathrm{A,NL}}$ with nonlinearities of third order. Mind that for $\mathbf{n}_{\phi,\mathrm{NL}}$ $|b(\lambda)|$ is replaced by the phase $\angle b(\lambda)$ of b. The first order stands for the initialization vector from Eq. (5.22). The second order is color coded to show the second order mixing terms of $\mathbf{x}_{\mathrm{A}}$ and $|b(\lambda)|$ (black), $\Delta\lambda_i$ (blue), $\Delta\lambda_R$ (yellow), $\Delta a'_I$ (purple) and $\Delta a'_R$ (orange), respectively. Additionally the first parts of third order nonlinearity mixing terms are shown (dashed lines). [90]

nonlinearity to be used. A third order nonlinear NFT equalizer for a single order soliton then reads

$$\begin{aligned}\Delta\hat{A}(b_n(\lambda_i)) = &\sum_{l=1}^{N_x} \mathbf{e}_{A,1}[l]\mathbf{x}_{\mathrm{A}}[l] \\ &+ \sum_{l=1}^{N_x}\sum_{m=1}^{N_x} \mathbf{e}_{A,2}[l,m]\cdot\mathbf{x}_{\mathrm{A}}[l]\cdot\mathbf{x}_{\mathrm{A}}[m] \\ &+ \sum_{l=1}^{N_x}\sum_{m=1}^{N_x}\sum_{n=1}^{N_x} \mathbf{e}_{A,3}[l,m,n]\cdot\mathbf{x}_{\mathrm{A}}[l]\cdot\mathbf{x}_{\mathrm{A}}[m]\cdot\mathbf{x}_{\mathrm{A}}[n].\end{aligned} \tag{5.24}$$

A major disadvantage of time domain Volterra equalizers is the large number of coefficients that need to be calculated. In long transmission links, the nonlinear symbol interference can extend over several symbols and thus require large N_e.

Since in soliton transmission there is usually no interference, N_x is limited to the length of $\mathbf{x}_{\mathrm{A}}$ (which is only five in the case of single eigenvalue equalization). The total amount of coefficients to be trained and added multiplications in the online equalization process is then

$$N_{\mathrm{coeffs}}(O_{\mathrm{NL}}) = \sum_{m=1}^{O_{\mathrm{NL}}} \frac{1}{m!} \prod_{n=0}^{m-1} (N_x + n). \tag{5.25}$$

5.3.3 Neural Networks

Machine learning (ML) has also gained a foothold in optical communication. For example, it is being investigated in the physical layer for estimating the quality of transmission (QoT) [107], mitigating non-linearities [108] or generalized parameter optimization in WDM networks [109]. Additionally, ML can also be used in the network layer for e.g. traffic prediction [110]. Comprehensive reviews on ML in

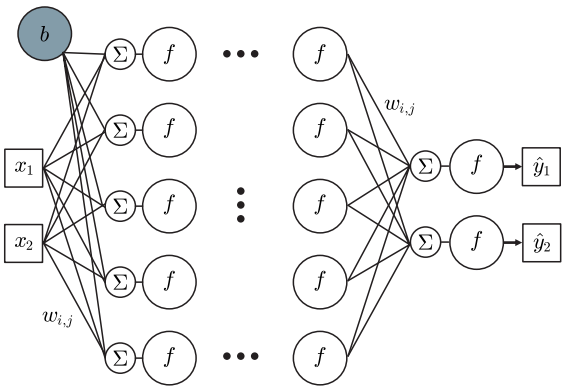

Figure 5.5: Exemplary structure of a neural network. Two inputs $x_{1,2}$ get mapped to two outputs $\hat{y}_{1,2}$ using an arbitrary number of layers and nodes. Each layer consists of nodes which contain activation functions of weighted sums of the preceding layers' nodes.

optical communications engineering can be found in [111][112]. In ML, knowledge is extracted from existing (known) and target-related data using mathematics and computer science to solve a given problem. Patterns are to be recognised on the basis of the data obtained in order to find a generalized model that also works with unknown input data. This is done through parameterised training of the model. A generalized model has the ability to describe or classify unseen (new) data as correctly as possible. This process is called prediction [113][114].

Neural networks, as a subcategory of machine learning, consist of various input, hidden and output layers, which in turn always contain at least one neuron (see Fig. 5.5). The input and output layers are essential and are responsible for the input of data and the output of the prediction, respectively. The hidden layers are optional, but are needed to solve non-linear problems. Among other things, they determine the complexity of the network. More than one hidden layer makes the neural network a deep neural network (DNN). The neurons, also called nodes of the network, are stimulated with so-called activation functions, which are selected specifically for the problem. These are differentiable functions that can be used to map to ranges of values or specific values, which make it possible to learn non-linear problems. The parameters (e.g. the number of hidden layers or the choice of the activation functions) or variables that have to be set by the user of the model are called hyper-parameters.

Backpropagation

The algorithmic approach that neural networks use in training is called backpropagation. It is based on the iterative application of the chain rule for the derivation of the partial derivatives of the loss function

$$L(y, \hat{y}) \tag{5.26}$$

with respect to all weights of the network, where y is the known output and $\hat{y}$ is the prediction, which describes a differentiable and continuous function of the weights between the input values x of the network and the neurons. The output of a neuron is given by

$$o_j = f(N_j) \tag{5.27}$$

with

$$N_j = \sum_{i=1}^{N} w_{ij} \cdot x_i + b_j. \tag{5.28}$$

Here, f is a differentiable activation function, w_{ij} the weight from input i to neuron j, x_i the inputs and b_j a neuron specific bias. The goal is now to compute the partial derivation of the loss function E with regards to $w_{i,j}$ by using the chain rule

$$\frac{\partial L}{\partial w_{i,j}} = \frac{\partial E}{\partial o_j} \frac{\partial o_j}{\partial N_j} \frac{\partial N_j}{\partial w_{i,j}}. \tag{5.29}$$

This leads to a change of weights $\Delta w_{i,j}$ using the gradient descent

$$\Delta w_{i,j} = -\eta \frac{\partial L}{\partial w_{i,j}}, \tag{5.30}$$

where η is the learning rate. This gets repeated for all training samples and a finite number of training epochs.

Neural Network Parameters

The structure of a neural network (NN) is parametrized by its' hyper parameters such as the number of inputs, outputs, hidden layers and nodes of each layer or the activation functions and other things such as the normalization of the data. All of these hyper parameters are use-case specific and have to be optimized before employing the neural network. For example, it is possible for a model to have a low error on the training set but significantly weaker results on the test set. This phenomenon is called *over-fitting* and occurs when the model is too complex for the data set. The opposite of over-fitting is *under-fitting*. The model is not complex enough for the the data set at hand and does not achieve a low

training error.

Another important set of parameters are the training parameters. These contain among others the number of training symbols, the number of training epochs (e.g. the number of forward and backward propagations during training), the training batch size, the so-called *drop-out* and the learning rate η. *Minibatching* is a tool to increase the performance and speed of the training process by bundling multiple training samples into one batch. The weights $w_{i,j}$ are then not updated for each training sample, but by an averaged gradient calculated from all samples of the batch.

Drop-out describes a regularisation method during training that randomly sets individual inputs of a neuron to zero, thus deactivating them. The technique is used to avoid over-fitting during the training process, by deactivating individual pieces of information, including the data less likely to influence the NN, which are responsible for memorisation in the training. This is exactly where the task lies in the choice of the drop-out rate. If the chosen drop-out rate is too low, the test result will not improve. If, on the other hand, the dropout rate is too high, the network lacks much of the data it needs to learn properly, which leads to poor model performance.

Neural Network NFT Equalizer

The neural network equalizers used in this work uses the tools of neural networks and applies them to the NFT outputs. The input vector of the NNs can be

$$\begin{aligned}\mathbf{x}_{\mathrm{NN}} &= [\mathrm{Re}(b(\lambda_i)),\, \mathrm{Im}(|b(\lambda_i)|),\, \mathrm{Re}(\Delta a_n'),\, \mathrm{Im}(\Delta a_n'),\, \mathrm{Re}(\Delta\lambda_{i,n}),\, \mathrm{Im}(\Delta\lambda_{i,n})] \\ &\quad \text{or} \\ \mathbf{x}_{\mathrm{NN}} &= [\angle b(\lambda_i),\, \log(|b(\lambda_i)|),\, \mathrm{Re}(\Delta a_n'),\, \mathrm{Im}(\Delta a_n'),\, \mathrm{Re}(\Delta\lambda_{i,n}),\, \mathrm{Im}(\Delta\lambda_{i,n})],\end{aligned} \tag{5.31}$$

which are mapped to a chosen type of outputs. The outputs can be an equalized $\hat{b}(\lambda_i)$ [87], which has to be classified by demodulation, or already classified bits. This way the NN also takes over the task of classification. Another output is the so-called *softmax*

$$\hat{y}_j = \frac{\exp(N_j)}{\sum_{m=1}^{M} \exp(N_m)}, \tag{5.32}$$

where M is the amount of outputs. This leads to values between zero and one at the output, where the highest $\hat{y}_j$ refers to the predicted transmitted symbol. This way, the output is also a measure of confidence and could be used for further soft decisions error correction. The NN adapted to an NFT equalization using one eigenvalue is depicted in Fig. 5.6. Again, $\mathbf{x}_{\mathrm{NN}}$ can be expanded by additional eigenvalues.

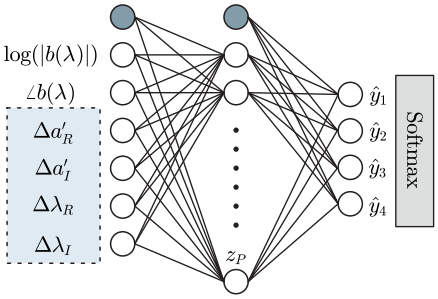

Figure 5.6: Neural network adapted to an NFT equalization using one eigenvalue and softmax decision. Subscript R and I denote real- and imaginary part, respectively.

5.4 Experimental Performance Comparison

In order to compare the equalizer concepts explained above, they were applied to experimental data, measured at Helmut Schmidt University, Hamburg. The experiments were first order soliton transmissions on one polarization and second order transmissions on two polarizations. In this section first the data-generation and experimental setup are described. Afterwards, the resulting data is investigated with regard to the correlations between the deviations of NFT coefficients and eigenvalues. Finally, the equalizer concepts shall be investigated and compared to draw a conclusion with regards to performance and complexity differences.

Mind, that in the case of dual-polarization transmission the NFT has to be expanded to two polarizations. For this purpose, instead of a scalar $q(t,z)$, the vector $\mathbf{q}(t,z)$ is used, which describes the time domain signal on both polarizations. This can be inserted in the normalised nonlinear Schrödinger equation, which produces the coupled Manakov equation. The Zakharov-Shabat system then extends to

$$\frac{\partial}{\partial t}\boldsymbol{v} = \Lambda \boldsymbol{v} \tag{5.33}$$

$$\boldsymbol{v} = \begin{pmatrix} v_1(\lambda;t,z) \\ v_2(\lambda;t,z) \\ v_3(\lambda;t,z) \end{pmatrix}, \boldsymbol{\Lambda} = \begin{pmatrix} -\mathrm{j}\lambda & q_1(t,z) & q_2(t,z) \\ q_1^*(t,z) & \mathrm{j}\lambda & 0 \\ q_2^*(t,z) & 0 & \mathrm{j}\lambda \end{pmatrix}.$$

Again, using the vanishing boundary condition, we can start the iteration with

$$\boldsymbol{v} \to \begin{pmatrix} 1 \\ 0 \\ 0 \end{pmatrix} e^{-\mathrm{j}\lambda t} \quad \text{for} \quad t \to -\infty \tag{5.34}$$

Table 5.2: Parameters of the experimental setup.

DAC sampling rate	88 GSa/s
ADC sampling rate	80 GSa/s or 40 GSa/s
Baud rate	1 GBd or 2 GBd
Carrier laser wavelength λ_c	1550.12 nm
Carrier laser linewidth $\Delta\nu$	< 1 kHz
Symbol period T_s	1 ns or 0.5 ns
Normalized time $T_0 = T_s/11$	91 ps or 45.45 ps
Span length	50.3 km
Fiber loop length	100.6 km
Effective nonlinearity γ_{eff}	$0.96\,\text{W}^{-1}\text{km}^{-1}$
Fiber attenuation α	0.2 dB/km
Chromatic dispersion β_2	$-5.75\,\text{ps}^2/\text{km}$

Table 5.3: Parameters of the NFT.

	Single-polarization	Dual-polarization
Eigenvalues λ_i	0.5j	$\mp 0.15 + 0.3$j
Modulation format	4ASK-8PSK	QPSK-QPSK
Amplitudes $\lvert b(\lambda_i)\rvert$	exp([−1.5 − 0.5 0.5 1.5])	[0.5 2.5]
LPA Launch power P_{in}	-3.85 dBm	1 GBd: -5 dBm ,2 GBd: 0.92 dBm

to gain the NFCs

$$a(\lambda; z) = \lim_{t\to\infty} v_1 e^{+\text{j}\lambda t} \tag{5.35a}$$

$$b_1(\lambda; z) = \lim_{t\to\infty} v_2 e^{-\text{j}\lambda t} \tag{5.35b}$$

$$b_2(\lambda; z) = \lim_{t\to\infty} v_3 e^{-\text{j}\lambda t}. \tag{5.35c}$$

One can see from the equations, that the NFT couples both polarizations and does not treat them independently, as it is done by conventional polarization division multiplexing. Due to the coupled computation of the polarizations, differential precoding schemes [85] have been proposed.

5.4.1 Experimental Setup

The experimental setup is depicted in Fig. 5.7 and the parameters summarized in Tab. 5.2.
One experiment consisted of a highly modulated single eigenvalue transmission using only one polarization with a symbol rate of 1 GBd and a 4ASK-8PSK modulation scheme. Details of the modulation can be found in Tab. 5.3. To examine a multi eigenvalue double polarization transmission, two eigenvalues

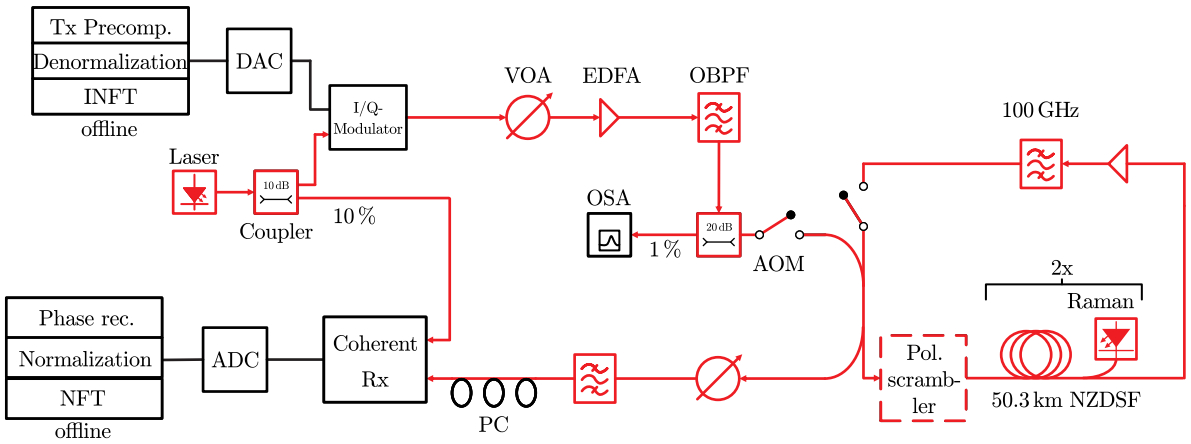

Figure 5.7: Neural network adapted to an NFT equalization using one eigenvalue and softmax decision.

with different real parts where used and differentially modulated on both polarizations. The real parts of the eigenvalues were ± 0.15. Both eigenvalues were modulated using QPSK on both polarizations. Additionally $b_2(\lambda)$ was rotated by $\pi/4$ to optimize the signal in terms of peak-to-average power ratio (PAPR) [86]. Since, due to the different real parts, the solitons travel inside the retarding time-frame, a pre-shift is used to apply a virtual propagation backwards over a certain distance [86]. The soliton signals are created using the Darboux transform and then denormalized into physical units. This was followed by a precompensation of frequency and amplitude responses of the DAC and modulator. Blocks of 2978 or 5957 symbols for 1 or 2 GBd, respectively, were transmitted. At least four symbols are used to synchronize the sequence and, in the DP case, 256 symbols with a reference sequence containing fundamental solitons were used to recover the polarization. The loop consists of two 50.3 km NZDSF spans with counterpropagating Raman amplification and an EDFA for forward amplification. In the case of DP transmission a polarization scrambler was added to the loop. For more detailed explanations of the experimental setup, the reader is referred to publications of the Schäffer group at HSU, Hamburg[86][88].

5.4.2 Experimental Perturbation Correlations

First, the correlations between deviations of the eigenvalues and NFCs, which have already been shown simulatively, will also be shown experimentally.

Single Eigenvalue Transmission

This is first demonstrated by means of the transmission of first-order solitons. The received $b(\lambda)$ after 905 km transmission are depicted in Fig. 5.8a, where the larger spread of amplitudes of the

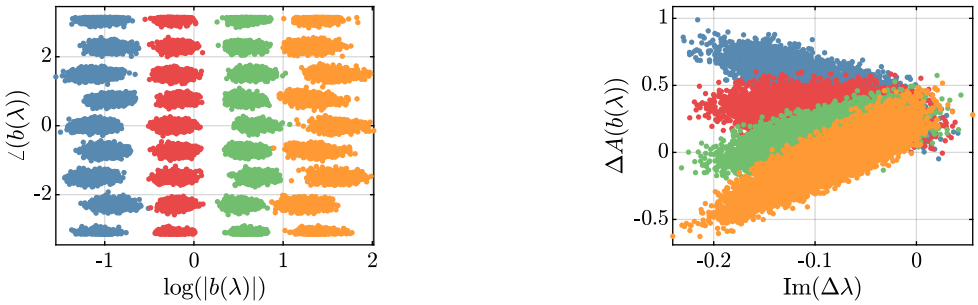

(a) Constellation of received $b(\lambda)$ in polar coordinates.

(b) Deviation of the amplitude of $b(\lambda)$ over the deviation of the eigenvalues' imaginary part (color coded to the transmitted amplitude to show different correlations depending on the transmitted symbol)

Figure 5.8: Received $b(\lambda)$ constellation after 905 km experimental transmission of first order solitons and one polarization and measured correlations [90].

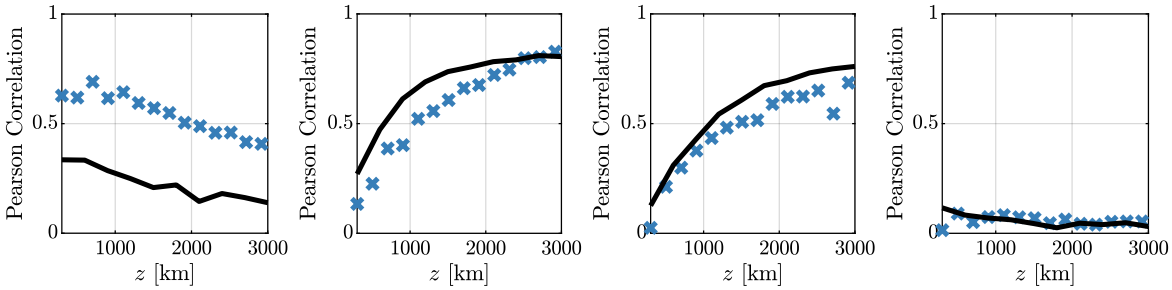

(a) $\rho(\mathrm{Im}(\Delta\lambda), \Delta\mathrm{A}(b(\lambda)))$ (b) $\rho(\mathrm{Im}(\Delta\lambda), \Delta\phi(b(\lambda)))$ (c) $\rho(\mathrm{Re}(\Delta\lambda), \Delta\mathrm{A}(b(\lambda)))$ (d) $\rho(\mathrm{Re}(\Delta\lambda), \Delta\phi(b(\lambda)))$

Figure 5.9: Pearson correlations between $\Delta\lambda$ and $\Delta b(\lambda)$ during transmission. Black lines refer to idealized simulations and blue X to experimental results [90].

highest/lowest amplitudes (leading to the largest absolute time shifts) is qualitatively larger than of the middle amplitudes. This can partly be explained by Eq. (5.3) and is also observable in Fig. 5.8b. Fig. 5.8b also shows the strong correlations between $\mathrm{Im}(\Delta\lambda)$ and $\Delta\mathrm{A}(b(\lambda))$, which have already been observed and explained in Section 5.2.2.

In order to directly compare the experimentally measured correlations with a simulation, an idealised simulation was set up. Here, a first-order soliton was transmitted, which was modulated exactly as in the experiment. However, the transmitters and receivers were assumed to be ideal and only distributed noise with fiber loss was assumed as distortion. The absolute Pearson correlations of experiment and simulation and their development during transmission are depicted in Fig. 5.9. First of all, a deviation between the simulation and the experiment can be observed in Fig. 5.9a. Here the correlation in the simulation is not as strong as in the experiment. This can be explained by transmitter disturbances

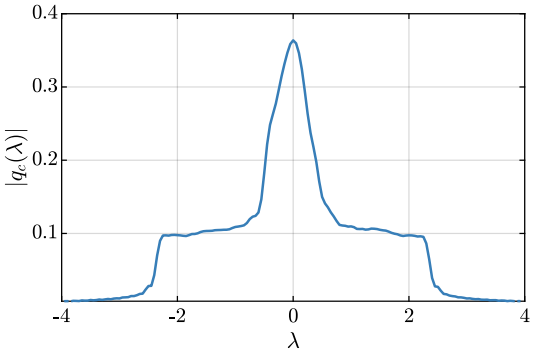

(a) Computed average received $q_c(\lambda)$, which was not modulated at Tx.

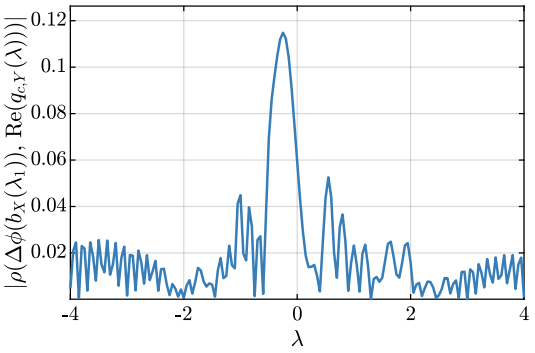

(b) Pearson correlation between the deviation of the phase of $b_X(\lambda_1)$ of the X-polarization and the real-part of the continuous spectrum of the Y-polarization $\mathrm{Re}(q_{c,Y}(\lambda))$.

Figure 5.10: Received unmodulated continuous spectrum after experimental transmission of discrete DP spectrum modulation. The continuous spectrum was set to be 0 at the transmitter. However, energy from the discrete spectrum radiates into the continuous spectrum and leads to correlations.

such as low-pass behaviour (see Fig. 5.1a), which causes the imaginary part of the eigenvalue to drop. This in combination with $|q_d(\lambda_i)|= 2\mathrm{Im}(\lambda_i)\exp(2T_0\mathrm{Im}(\lambda_i))$ leads to decreasing amplitudes of $b(\lambda_i)$, if $a'(\lambda_i)$ does not increase proportionally. Overall, this part of correlation decreases during transmission, since this deviation is not changing the transmission properties of the soliton.

This is in contrast to the correlations depicted in Figs. 5.9b and 5.9c. If the imaginary part of an eigenvalue is changed, this changes the peak power of the soliton. This in turn leads to a change in the non-linear phase rotation caused by SPM. Therefore, the magnitude of this correlation increases with increasing transmission length (see Fig. 5.9b), as it is directly dependent on the transmission characteristics of a soliton.

Similarly, there is a correlation between the real part of the eigenvalue (which represents the center frequency) and the amplitude of $b(\lambda_i)$ (which represents the position of the soliton in the time window). Obviously, the dispersion in the fiber leads to a changing propagation speed with changing center frequency of the soliton. This leads to changing positions in the time window and thus to changing amplitudes of $b(\lambda_i)$. Since this correlation is also a direct result of fiber properties, the strength of the correlation also increases with the transmission distance (see Fig. 5.9c).

In contrast, the correlation between $\mathrm{Re}(\Delta\lambda)$ and $\Delta\phi(b(\lambda))$ is very low to non-existent and can therefore be ignored when designing equalizers.

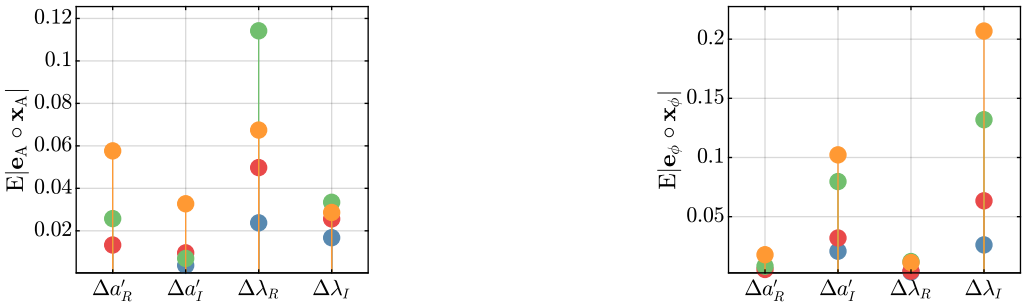

(a) Impact of known deviations on $\mathrm{A}(b(\lambda))$.

(b) Impact of known deviations on $\phi(b(\lambda))$.

Figure 5.11: Average absolute influence of known deviations after using linear MMSE equalization after (blue): 704 km, (red): 1509 km, (green): 2313 km, (orange): 3118 km transmission. Subscripts R and I stand for real- and imaginary value, respectively.

Transmission with two Eigenvalues

To further show correlations between the continuous and the discrete spectrum, even between polarizations, a calculated continuous spectrum and a cross-correlation are shown in Fig. 5.10. Although the continuous spectrum has not been modulated, energy is received here. This is limited between $\lambda = \pm 2.3$, which corresponds to the filter bandwidth. A peak can be detected around $\lambda = 0$. This corresponds to the real part of the eigenvalues at ± 0.15. In Fig. 5.10b, the correlation between the real part of the continuous spectrum and the deviation of the phase of $b_X(\lambda_1)$ can be seen. This is shifted into the negative lambda range, which corresponds to the position of the eigenvalue. To illustrate the magnitude of the cross-correlations, the correlation between different polarizations is shown here. Since $b(\lambda_i)$ of both polarizations are coupled via λ_i, the polarizations are not orthogonal.

5.4.3 Linear and Nonlinear MMSE

Single Order Soliton

First, the equalization behaviour of the linear MMSE equalizer on the transmission with an eigenvalue is to be investigated. For this purpose, Fig. 5.11 shows the averaged results of an element-wise multiplication of the trained equalizer tap weights $\mathbf{e}$ and deviation vector $\mathbf{x}$ (analogous to Eq. (5.20)). Thus, the influence of each known deviation can be quantified. Mind that Fig. 5.11 can be compared to conventional depictions of tap-weights of e.g. FFE filters to compensate for dispersion. However, the depicted taps in Fig. 5.11 are already weighted by the deltas, since they do not have the same average amplitude.

This leads to the normalized equalizer weights of a third order nonlinear equalizer depicted in Fig. 5.12.

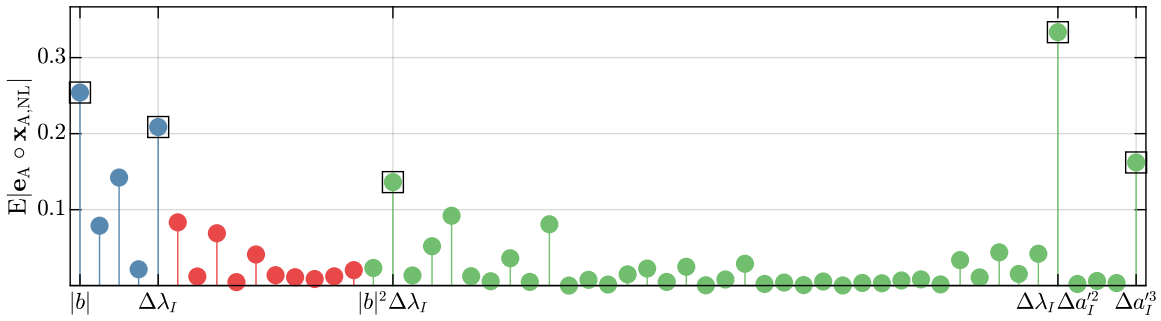

Figure 5.12: Average absolute influence of known deviations after using nonlinear MMSE equalization after 1911 km. (blue) first order taps, (red) second order taps, (green) third order taps. Squared values refer to NFC/deviation combinations as labeled beyond.

Here one can see that the higher order terms can have a high impact onto the equalization performance w.r.t. the amplitude. In addition, one can see that many weights, especially of the high order, are very low. By deleting the weights below a certain limit, the size of the filter can be greatly reduced without big loss of performance.

The number of training symbols required for the different equalizers is shown in Fig. 5.13a. As the complexity of the equalizers increases, so does the number of required training symbols. Thus, approximately 1500 training symbols are sufficient to train the linear MMSE equalizer sufficiently. A non-linear MMSE equalizer of the fifth order, on the other hand, requires 14000 training symbols to be able to set all coefficients properly and is not able to yield satisfactory results with a smaller number of training symbols. Additionally, only minimally better results can be achieved than with a third-order nonlinear equalizer, which is already trained with about 7100 symbols and leads to satisfactory results with only 3100 symbols. Furthermore, the nonlinear equalizer of second order reaches the HD-FEC limit using only 1600 symbols. Therefore, only nonlinear equalizers up to the third order are discussed in the further considerations, since the minimally improved BERs are not worth the training effort and increased the computational cost.

The BER achieved by trained equalizers as a function of the transmission distance is plotted in Fig. 5.13b. The linear MMSE equalizer increases the transmission range at the HD-FEC limit by approximately 200 km to up to 1550 km. The tested non-linear equalizers can still improve this. If the HD-FEC limit is used, second-order equalizers can improve the range by 700 km. This can be improved by third-order non-linear equalization, which extends the transmission range by up to 1350 km.

In order to show these improvements qualitatively, Fig. 5.14 shows constellation diagrams of $b(\lambda_i)$ after 2515 km transmission. These show, among other things, an IQ imbalance depending on the transmitted symbol. This can be a result of amplitude imbalances of the IQ modulators, which lead to different influences of SPM depending on the modulated phase. While the linear MMSE equalizer

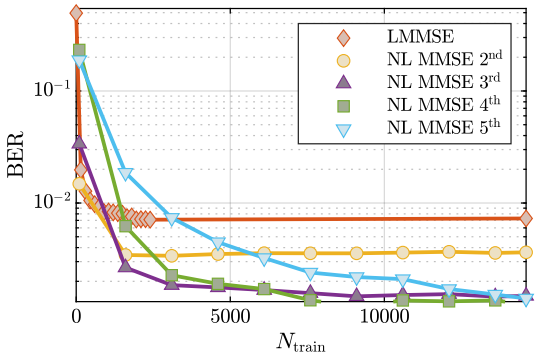

(a) Resulting BER after equalization using linear and nonlinear MMSE equalizers for 1911 km transmission reach depending on the number of training symbols and order of nonlinearity.

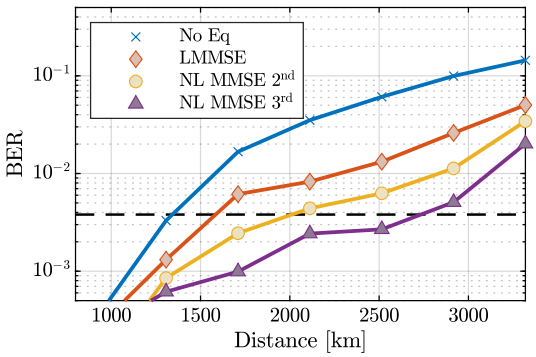

(b) Resulting BER after varying transmission distances for different orders of nonlinearity for the nonlinear MMSE equalizer using 10,000 training symbols. For readability the HD-FEC limit is included (dashed line).

Figure 5.13: Determined BERs of single eigenvalue transmission for different (N-)LMMSE equalizers depending on training symbols and distance.

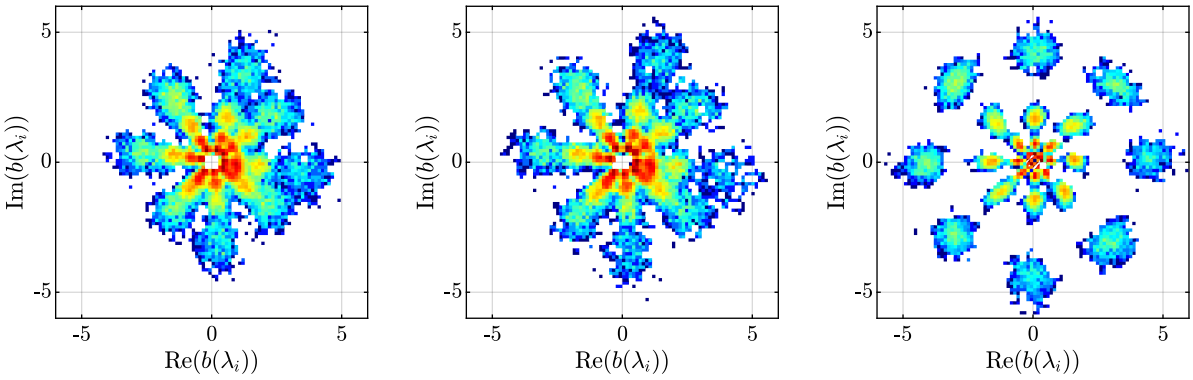

(a) Constellation of received $b(\lambda)$ without equalization.

(b) Constellation of received $b(\lambda)$ with linear MMSE equalization using 2500 training symbols.

(c) Constellation of received $b(\lambda)$ with non-linear MMSE equalization using 6300 training symbols.

Figure 5.14: Received $b(\lambda)$ constellation after 2515 km experimental transmission of first order solitons and one polarization after different equalizers.

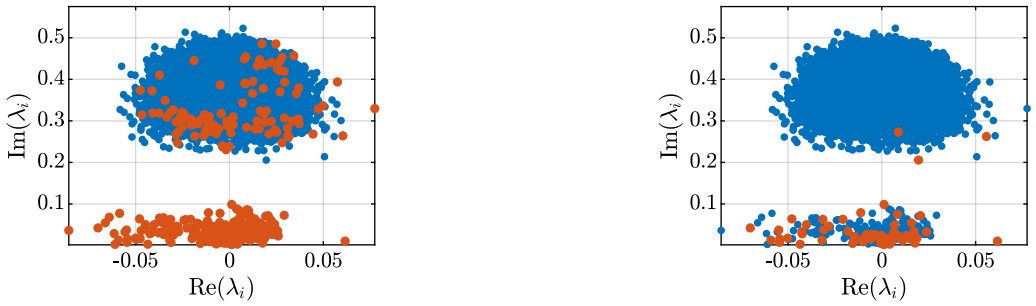

(a) No equalizer

(b) 3rd order nonlinear EQ

Figure 5.15: Received eigenvalues after 1307 km transmission. Orange markups represent eigenvalues, which lead to symbol errors.

cannot compensate this disturbance (Fig. 5.14b), a third-order non-linear equalizer can (Fig. 5.14c). The non-linear equalizer also performs much better in terms of amplitude equalization, so that there are only very few errors due to incorrectly decided amplitude levels.

Fig. 5.15 shows the eigenvalues received after 1307 km transmission range. One can see that a small part of the eigenvalues are strongly shifted to the lower parts of the complex plane. These eigenvalues are spurious eigenvalues that have emerged due to disturbances during transmission. If an eigenvalue is part of the main group of eigenvalues, the non-linear equalizer is able to almost completely equalize the received $b(\lambda_i)$ and thus leads to lower BERs. However, if an erroneous eigenvalue is chosen the equalizer is not able to fully compensate for this error. Furthermore, if the order of non-linearity is high, this leads to error propagation, as $b(\lambda_i)$ may be in a region where a higher bit error penalty occurs after equalization. For this reason, the relative improvement by using higher order equalizers for shorter distances is smaller compared to lower order equalizers.

Dual Polarization Transmission

In this section the dual polarization transmission with two eigenvalues is examined with regard to MMSE equalizers. First, each $b_{1,2}(\lambda_i)$ is equalized individually using the associated λ_i and $a'(\lambda_i)$, leading to four equalizers for this transmission. For good results 2000 training symbols for the LMMSE and 8000 training symbols for the 3rd order non-linear equalizer have been used in this section. The resulting BERs for the two equalizers and symbol rates are depicted in Fig. 5.16. Both equalizers can improve the transmission distances. Nonlinear equalization deteriorates the results for relatively short transmission distances compared to the linear counterpart and only shows small improvements for longer transmissions especially for the 1 GBd case, however. The reason for worse performance at lower distances can again be found in spurious eigenvalues. The strengths shown by the non-linear equalizer in single eigenvalue transmission, namely equalization of IQ-imbalances and amplitude noise, are of less

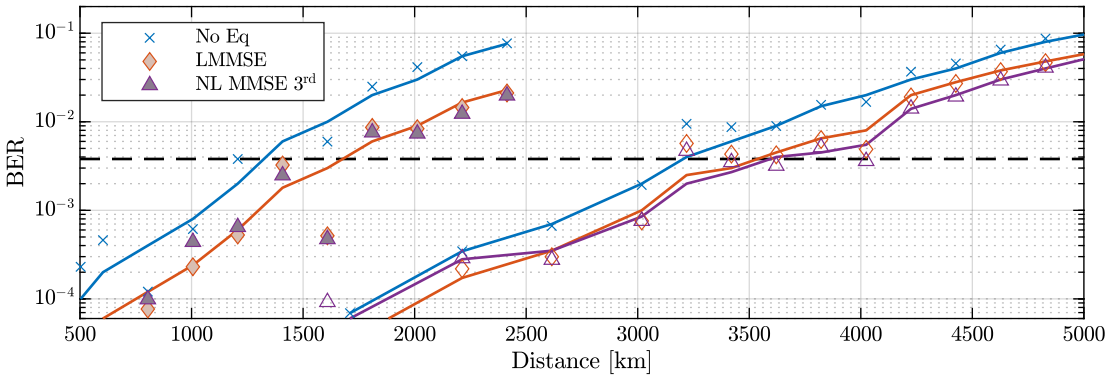

Figure 5.16: BER depending on transmission distance using single eigenvalue equalization for dual polarization, two eigenvalue transmission. Filled markers refer to 2 GBd transmission and unfilled markers to 1 GBd symbol rate.

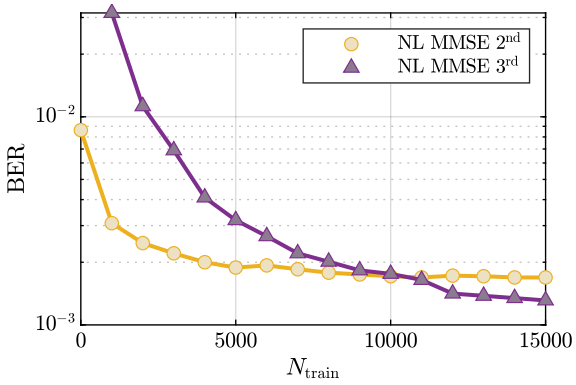

Figure 5.17: BER after cross-correlation equalization for 1 GBd dual polarization, two eigenvalue transmission for 3420 km.

importance here, as a simpler QPSK modulation was used.

In order to also use the correlations between eigenvalues of different polarizations, the non-linear equalizers were extended. The number of training symbols required is shown in Fig. 5.17. Here, the second-order NLMMSE requires 5000 training solitons to be trained out. The third-order NLMMSE, on the other hand, shows an improvement in BER when more than 10,000 training symbols are used.

The distance achieved using cross-correlation equalizers with BERs below the HD-FEC limit is shown in Fig. 5.18. Here, an improvement by increasing the equalizer order can be seen especially for the transmission with a high symbol rate. Overall, reach improvements can be observed in the region of 700 km for 2 GBd to 1000 km for 1 GBd transmissions.

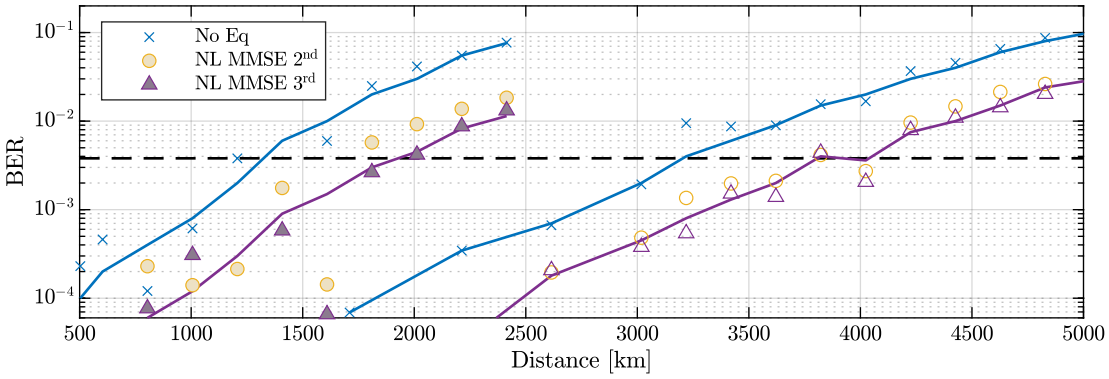

Figure 5.18: BER depending on transmission distance using cross-correlation equalization for dual polarization, two eigenvalue transmission. Filled markers refer to 2 GBd transmission and unfilled markers to 1 GBd symbol rate.

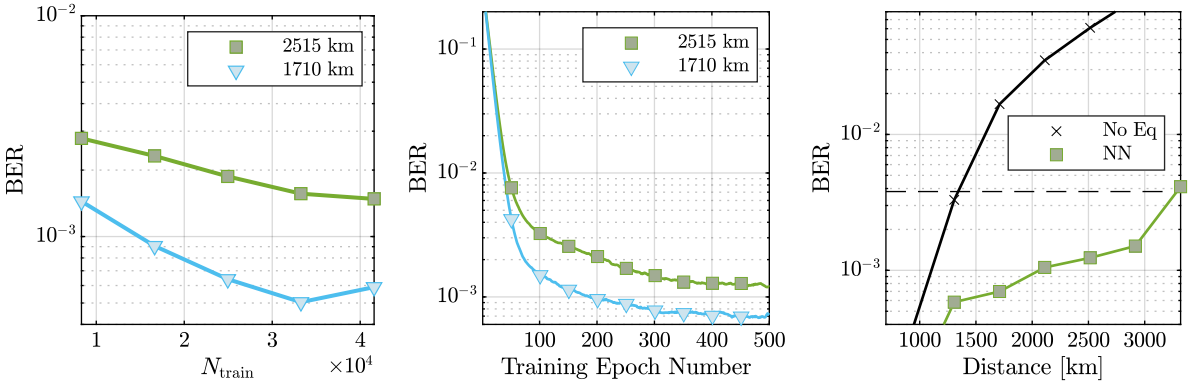

(a) BER depending on the number of training solitons.

(b) BER depending on number training epoch.

(c) BER depending on distance.

Figure 5.19: Determined BERs of single eigenvalue transmission for NN equalization depending on the training complexity for 1710 km and 2515 km transmission.

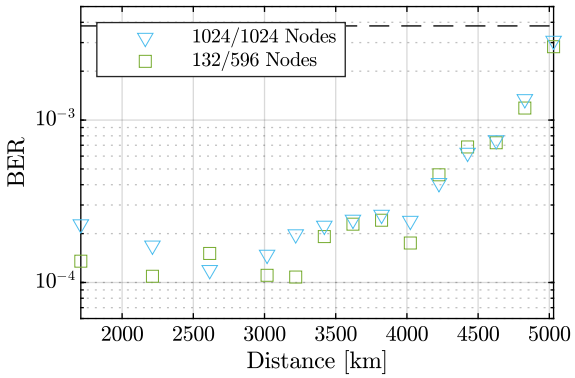

Figure 5.20: BER of DP 1 GBd 2 eigenvalue transmission after equalization using cross-correlation NNs for two network sizes: (triangle) 2 hidden layers with 1024 nodes each, (square) 2 hidden layers with 132 and 596 nodes, respectively.

5.4.4 Neural Network

The NN hyper-parameters used in the single eigenvalue transmission were determined heuristically. Satisfactory results were gained for an NN comprising of two layers with 250 nodes each. The used transfer function was the rectified linear unit (ReLU) according to $f(x) = \max(0, x)$. A drop-out of 50 % and an adaptive gradient descend method (the Adam algorithm [114]) were used during training with batch-sizes of 512. The training was based on minimizing the cross-entropy loss between the one-hot encoded class of the transmitted bit and output vector.

The amount of training solitons needed for the NN is depicted in Fig. 5.19a. The number of training solitons required is generally higher than that of the MMSE equalizers (see Fig. 5.13a). While for longer distances (here: 2515 km) already a relatively small number of 8000 training solitons achieve a good result (BER = 2.7e-3), which can only be minimally improved by increasing it up to 44,000 (BER = 1.4e-3), shorter distances benefit from more training data. For a shorter distance of 1710 km, the BER here drops sharply from 1.4e-3 (8000 training solitons) to as low as 5e-4 (33,000 training solitons). The number of training epochs required to fully train the NN is shown in Fig. 5.19b for both distances mentioned. The number of training solitons was set to 25,000. A fast approach to the optimum can be observed in the range up to 100 training epochs. To reach the optimum, however, more than 500 epochs are necessary for both transmission distances. Only minimal improvements can be observed here. However, since this is an offline process, the number of training epochs was increased to up to 1000 in the future in order to achieve optimal results.

The implemented cross-correlation NN equalizer was built to account for all cross-correlations between eigenvalues of differing polarizations. Hence, a more complex NN was designed. In this network, all $b_{1,2}(\lambda_i)$, $\Delta a'(\lambda_i)$ and $\Delta\lambda_i$ were used as inputs. This resulted in a total of 4 $b_{1,2}(\lambda_i)$, 2 $\Delta a'(\lambda_i)$ and 2

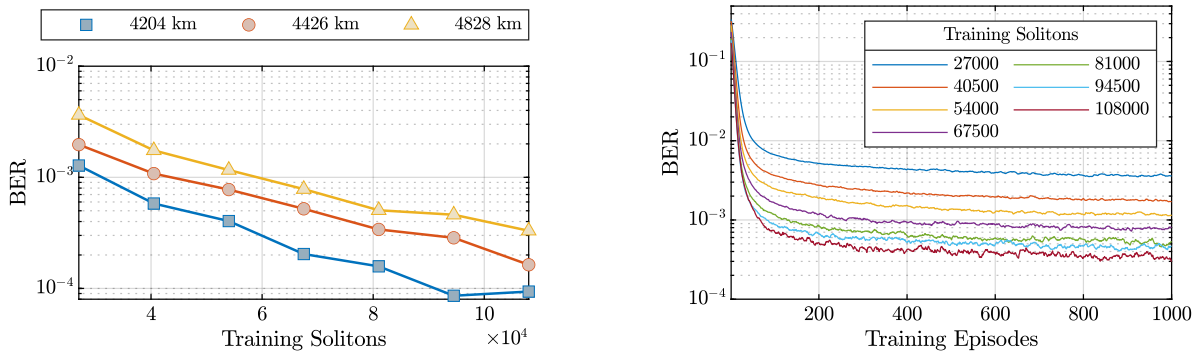

(a) BER depending on the amount of used training solitons for different transmission distances.

(b) BER for 4828 km transmission depending on the number of training episodes for different amounts of training symbols, denoted by the legend.

Figure 5.21: Required training for a cross-correlation NN equalizer taking the continuous spectrum into account. The NN was trained to equalizes the 1 GBd, 2-eigenvalue DP transmission.

$\Delta\lambda_i$. The output layer directly decoded all 8 bits encoded on each multi-soliton (QPSK, 2 eigenvalues, 2 polarizations). Since the softmax function was used here, the output layer was already 256 nodes in size. Because of the increased complexity of this network, the hyper-parameters were redesigned. Initially, two very large layers with 1024 nodes were used. The results are shown in Fig. 5.20. Since this network size is very large for online processing, it should be simplified. For this purpose, the required number of nodes per layer was redefined with the help of a random-search algorithm. In this way, a better combination of layer sizes could be found, which reduced the number of nodes to 132 and 596 for the first and second layers, respectively. As shown in Fig. 5.20, the performance of the network does not decrease, while the number of required multiplications was reduced by a factor of 5.7.

Subsequently, this equalizer was extended to also take into account correlations with the continuous spectrum as shown in Fig. 5.10a. The continuous spectrum was calculated between $\lambda = \mp 4$ and discretized using 161 steps. The input vector now consisted of the real- and imaginary parts of $\mathbf{x} = [b_{1,2}(\lambda_{1,2}), \Delta a'(\lambda_{1,2}), \Delta\lambda_{1,2}, b_{c,X}(\lambda), b_{c,Y}(\lambda)]$. It has been determined that the optimized hyper-parameters of the hidden layers did not change for this equalizer, leading again to hidden layer sizes of 132 and 596. However, due to the increased size of the input layer, new training sweeps have been conducted to determine the training complexity for this network.

The training effort can be seen in Fig. 5.21. Increasing the number of training solitons up to 108000 can lead to improvements of the BER (5.21a). This number could not be increased further because not enough data was generated to calculate a statistically valid BER. However, the improvement by using a very high number of training solitons is still very small and vanishes for shorter distances.

The needed training episodes for different amounts of training solitons are depicted in Fig. 5.21b. No dependence of the duration of the training on the number of training symbols can be observed. As

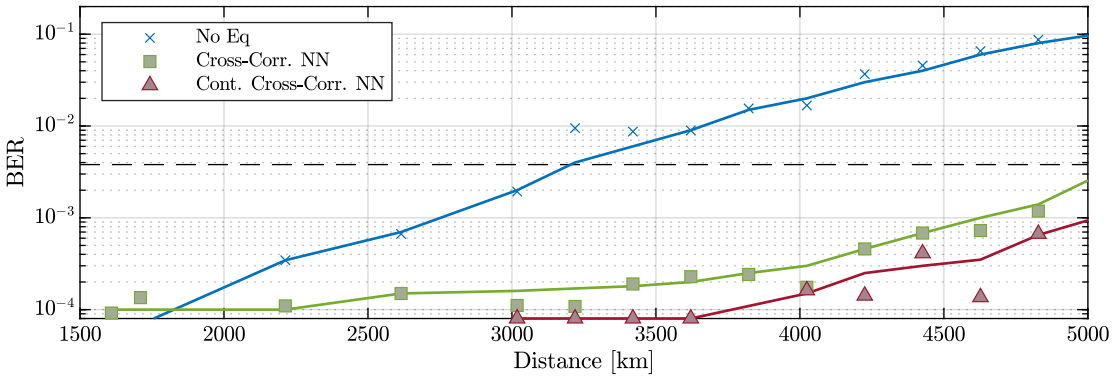

Figure 5.22: BER of DP 1 GBd 2 eigenvalue transmission after equalization using cross-correlation NNs. The NN using only the discrete spectrum was trained using 45000 training solitons and the NN also taking the continuous spectrum into account using 67500 training solitons. BERs below 8e-5 can not be displayed due to statistical validity.

with the other NN equalizers, 500-1000 episodes are sufficient. To compare the cross-correlation NN equalizers, Fig. 5.22 depicts the BER after equalization depending on the transmission distance. Here it can be seen that by taking into account the continuous spectrum, the NN can not only improve the overall performance, but also reduce the amount of errors for transmission distances below 3000 km to zero. Mind, that the exact BER up to 3621 km can not be computed due to an insufficient amount of transmitted bits. In contrast, the cross-correlation NN without continuous spectrum cannot adequately equalize especially shorter transmission distances and even worsens the BER. However, both NNs yield a BER below the HD-FEC limit for all measured distances up to 5018 km.

5.4.5 Comparison

In this section, the studied equalizers will be compared with regard to their complexity and their BER improvement. The complexity here is to be limited to online equalization, as it is assumed that the training is carried out offline, before the start of the transmission. To measure the complexity, the number of multiplications to be performed online is used. Since only ReLU transfer functions were used for the NN equalizers, the complexity of a node of an NN is limited to one comparator and one multiplier. The amount of multiplications needed for NN equalization then reads

$$N_{\text{mult,NN}} = \sum_{l=1}^{L-1} k_l k_{l+1} + \sum_{l=2}^{L-1} kl, \tag{5.36}$$

where L is the number of layers and k_l is the amount of nodes in layer l. The number of required multiplications of the MMSE equalizers corresponds to the number of their coefficients. For the linear

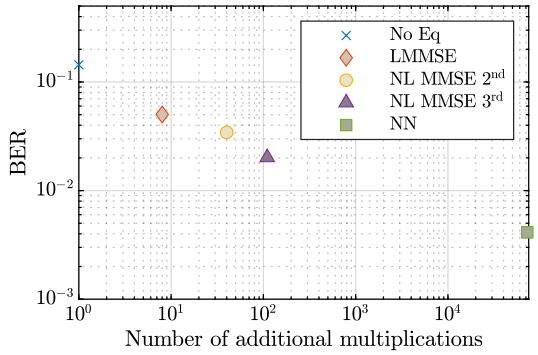

(a) Comparison of additional multiplications needed for equalization of the different equalizers for 3019 km reach.

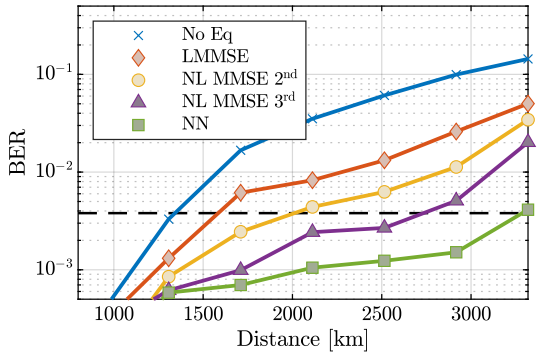

(b) Comparison of BERs after different equalization techniques as described above for single eigenvalue transmission. For readability the HD-FEC limit is included (dashed line).

Figure 5.23: Comparison of all equalizers w.r.t. complexity and performance.

Table 5.4: Comparison of equalizer techniques for single eigenvalue transmission at 3019 km reach

	N_{train}	N_{mult}	BER improvement
MMSE	≈ 2000	8	-8.87 dB
2nd-order NL MMSE	≈ 2000	40	-12.4 dB
3rd-order NL MMSE	≈ 6000	110	-17.1 dB
NN	$\approx 30,000$	72500	-30 dB

MMSE equalizer this is fixed to 4 and for the nonlinear MMSE Eq. (5.25) can be used. Mind, that this amount has to be doubled, since the MMSE equalizers account for amplitude and phase noise separately.

Single Eigenvalue Transmission

The resulting amount of needed multiplications for the considered equalizers is depicted in Fig. 5.23a. Fig. 5.23b compares the improvement in BER achieved by the different equalizers w.r.t. the transmission distance. Overall, with rising complexity of the equalizers a BER improvement can be seen. The amount of additional multiplications and needed training symbols are finally compared in Tab. 5.4

Transmission of Two Eigenvalues on Both Polarizations

The required number of multiplications to equalize all 4 b-coefficients of a soliton are shown in Fig. 5.24. Especially the complexity of the NN equalizers increases strongly here, since large hidden layers and a large output layer are used. However, a great benefit can be gained from the additionally used continuous spectrum. While the BER drops to 6.3e-4 (cf. BER without equalizer 1.11e-1, BER NN without continuous spectrum 2.8e-3), the number of total multiplications increases only insignificantly

Table 5.5: Comparison of equalizer techniques for double eigenvalue transmission at 5030 km reach

	N_{train}	N_{mult}	BER improvement
MMSE	≈ 2000	32	-3.2 dB
3rd-order NL MMSE	≈ 8000	440	-4.4 dB
2nd-order Cross. Corr. NL MMSE	≈ 8000	432	-6.7 dB
3rd-order Cross. Corr. NL MMSE	≈ 12000	1752	-9.3 dB
Cross. Corr. NN	$\approx 45,000$	234088	-32 dB
Cont. Cross. Corr. NN	$\approx 67,500$	255340	-45 dB

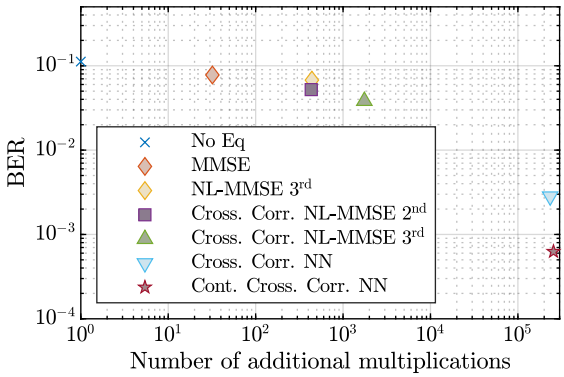

Figure 5.24: BER at the cost of complexity of all investigated equalizers for the DP, two eigenvalue transmission with 1 GBd symbol rate at 5030 km transmission reach.

compared to the cross-correlation NN without continuous spectrum.

In addition, it should be noted that all equalizers presented here have the potential to be highly parallelised, which can greatly reduce the overall duration of an equalization.

To quickly compare the different equalizers, the reader is referred to Table 5.5. Here, the training and equalization costs of the BER improvements are compared.

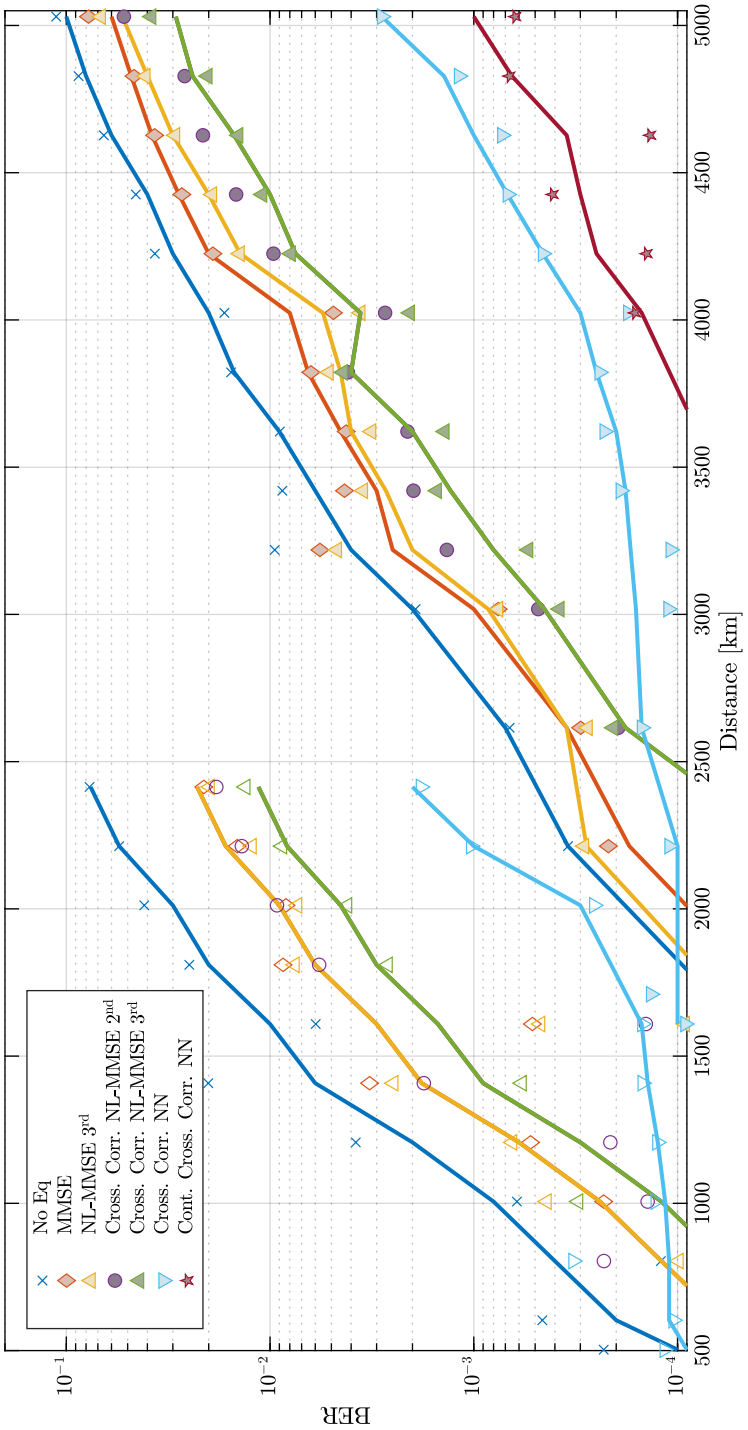

Figure 5.25: BER of all investigated equalizers for the DP, two eigenvalue transmission. Filled markers refer to 1 GBd transmission, unfilled markers to 2 GBd symbol rate.

5.5 Summary

In this chapter, disturbances such as low-pass behaviour and noise of the real channel on the discrete NFT spectrum were considered. These, in addition to unknown deviations of the modulated b-coefficient, lead to deviations of the eigenvalue. Since the transmitted eigenvalue can be assumed to be known, the deviation of the eigenvalue can be used to infer deviations of $b(\lambda_i)$.
For this purpose, (non-)linear MMSE equalizers and neural networks were introduced and experimentally tested in single and double eigenvalue transmissions using one and two polarizations.
Overall, with rising complexity of the employed equalizers also the performance increases, with NN equalizers reducing the BER by up to 45 dB and more than doubling the achievable transmission distance.

Chapter 6

Electronic Photonic Signal Processing for NFT Transmitters

Photonic signal processing is an approach to shape microwave signals in the optical domain [115][116]. This has the intrinsic advantage of optical transmission, namely extremely large bandwidths, a large frequency range and no electro-magnetic interference. Commonly, signals which are modulated over the RF/mm-wave spectrum have bandwidths up to 100 GHz. This accounts to only 0.05% of the available bandwidth for a 1550 nm optical carrier.

Using electronic photonic signal processing wideband operations such as beamforming for phased arrays, filters with an extremely high tuning range, photonic mixers or even photonic reservoir computing can be realised. In this section a silicon photonics (SiP) chip shall be designed and investigated, which is able to densely multiplex solitons. By exploiting the tight control over frequency and time-differences of the SiP chip, high spectral efficiencies in the field of soliton transmission can be reached in a scalable manner.

This chapter is organized as follows: First, it will be motivated why electronic photonic signal processing is used in the field of NFT-based soliton transmission. Then the SiP chip used will be presented conceptually and as a more defined architecture. The chip will first be characterised and then experimentally tested in transmissions of up to four soliton channels.

6.1 Motivation

Pulse shapes created in the digital domain by an INFT can be difficult to generate. This is illustrated in Chapter 4 and is not only due to the increasing bandwidth of higher order solitons, but also due to the increased dynamic range and vertical resolution required.

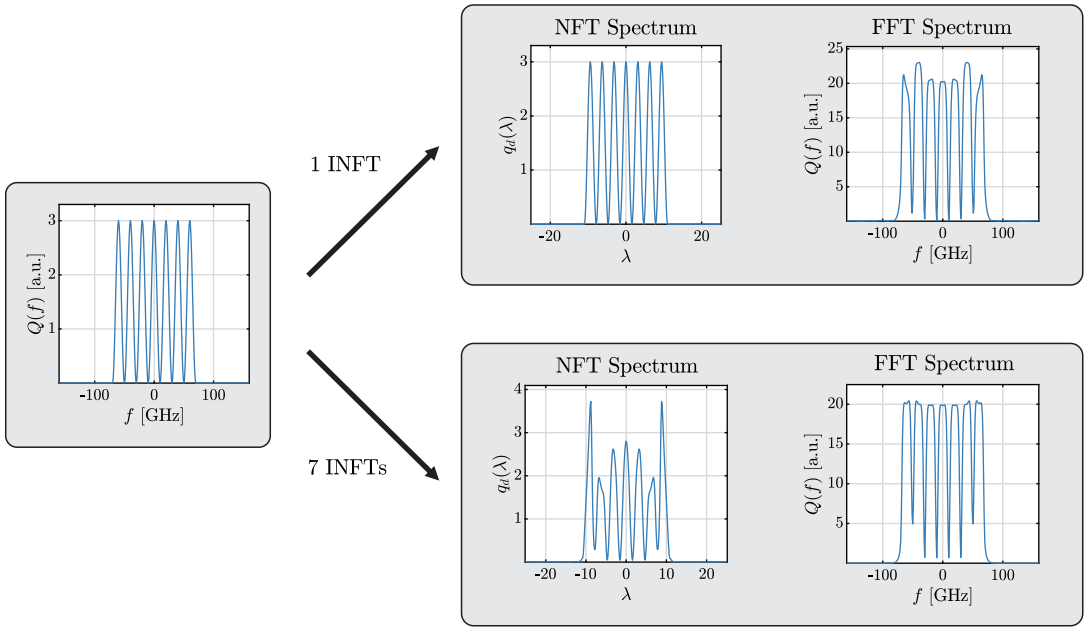

Figure 6.1: (left) Tx 7-channel WDM spectrum and resulting nonlinear and linear spectra after (top box) nonlinear multiplexing using one broadband INFT and (bottom box) linear multiplexing adding seven narrowband INFTs.

So to fill an entire band, it is necessary to perform many digital INFTs, which are then multiplexed. However, to ensure the linear transmission characteristics of multiple signals generated by INFTs, a non-linear multiplexer would have to be used due to the non-linearity condition

$$f(q_1 + q_2) \neq f(q_1) + f(q_2).$$

Therefore, a true NFT transmission using digital INFTs is not scalable due to the electrical bandwidth of the Tx and Rx components. For this reason, true NFT WDM transmissions are not yet feasible. To illustrate this graphically, Fig. 6.1 shows the two multiplexing methods described. Here, seven channels were multiplexed non-linearly using a single INFT (top) and multiplexed linearly after calculating seven separate INFTs (bottom). Only when a single INFT is calculated, seven orthogonal NFT channels emerge that evolve linearly (top box, left). However, if seven narrowband INFTs are calculated, which are then linearly multiplexed, this leads to interference between the channels as calculated by the NFT (lower box, left) and linear FFT (lower box, right). So far, linear WDM transmissions with INFT modulated signals have not been investigated in more depth.

In order to maintain the linear transmission characteristics of a channel, nonlinear de-multiplexing would also have to be available, even if nonlinear multiplexing was possible. Alternatively, the NFT

would have to be calculated over several channels in order to also consider XPM between channels, which in turn would need very broadband receivers. As an option to keep the required Rx bandwidths low, large spectral guard bands could be used. These, however, would reduce the spectral efficiency and possibly negate the gain of using NFT processing.

A multiplexing scheme enabling broadband super-channels, to reduce the spectral efficiency fallout associated to the guard bands, but that remains compatible with eigenvalue communications, would thus be a powerful tool [117][118] and a step towards fully modulated and scalable NFT multiplexing.

To decrease electrical and electro-optic hardware requirements and facilitate a scalability of NFT-based transmission systems an SiP chip is used to shift the synthetization of higher-order solitons to the optical domain. To create a dense multiplexing, first order solitons that are overlapping in time and frequency domain are phase- and amplitude modulated and optically merged within the chip and the transmission link. Thus, guard bands can be omitted and even an overlapping of the spectra is made possible. This not only decreases the generation requirements significantly (see Chapter 4.2) but also maximizes spectral efficiency.

To enable this, the required tight control on differential frequency and timing of the solitons is made possible by the SiP chip. Integrated platforms enable robust systems with precise pulse interleaving for optical time division multiplexing [119], [120] and have enabled control to interleave pulses in the picosecond range [121].

6.2 Silicon Photonics Integrated Circuit

This section will explain the concept of the photonic integrated circuit (PIC). The actual design and its limitations will then be described and explained. The aim of the chip design is to individually modulate up to 4 soliton channels and then multiplex them with reconfigurable time delays. The idea of the chip is to be scalable to more than 4 channels to potentially fill all available frequency bands.

6.2.1 Concept and Architecture

A conceptual circuit is shown in Fig. 6.2. Here a bit-stream is parallelised and modulated onto the b-coefficient by (A)PSK modulation. The eigenvalues shown are intended to represent the four solitons, which can be calculated either by a numerical INFT (here the Darboux transform) or, since only first-order solitons have been used so far, analytically (see Eq. (4.1)). The digitally generated first-order solitons are then converted into the analogue, electrical domain by a DAC. These analogue electrical signals are connected directly to the IQ-MZMs on the chip. The IQ-MZMs each modulate a filtered laser line of a laser comb-source. By using a comb-source, a very uniform and constant Δf can be guaranteed. The solitons, now converted into the optical domain, pass through a reconfigurable delay

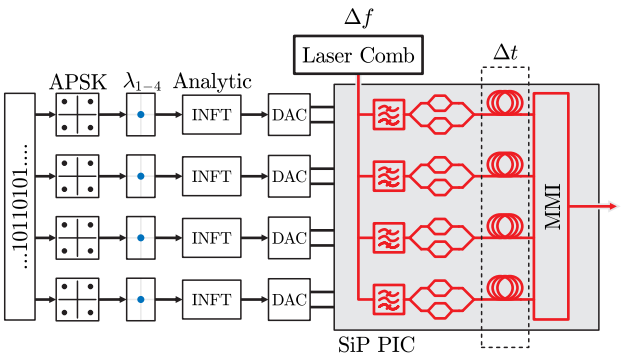

Figure 6.2: Concept of the envisioned SiP chip: A bit sequence gets parallelized into four channels, each modulating a first order soliton. A laser comb source supplies evenly spaced laser lines, which get fed and filtered into each channels bus on the chip. The filtered laser lines get modulated by IQ-MZMs to yield phase modulated solitons. The modulated solitons get delayed by a network of reconfigurable delay-lines to get a dense time division multiplexing and multiplexed onto a common output bus afterwards.

network, which can provide very precise control over Δt. Finally, all solitons are multiplexed onto a common BUS using an MMI and routed to the output of the chip.

The now arising question is how small Δf and Δt can be chosen in terms of T_0, while preserving the eigenvalues and thus the desired transmission properties. Additionally, a T_0 has to be determined to yield solitons which are adapted to the available fiber loop setup. Afterwards filter bandwidths and delay line lengths can be set.

The present fiber loop, adapted to soliton communications, consisted of 50 km NZDSF spans. With the help of lumped amplification using EDFAs, the fiber loss was compensated. The first condition imposed on the soliton width is then that of the guiding center soliton $\xi_A = L_A/L_D \ll 1$ (see Chapter 2.1.5) with $L_D = T_0^2/|\beta_2|$. Since L_A and β_2 are parameters fixed by the present fiber, one can calculate

$$T_0 \gg \sqrt{|\beta_2| L_A}. \tag{6.1}$$

Now L_A is fixed to 50 km and $\beta_2 \approx -5.74\text{e}-27\,\frac{\text{s}^2}{\text{m}}$, which leads to $T_0 \gg 16.94\,\text{ps}$. Since the soliton channels are to be multiplexed very closely in the frequency domain, it is also necessary to consider the condition $L_{\text{coll}} \gg L_A$. Otherwise, a frequency offset due to too short collision distances can cause problems in the detection due to the very narrow multiplexing. Using Eq. 2.18 one can calculate $T_0/\Delta f \gg \frac{L_A}{9.778\text{e}25\,\text{m/s}^2} = 5.114\text{e}-22\,\text{s}^2$. This can be rewritten into

$$\Delta f \ll T_0/5.114\text{e}-22\,\text{s}^2. \tag{6.2}$$

From Eqs. 6.1 and 6.2 one can see that T_0 should be chosen as large as possible to get robust solitons and less impact due to collisions from more distant channels.

Since the spectral efficiency of a soliton is fixed, it is recommended to use larger T_0 (with larger absolute time-division spacing $\Delta\tau$ and smaller absolute frequency spacing Δf of the channels) to get a robust transmission with regards to the conditions of the guiding center soliton and collision lengths.

Given the discussion above, a soliton width of $T_0 = 60\,\mathrm{ps}$ was set to carry out the further examinations. This value was chosen conservatively, since this leads to $\Delta f \ll 117.3\,\mathrm{GHz}$ and $L_D \approx 435.6\,\mathrm{km}$ and also leads to less demands with regards to total bandwidth of the chip and hence possibly cheaper components.

Following Fig. 4.10, one can see that for two eigenvalue multiplexing, minimum multiplexing parameters ΔT and Δk can be chosen to be

$$\Delta T_{\mathrm{min}} = 2.5$$
$$\Delta k_{\mathrm{min}} = 1.5,$$

to get dense multiplexing without much perturbation, keeping in mind that multiplexing of four channels could increase the perturbations. This leads to multiplexing parameters in physical units

$$\Delta\tau_{\mathrm{min}} = 150\,\mathrm{ps}$$
$$\Delta f_{\mathrm{min}} = 9.5\,\mathrm{GHz},$$

which were the core parameters during the design of the chip.

6.2.2 Design and Components

Figure 6.3 shows a block diagram of the integrated system and Fig. 6.4 a micrograph of the fabricated chip. Four 2nd-order CROW OADMs distribute the different laser lines into the two IQ MZMs.

This makes it possible to modulate four channels, while only two complex signals and IQ-MZMs need to be used. In turn one four-channel AWG (Keysight M8169A) is sufficient and reduces the implementation efforts for modulators. Thus, at the beginning, channels 1 and 3 (or 2 and 4) carry the same information (see wavelength labelling in Fig. 6.3). However, channels 3 and 4 are delayed by 300 ps or 500 ps after modulation, depending on the selection of the 4-ring CROW OADMs. By adjusting the baud rate, these channels now travel in the subsequent symbol clock and generate four independent solitons there. By selecting the 300 ps delay line and a symbol duration of 600 ps, evenly distributed solitons with $\Delta t = 150\,\mathrm{ps}$ can be generated. If the 500 ps delay line is selected in combination with a symbol duration of 1 ns, Δt increases to 250 ps.

Since channels 1 and 3 (or 2 and 4) do not overlap, they can be multiplexed with CROW OADMs onto one output bus each without crosstalk. These 2 bus waveguides can finally be coupled by an MMI, as this does not filter the spectra and thus allows overlapping. However, this comes at the cost of 3 dB

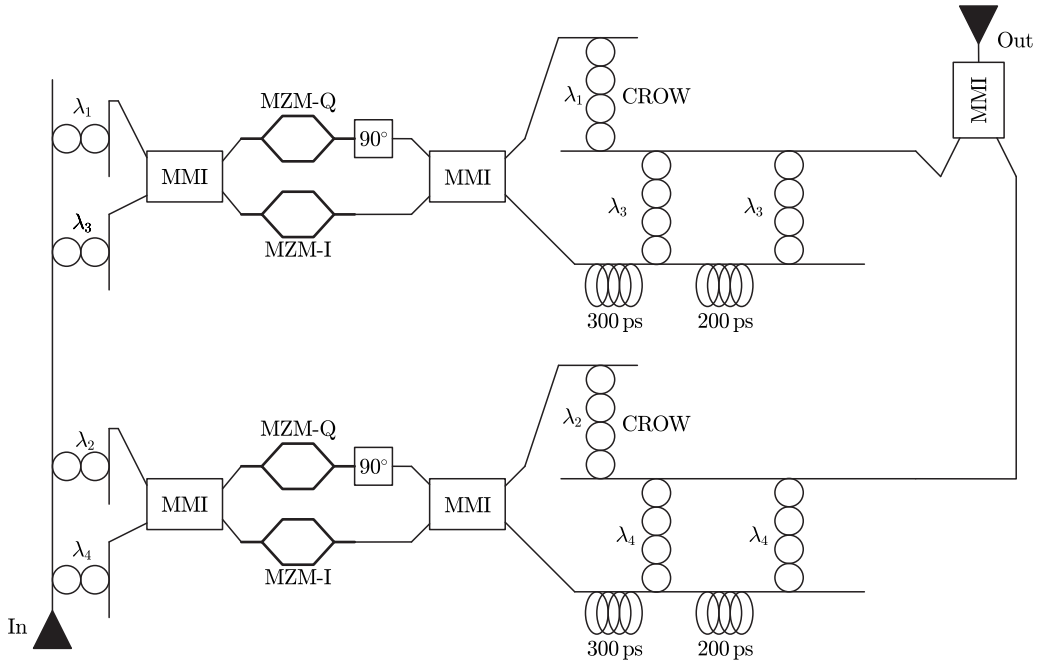

Figure 6.3: Design of the SiP chip: Four narrow-band two ring coupled (ring-) resonator optical waveguides (CROWs) (left hand side) let the selected laser lines pass. Two channels get modulated by an IQ-MZM. Afterwards one channel gets routed directly to the output bus, while the other one gets delayed by 300 ps or 500 ps into the following soliton window to get four independently modulated solitons.

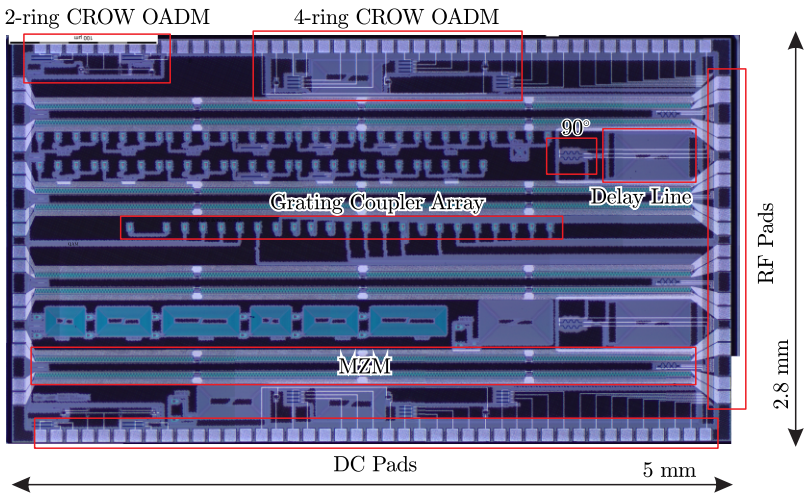

Figure 6.4: Micrograph of the created SiP PIC.

additional insertion losses due to reciprocity. But this penalty is incurred only once, irrespective of the number of channels.

Important re-configurable elements of the PIC are the CROWs and MZMs. The 2nd-order CROW filters, which are used to filter the laser lines into the modulators, have an insertion loss (IL) of 2 dB and a 3-dB bandwidth of 7.5 GHz when both rings are aligned, as depicted in Fig. 6.5a. Due to the design with only two rings, the filter slope is not very steep. This leads to a 5-dB bandwidth of around 10 GHz and is the lowest possible frequency spacing of the channels. The 4th-order CROW OADMs have 3 dB IL and a 3-dB BW of 15 GHz after alignment (Fig. 6.5a). Because of the large bandwidth of the fourth order CROW-filters relative to the -20-dB bandwidth of a 60 ps soliton (approximately 10.1 GHz), and the distortion-less combination of the BUS waveguides using an MMI, the chip can be assumed to be an almost perfect linear superposition of the four soliton channels. This, however, needs very precisely adjusted voltages for each ring of the CROWs, leading to a total of 32 voltages which need to be controlled. The IQ-MZMs consist of 4.4 mm long phase shifters, which can also be clearly seen in Fig. 6.4. Complementary phase shifters are operated in nested MZMs in GSSG configuration. Since only four AWG channels and matched RF amplifiers were available, the RF-signal had to be split electrically leading to a maximum driving voltage at the MZMs of 2 Vpp. If only two channels were being modulated, the driving voltage could be doubled to 4 Vpp. The IL is below 4 dB and the electro-optic cutoff frequency is 13.8 GHz and is thus adapted to the present application. When driven with 2 Vpp signals and biased for QPSK modulation, this results in a combined IL and modulation penalty of 12.3 dB, which lowers to 7.7 dB at 4 Vpp. This penalty is defined here as the attenuation of the peak power after modulation since nested modulators are biased at the zero-transmission point.

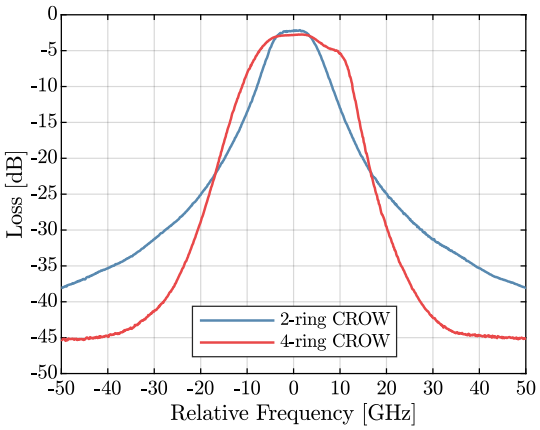

(a) 2-ring and 4-ring CROW frequency response.

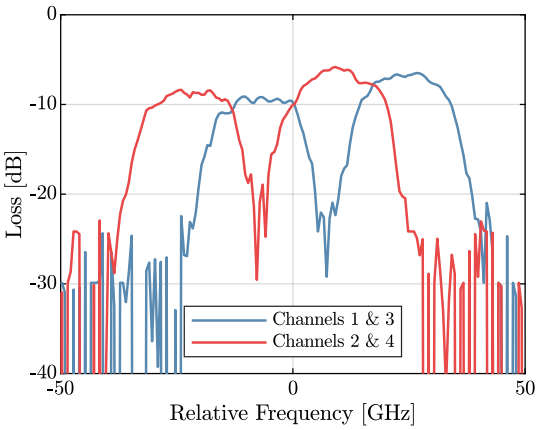

(b) Reconfigurable output network response after alignment.

Figure 6.5: Measured frequency responses of (a) CROW OADMs and (b) full chip.

Since the line power of the comb source was very low and the set up system could tolerate slight frequency fluctuations between channels, discrete cavity lasers were used (Agilent N7714A). The output power of the four lasers could be adjusted separately and were thus set to 12 dBm for channels 3 and 4 and 8 dBm for channels 1 and 2. This compensates for the additional IL of the delay lines (see Fig. 6.5b). In total, the optical losses were as follows: 1) The external 4x1 multiplexer to multiplex the laser lines introduced an IL of 7 dB; 2) the input and output grating couplers cumulatively added an IL of 7.5 dB; 3) 2nd- and 4th-order CROW OADMs added a cumulative IL of 5 dB; 4) the IQ-MZMs an insertion and modulation penalty of 12.3 dB for 2 Vpp drive voltage (4-channel experiments); 5) delay lines an IL of 4 dB; 6) the output MMI an IL of 3 dB due to reciprocity (with negligible excess losses); and 7) interconnect waveguides and monitor taps a cumulative 3 dB IL. Thus a soliton-pulse peak-power of -29.8 dBm at the PIC output was gained. These values have been used to adjust the required amplification at the PIC output to reach the calculated soliton peak power launch condition of 3.9 dBm calculated based on the path-average conditions.

6.3 Experimental Verification

In order to verify the theoretically developed models of soliton multiplexing, several experiments were carried out. In the course of the processing time, 2 PICs were manufactured, whereby the first PIC could only modulate channels 1 and 3. Experimental investigations with increasing complexity were thus carried out. Here, the multiplexing parameters were chosen to be progressively denser. In the first set of experiments, only two channels using the first chip were modulated. This led to the possibility to

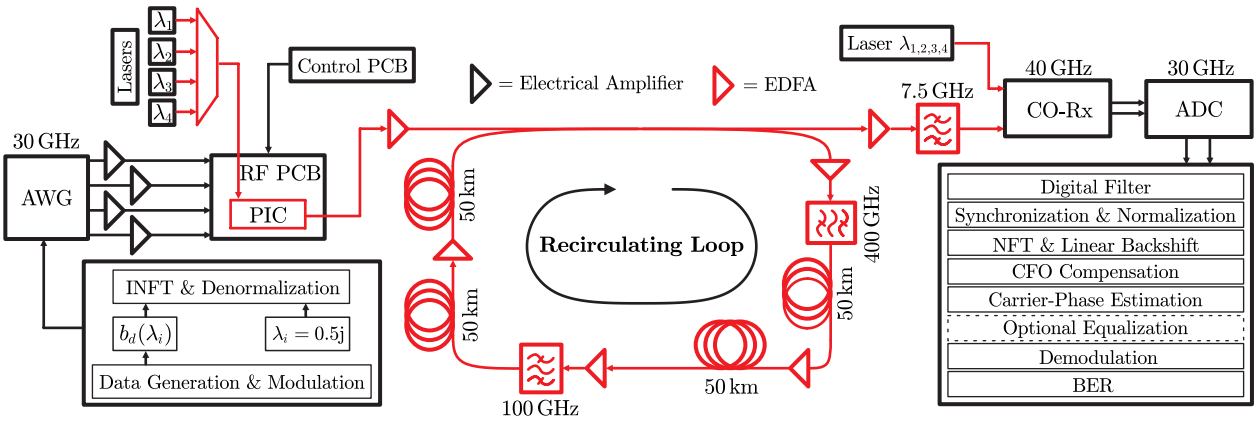

Figure 6.6: Experimental setup for the four-channel measurements.

drive the MZMs with 4 Vpp RF-signals, since two RF-amplifiers could be used for each differentially driven quadrature. This enabled later comparisons with a 2 Vpp driven MZM, to verify, if there are PIC-external bottlenecks in this experiment. Afterwards, all four channels were modulated, but with a coarser multiplexing scheme to be comparable to the two-channel transmission. This facilitated the verification of possible penalties due to cross-talks or problems in the heat-distribution because of using all four channels. Finally, in the last set of measurements the channels were multiplexed as dense as possible and even amplitude modulation of the b-coefficient was introduced, in order to determine the maximum possible spectral efficiency enabled by the chip.

6.3.1 Experimental Setup

The experimental setup for a 4-channel transmission is shown in Fig. 6.6. The DSP block on the transmitting side is independently executed twice. A 4-channel AWG (Keysight M8196A, 80 GS/s, ENOB $\approx$5.5) serves as a DAC and generates inphase and quadrature portions of two parallel soliton streams. Each stream consisted of 2000 solitons and an additional zero padding of 5 ns for synchronization purposes. The solitons are amplified to a swing voltage of 4 Vpp using electrical RF amplifiers (SHF S807). Because of the GSSG configuration, these are split by 3 dB splitters and then provide 2 Vpp swing voltage, which is DC-blocked and then connected to the PIC's RF PCB. As described in Section 6.2.2, four cavity lasers (linewidth <100 kHz) with powers of 8 and 12 dBm are used as carriers, coupled with the aid of a 6 dB coupler and fed into the chip using grating couplers. The control PCB is connected to the RF PCB by means of ribbon cables. The control PCB is managed by a PC via USB. This allows the MZMs to be biased and the CROW OADMs to be adjusted using software. The PIC output (average power of 4 channels now ≈ -36 dBm) is amplified by an EDFA and fed into a recirculating loop. The recirculating loop consists of 4 spans of 50 km NZDSF. The attenuation is compensated by EDFAs (NF

$\approx 5\,\mathrm{dB}$). As seen in Fig. 6.6, two filters inside the loop are used to remove out-of band noise. After the desired number of loops have been passed through, the received signal is first amplified again. Then the channel(s) under test are filtered by a narrow-band optical filter (bandwidth of 7.5 GHz for one channel). The optical to electrical conversion is done by means of a NeoPhotonics μ-ICR coherent receiver. An additional laser (linewidth <10 kHz) served as local oscillator and an oscilloscope (Keysight DSOZ634A, 80 GS/s, ENOB ≈ 5.5) as ADC.

The digitized Rx signal was digitally filtered by a 3^{rd}-order Butterworth filter with a 3 dB bandwidth equal to two thirds of the solitons' 20 dB bandwidth. Afterwards the signal was synchronized using the zero padding and normalized into NFT units, which was followed by the NFT and one-step back propagation according to (3.37). The carrier frequency offset (CFO) was computed by calculating the mean real-part of the eigenvalues and subsequently compensated, which was followed by either a blind- or a pilot based carrier-phase estimation. Afterwards, the different equalization techniques as described in Section 5 were used, which was followed by the demodulation of the QPSK symbols (if no NN was used) and subsequent BER calculation.

6.3.2 Two Channels

In this set of two-channel measurements the general capability of the chip to generate solitons was verified. This was followed by comparisons of multi-channel and single-channel equalization schemes. For the two-channel measurements, all four available AWG channels and amplifiers were used to achieve 4 Vpp swing voltage and in turn maximum Tx OSNR, which was subsequently compared to a transmission using only 2 Vpp swing voltage. This enabled the comparison of two- versus four-channel transmissions, which only allowed for 2 Vpp swing voltage. The differential frequency was set to 30 GHz and the time-domain spacing to 500 ps with a baud-rate of 1 GBd. This results in very low to no interference between channels.

First, the average launch power for this transmission had to be determined. For this, two channels were transmitted and the launch-power was swept at 2800 km transmission distance. The results are depicted in Fig. 6.8a. Here, the best results were seen at launch-powers of -2 dBm. This fits the calculated loss-less path averaged launch-power of approximately -2.33 dBm. To calcualte this, an attenuation of 0.2 dB/km, dispersion of $D = 4.6\frac{\mathrm{ps}}{\mathrm{nm\cdot km}}$ and nonlinearity $\gamma = 1.6\frac{1}{\mathrm{W\cdot km}}$ were assumed. Deviations from this value in experiments can be due to small variances of the fiber-parameters or insertion losses into the fiber. If only one channel was transmitted, 3 dB were substracted from the experimentally gained optimal launch power for two channels.

Since the experimentally found optimal launch power corresponds to the theoretically calculated launch power required for the formation of solitons, it can be concluded that solitons were indeed generated with the chip. This can also be qualitatively be seen in Fig. 6.7, where the pulse-width does

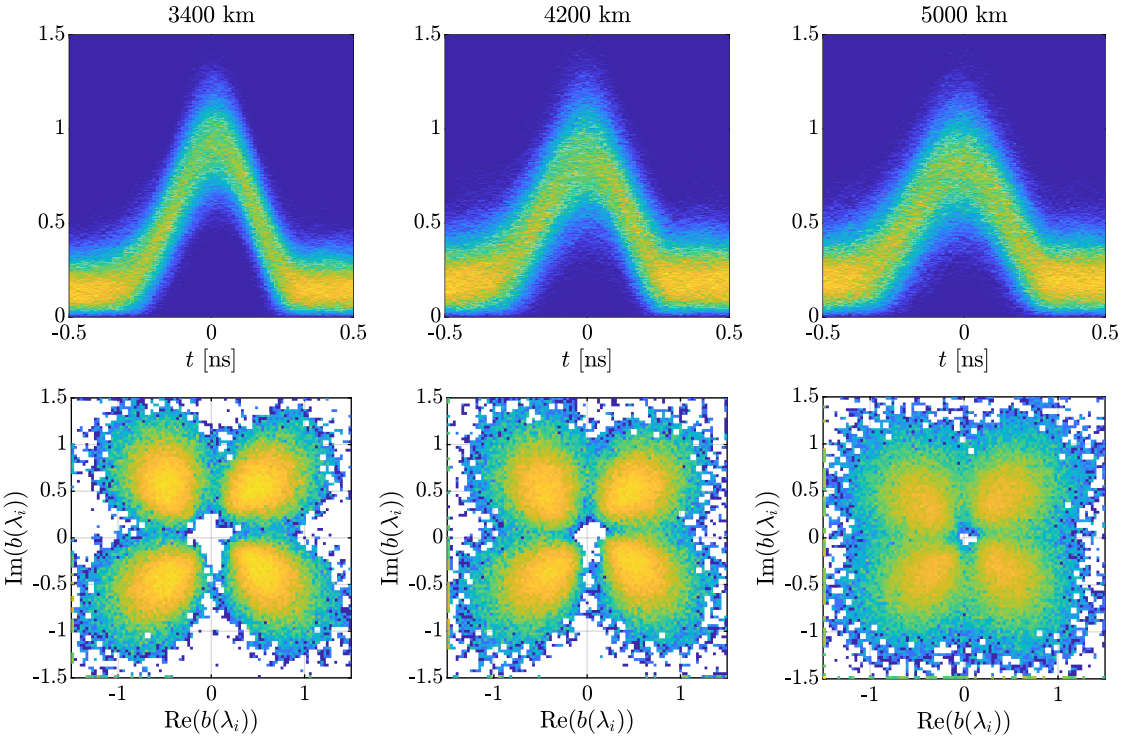

Figure 6.7: Eye-diagrams and constellations for (left) 3400 km, (middle) 4200 km and (right) 5000 km transmission.

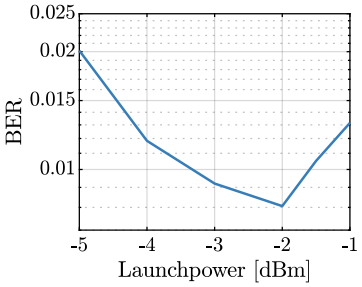

(a) BER depending on the launch power for two channel transmission at 2800 km transmission distance.

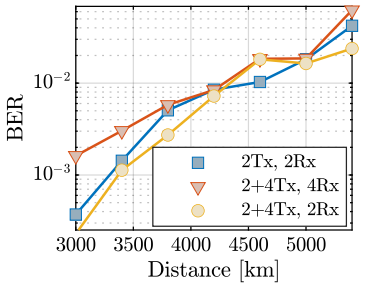

(b) BER depending on the distance for different channel configurations.

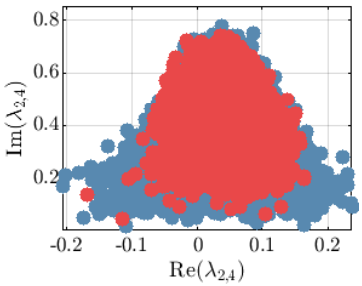

(c) Received eigenvalues after transmitting both channels and receiving a single channel after 3000 km. (Red) channel 2 and (blue) channel 4.

Figure 6.8: Measurement results of the two-channel measurements using 4 Vpp driving voltage and transmitting either only channel two or channels two and four.

not increase with increasing transmission distances.

Analysis of Single Channel Reception

To set the IQ-MZM, only channel 2 was used first. Afterwards, the laser of channel 4, being modulated by the same IQ-MZM, was turned on to measure a two-channel transmission. The first measurement results are depicted in Fig. 6.8b. In general, no penalty can be seen due to multiplexing two channels. This is to be expected, since no dense multiplexing was taking place and the soliton collisions were accounted for by the channel spacing and soliton width. This led to transmission distances below the assumed soft-decision forward error correction (SD-FEC) limit of 1.25e-2 up to 4400 km. However, detecting channel four led to worse performances than the detection of channel 2. This can also be seen in Fig. 6.8c, where the detected eigenvalues after 3000 km transmission are shown. It can be seen that the eigenvalues of channel 4 scatter much more than those of channel 2. This could be reversed by adjusting the MZMs. However, a perfect adjustment of both channels at the same time was not possible. Nevertheless, it should be noted that solitons were generated in both channels, since eigenvalues were detected.

To investigate the influence of the driving voltage on the transmission quality, it was reduced to 2 Vpp. A comparison is shown in Fig. 6.10a. Due to the reduced voltage swing, the transmitted signal power is reduced by 4.6 dB and in turn the transmission distance at the assumed SD-FEC limit decreases by 1200 km. From this, it can be seen that one bottleneck is not directly on the chip, but in the preceding transmitter hardware, which should be taken into account in the four-channel measurements that follow later.

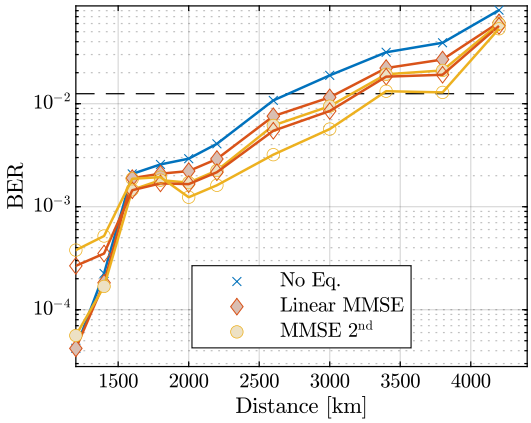

(a) BER depending on the distance for two channel transmission and reception using different equalizers. Filled markers refer to single eigenvalue equalization, unfilled markers to cross-correlation equalization.

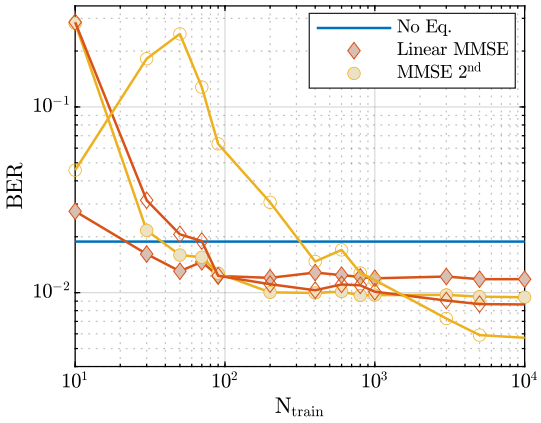

(b) BER depending on the amount of training symbols for two channel transmission and reception at 3000 km, using different equalizers. Filled markers refer to single eigenvalue equalization, unfilled markers to cross-correlation equalization.

Figure 6.9: Measurement results of the two-channel measurements using 4 Vpp driving voltage and transmitting and receiving two channels

Analysis of Dual Channel Reception

Since the receivers' bandwidth was high enough to detect both channels, this was done to investigate multi-channel equalization similar to the cross-correlation equalizers in Chapter 5. The Rx local-oscillator was set between channels two and four and the receiver filters bandwidth to 50 GHz. In this configuration, the overall transmission distance was reduced when compared to the single sub-channel reception and only 2600 km could be reached (see Fig. 6.9a) with BERs below the assumed FEC-limit. This is a consequence of the broader receiver filters and subsequent lower subchannel powers at the photodiodes of the coherent receiver. After all, only about 21 GHz of the 50 GHz reception bandwidth were filled with solitons. Since the maximum allowable optical power could not be increased due to the photo receiver damage threshold and nonlinearities, the total signal power was reduced and additionally superimposed by the noise of the electrical TIAs after the optical to electrical conversion.

However, this enabled cross-correlation equalization to be tested and compared with single-channel equalization. As one can see, especially nonlinear equalization can increases the transmission distance below SD-FEC by 800 km up to 3400 km. The amount of needed training symbols is depicted in Fig. 6.9b. For the linear MMSE equalizer, only about 100 training solitons are needed to be well adjusted. The second order nonlinear equalizer in comparison requires around 200 training solitons, which can still be considered a low amount. Although, the training effort for the nonlinear multi-channel receiver rises drastically, with around 5000 solitons being needed to be well adjusted.

In general, additional range improvement can be achieved with better matched receiver hardware, if both channels are equalized together. However, since the existing hardware was not adapted to this case, multi-channel reception was not used in the following.

6.3.3 Four Channels

For comparability, the channel settings of the two-channel measurements were kept first. The channel spacing of channels 1 and 3 (respectively 2 and 4) was 30 GHz. This resulted in a channel spacing of 15 GHz on the main bus. The same delay lines were also used. The spacing in the time domain on the main bus was therefore halfed to 250 ps.

Subsequently, the solitons were more tightly multiplexed within the chip. The frequency spacing was 10 GHz and the spacing in the time domain was 150 ps. These are the target values discussed earlier. However, the symbol rate was left at 1 GBd to keep the sample rates comparable and to be able to attribute any degradation to the multiplexing.

After that, both tight multiplexing on the chip and reducing the symbol duration to 600 ps were introduced. This resulted in the highest spectral efficiency achievable with this chip without any amplitude modulation of $b(\lambda_i)$. To increase this even further, time domain modulation of the solitons was then added using 2ASK-4PSK modulation.

Analysis of quality degradation by using four channels

$$\boxed{\Delta t = 250\,\text{ps},\ \Delta f = 15\,\text{GHz},\ 1\,\text{GBd},\ 8\,\text{GB/s aggregated},\ 0.1455\,\text{b/s/Hz}}$$

These settings are not primarily chosen to achieve the highest possible spectral efficiency. Instead, the aim here is to validate, if any crosstalk occurs within the PIC due to the spatially tightly packed hardware. To ensure comparability with the two-channel transmissions, the multiplexing parameters between the odd and even channels have not been changed here. All carrier lasers were now used to create four soliton channels. In Fig. 6.10b it can be seen that these have no influence on the performance. At short distances, a degradation of the BER can be observed, while at longer distances it is even better than that of the two-channel measurement. However, this is due to measurement variations. The range under the SD-FEC does not change and remains at 3000 km.

To test the influence of equalization on the transmission range, single-channel equalizers were applied to the received channel. These were the linear MMSE equalizer, a non-linear second order equalizer and a neural network. For the size of the network, the findings of the dual-polarisation experiments (see Section 5.4.4) were initially used. Here, too, no better performance was found with changed network parameters, which is why the network size did not change. The number of hidden layers was again two, containing 132 and 596 nodes, respectively.

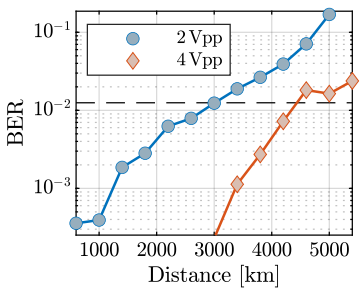

(a) Two channels using different driving voltages of the MZMs.

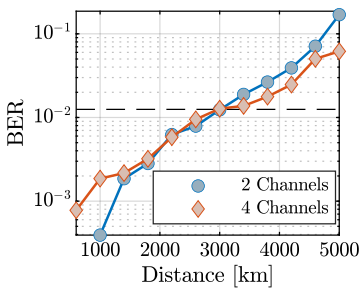

(b) Two versus four channel transmission using 2 Vpp driving voltage.

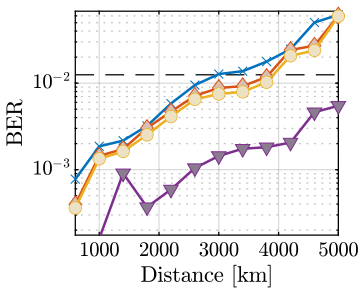

(c) Equalization of the 4-channel transmission: (blue, x): no equalization, (red, diamond): linear MMSE, (yellow, dot): 2^{nd}-order NL-MMSE, (purple, triangles): neural network equalization.

Figure 6.10: Four channel measurements using the first set of settings to compare two-channel and four-channel transmission. For readability, the assumed SD-FEC limit of 1.25e-2 is included (dashed line).

With the help of the linear MMSE equalizer, the transmission range at the SD-FEC limit could be increased by approx. 800 km to 3800 km. This could only be minimally improved by the non-linear equalization. This is again explained by the lack of amplitude modulation, which is the main beneficiary of non-linear equalization.

However, the neural network was able to significantly increase the transmission distance. Thus, 5000 km with BERs below the SD-FEC limit could be achieved and even 4200 km could be transmitted at the HD-FEC limit.

Analysis of narrow multiplexing

$$\boxed{\Delta t = 150\,\text{ps},\ \Delta f = 10\,\text{GHz},\ 1\,\text{GBd},\ 8\,\text{Gb/s aggregated},\ 0.2\,\text{b/s/Hz}}$$

In these measurements, the multiplexing parameters were chosen as derived in Section 6.2.1 and on which the system architecture of the chip is based. However, the symbol rate was not changed initially. Thus, the number of samples per soliton remains the same as in the previous measurements. Consequently, a penalty due to relatively lower sample rates can be excluded.

First, the optimal launch power was first determined and compared with the theoretical launch power. The results of this measurement are shown in Fig. 6.11a. As can be seen, the optimal launch power of -5.5 dBm deviates strongly from the calculated launch power of approximately 1 dBm. In a four-channel transmission, the launch power of -5.5 dBm would be required for transmission of solitons with a width of 249 ps. Interestingly, theses solitons actually emerge during fiber propagation (the transmitted spectra correspond to solitons with $T_0 = 60\,\text{ps}$ as can be seen in Fig. 6.12a) and keep

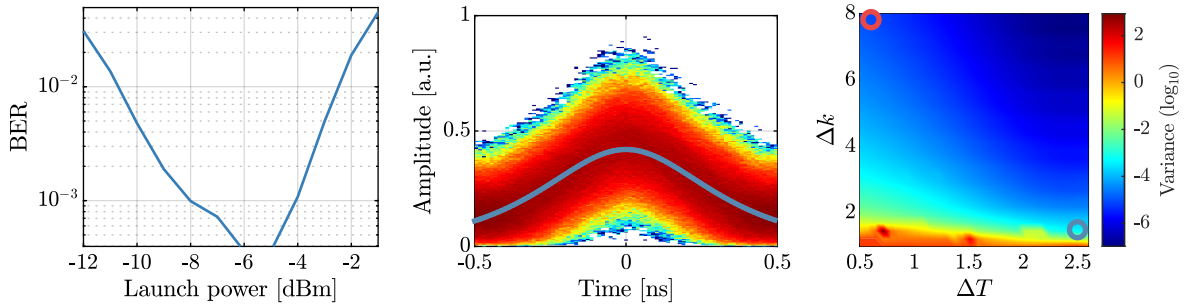

(a) BER depending on the launch power for dense four channel multiplexing (second settings) at 3000 km transmission distance.

(b) Received time-domain eye-diagram after 5800 km transmission. Blue overlay shows a soliton pulse with $T_0 = 249$ ps, which corresponds to the optimum launch-power of -5.5 dBm.

(c) Variance of the phase-deviation due to linear multiplexing with different multiplexing parameters. The blue circle refers to the transmitted parameters, while the red circle refers to the received ones due to temporal broadening: Δk changes, despite Δf being constant. This is due to the normalization using different T_0.

Figure 6.11: Measurement results of the narrow multiplexing, four-channel experiments.

this width for transmission distances up until the longest measurement of 5800 km, as can be seen in Fig. 6.11b. It can be concluded, that a solitonic transmission is maintained, but a better BER is obtained with wider pulses that reduce the frequency overlap between the channels at the cost of a higher temporal overlap. Looking at Fig. 6.11c this is not entirely surprising. Here, the transmitted case (blue circle, $\Delta T = 2.5$, $\Delta k = 1.5$) leads to a slightly worse variance due to multiplexing than the received case (red circle, $\Delta T = 0.6$, $\Delta k = 7.822$). Additionally, longer pulses are less prone to uneven collisions due to lumped amplification, as the collision distance elongates.

To improve the transmission results, the phase-recovery algorithm was changed from a blind phase search to a pilot-based one. Besides the better phase-tracking, this also enabled the use of a Rx local oscillator with a larger line width, but 3 dB more power. This lead to an overall increase of the BERs, despite the denser multiplexing, due to higher SNR at the receiver, when compared to the previous measurements.

The results are depicted in Fig. 6.12b. Without equalization, a transmission reach of up to 5000 km remaining below the assumed SD-FEC limit could be reached. Overall, the MMSE equalizers could barely improve the BERs and lead to no significant gain. The NN, however, could improve the BER especially for the lower distance. This enabled the use of HD-FEC up to 5000 km.

Analysis of increased symbol-rates and reduced amount of samples

$\Delta t = 150$ ps, $\Delta f = 10$ GHz, $1.\overline{666}$ GBd, $13.\overline{333}$ Gb/s aggregated, 0.3333 b/s/Hz

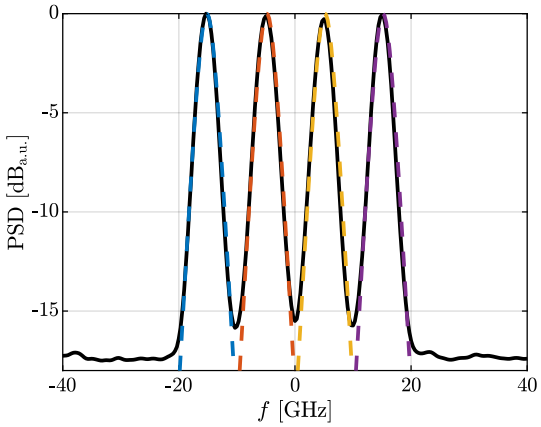

(a) (solid, black): Measured transmitted PSD, (dashed, colored): ideal PSDs of the four solitons to be multiplexed with $T_0 = 60\,\text{ps}$ for the second 4-channel settings.

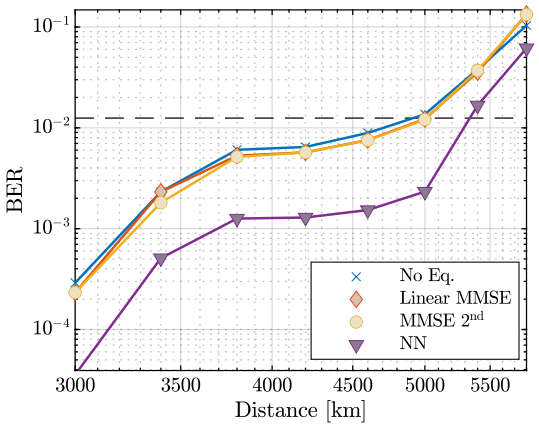

(b) BER depending on the transmission distance for four channel transmission using different equalizers. SD-FEC limit included for readability (dashed line).

Figure 6.12: Measurement results of the narrow multiplexing, four-channel experiments, showing the transmitted PSD and the BER.

To increase the spectral efficiency and especially the bit rate, the baud rate has now been changed. The spacing in the time domain remained at 150 ps. By using a symbol duration of 600 ps, an equidistant spacing of solitons of different windows in the time domain could be achieved. However, since the spacing in the time domain of the solitons within a block is not changed, a change in the achievable transmission distance can be attributed to the decreased sample count.

Again, the optimal launch power was swept at 3000 km before testing the transmission reach. And again, the launch power is below the calculated theoretical optimum, but increased by 2 dB, when compared to the 1 GBd measurement. This is because there is no more downtime between the soliton blocks. Therefore, the average signal power must increase by 2 dB to obtain the same peak power and hence T_0 as in the 1 GBd measurements.

The transmission reach with BERs below the assumed SD-FEC limit in this experiment was reduced by 400 km to 4600 km, when compared to the 1 GBd measurement, if no equalization was employed. This can be attributed to the reduced number of samples. On the other hand, the reduction of the transmission distance is relatively small here and may also indicate a measurement inaccuracy. Again, the MMSE equalizers could not improve upon this in a significant manner and the NN kept the BER below HD-FEC limit up to 4600 km. However, in these measurements, even at longer distances, the BER could be kept below SD-FEC with the help of the NN. Transmissions of up to 5800 km were possible.

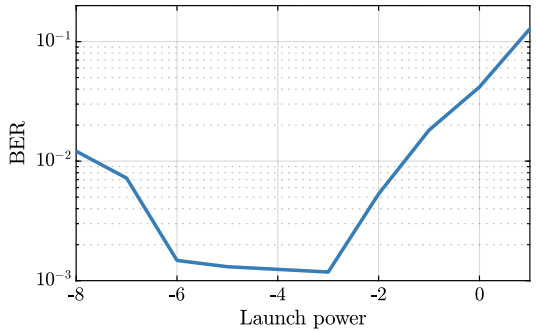

(a) BER depending on the launch power for dense four channel multiplexing at 3000 km transmission distance.

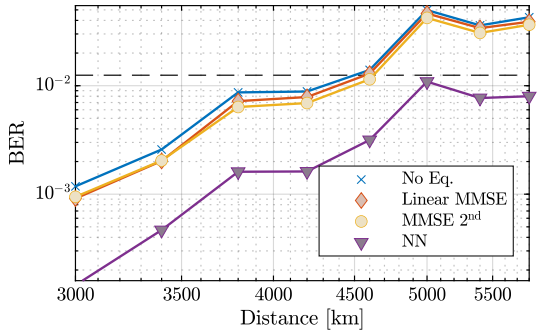

(b) BER depending on the transmission distance for four channel transmission using different equalizers. SD-FEC limit included for readability (dashed line).

Figure 6.13: Measurement results of the dense-multiplexing experiment with increased symbol-rate.

Analysis of additional Time-Division Modulation

$\Delta t = 150\,\text{ps}$, $\Delta f = 10\,\text{GHz}$, $1.\overline{666}\,\text{GBd}$, 2ASK-4PSK, 20 Gb/s aggregated, 0.5 b/s/Hz

To further increase the spectral efficiency, the amplitude of $b(\lambda_i)$ was chosen as the newly modulated degree of freedom. As previously described, solitons became temporally wider during transmission, which already increases temporal overlap. Combined with the design of the input filters (5 dB bandwidth = 10 GHz), this is why changing the solitons in the time domain was chosen to increase spectral efficiency. Since an even tighter multiplexing by increasing the symbol-rate was not possible due to the design of the delay lines, ASK modulation was chosen instead, which leads to a temporal shift of the solitons. Hence, some things have to be considered for this. First, the amplitudes should have the same value, but different signs on a logarithmic scale in order to equally distribute the resulting possible positions of the solitons in the time domain. The choice of amplitudes is now a trade-off between, on the one hand, the distinguishability between the amplitude levels in the noisy case and, on the other hand, the displacement of the solitons towards the edge of the window. A too large shift could allow for an easy decision, but pushes the solitons out of the time window and thus disturb the vanishing boundary condition. Furthermore, modulating the amplitude of $b(\lambda_i)$ also changes Δt, which in turn has an influence on the multiplexing penalty. Therefore, an optimal distribution of the amplitudes must be found.

To find appropriate amplitude levels, different time-shifts depending on the ASK modulation have been evaluated. The results are depicted in Fig. 6.14a. The overall best performance is gained by shifting the solitons by $\pm 90\,\text{ps}$. If this shift is chosen to be smaller, a penalty occurs over the whole transmission distance, which can be explained by the small distance between the points in the constellation. Larger

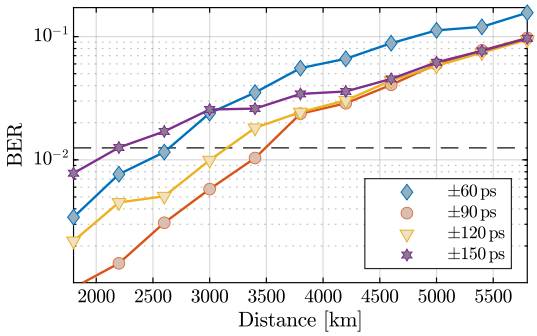

(a) BER for the four-channel transmission as a function of distance for different spectral amplitude modulations/time shifts.

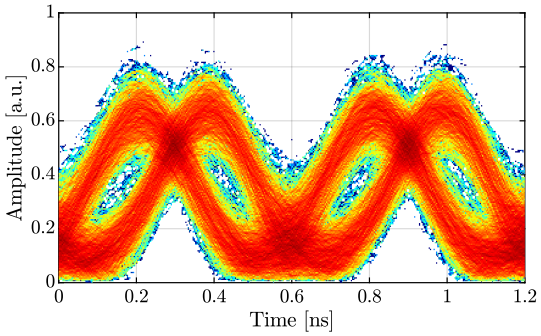

(b) Eye-diagram of one channel after 1800 km transmission with a time shift of ±90 ps.

Figure 6.14: Impact of different amplitude modulations on densely multiplexed four-channel transmission.

modulation time-shifts lead to a strong BER penalty especially at lower transmission distances, which is due to leaking of the solitons into the neighbouring time-windows. To illustrate the used time shift, Fig. 6.14b shows a received eye diagram after 1800 km transmission distance.

Without equalization, the additional modulation reduced the transmission range by about 1000 km to 3400 km when optimal spacing was selected. However, since it could be shown in previous chapters that the equalizers can reconstruct the amplitude very well, special attention has to be paid to this concept. Hence, after finding the optimal modulation time shift, the described equalizers were applied to the received NFT data. The results in Fig. 6.15a show that even the (non-linear) MMSE equalizers already allow a significant increase in performance. With the help of a linear MMSE equalizer, the transmission distance is extended up to 4200km and with a second-order non-linear MMSE equalizer up to 4600 km. The improvement in performance can also be observed qualitatively in Figs. 6.15b-6.15c. Here one can see how the non-linear MMSE equalizer can equalize the phases only minimally, but the amplitudes very well. Since only phase modulation was used in the previous measurements, the MMSE equalizers were not very effective.

Again, the NN equalizer performed the best in this experiment. It increased the transmission range below the SD-FEC limit by 2000 km to up to 5400 km, which is on par with the transmissions without amplitude modulation.

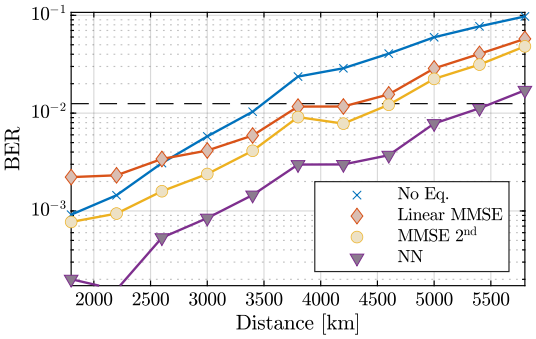

(a) BER for the four-channel transmission as a function of distance, without and with equalization (time shift ±90 ps).

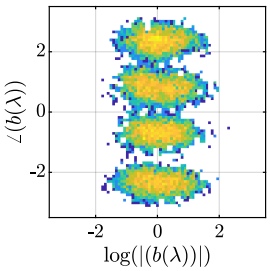

(b) Constellation diagram after 4600 km transmission without equalization.

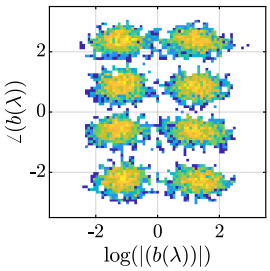

(c) Constellation diagram after 4600 km transmission with 2nd-order nonlinear MMSE equalization.

Figure 6.15: Equalization results of dense four-channel multiplexing transmission with additional amplitude modulation.

6.4 Summary

In this chapter, the possibility of multiplexing solitons linearly in very tight grids in both the time and frequency domains using a SiP chip was presented. This enables scalable, efficient soliton transmission. For a proof of concept, two chips were created, characterised and tested in transmission experiments. Thus, up to four soliton channels could be multiplexed and transmitted over long-haul distances.

To recap the experimental four-channel results, Fig. 6.16 depicts the transmission experiments. Here Fig. 6.16a shows the achievable transmission reach without equalization. Except for the first experiment, where the reach was particularly reduced by lower Rx LO power, the range at SD-FEC otherwise decreases with increasing spectral efficiency when no equalization is applied. Raising the baud rate from 1 GBd to 1.666 GBd (experiment 2 to 3) introduces only a small penalty (about 400 km at SD-FEC), which may still be within the range of measurement inaccuracy. By adding an ASK modulation, the range decreases more strongly with 800 km compared to the 3rd experiment. This is understandable, since a higher level modulation was applied at the same OSNR.

By applying an NN equalization, the measurement results can be strongly converged. Especially, if the HD-FEC limit is considered here, it can be seen that measurements 1, 3 and 4 with 4600 km have the same range and only measurement 2 with 5000 km reaches a slightly further distance, which is again within the range of measurement inaccuracy (Fig. 6.16b).

Fig. 6.17 shows the results of this work in comparison with other experiments based on NFT soliton transmissions. To do this, the spectral efficiencies and absolute data rates versus transmission distance from BERs to the SD-FEC limit are benchmarked. All efficiencies and bit rates are normalised to one

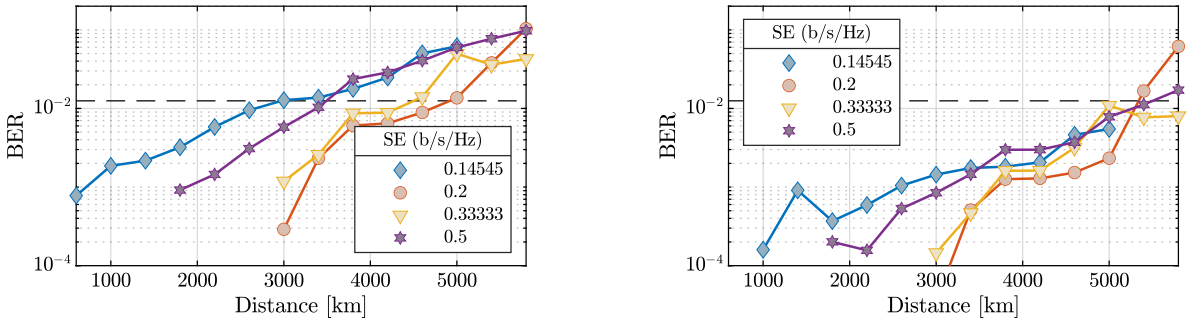

(a) BER without equalization.

(b) BER after NN equalization.

Figure 6.16: BER depending on distance for four-channel measurements. (blue, diamond): first settings, broad multiplexinig, (red, circle): second settings, dense multiplexing at 1 GBd, (yellow, triangle): third settings, dense multiplexing at $1.\overline{666}$ GBd, (purple, star): fourth settings, dense multiplexing at $1.\overline{666}$ GBd and additional ASK modulation. The legends denote the spectral efficiency. Assumed SD-FEC limit included for readability.

polarisation. In particular, the experiments of Gaiarin et al. and those of the collaboration with the Schäffer group at HSU were (as also shown in Chap. 5) dual polarisation transmissions, which doubles the absolute SE and bit rate, since an additional degree of freedom is used. This must be taken into account here. The experiments that were also described in this work (star and rectangle in the figure) are shown here once without equalization and once with NN equalization to ensure comparability with other works.

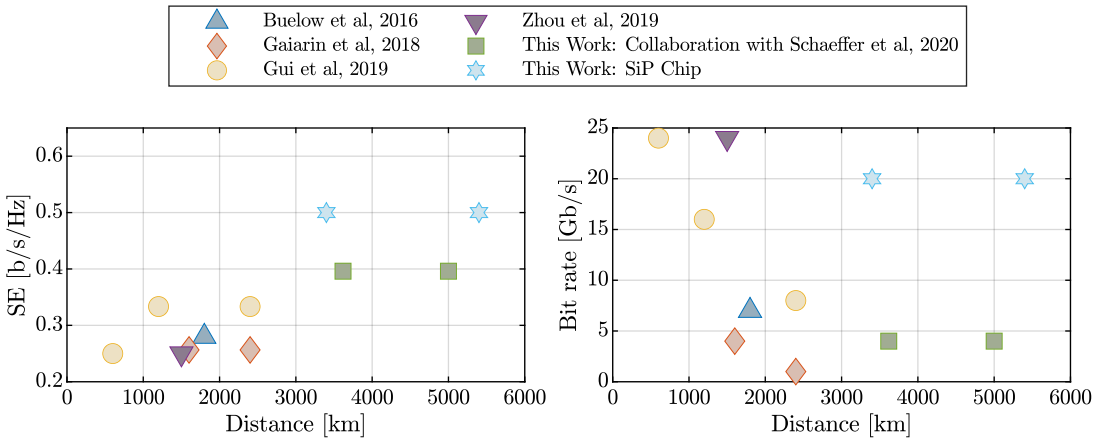

Figure 6.17: Comparison of the reached spectral efficiency (left) and bit rate (right) versus transmission distance at SD-FEC for selected experimental publications of NFT-based soliton transmissions. For comparison, these results are normalized to one polarization. Mind that Gaiarin et al (2018) and Schaeffer et al (2020) were dual-polarization experiments, which leads to a doubling of the spectral efficiency not displayed here. The referenced works are: Buelow et al [122], Gaiarin et al. [123], Gui et al. [82], Zhou et al. [124] and Collaboration with Schaeffer et al. [90]

The experiments presented here followed different approaches. Buelow et al [122] used digital multiplexing of a high number of seven eigenvalues with a relatively low symbol rate of 0.5 GBd and short 24 km spans of NZDSF. This is in contrast to the modulation scheme employed by Gui et al [82], which used only a single, highly modulated eigenvalue with symbol rates up to 6 GBd and 50 km NZDSF spans. Zhou et al [124] continued to work on the high symbol rate approach, but alternated the (non-zero) real-parts sign to force collisions during transmission, resulting in favorable soliton interactions. While this slightly decreased the spectral efficiency, the transmission distance increased. Gaiarin et al [123] focused on the first dual-polarization experiments using two vertically stacked eigenvalues at 1 GBd and distributed Raman amplification, albeit unfavourable 50 km SSMF links. Work on two polarizations has also been taken up by Schaeffer's group (Chan, Geisler et al) [86, 90]. Distributed Raman amplification was also used here, but it was employed on NZDSF-based transmission and horizontally distributed eigenvalues. This lead to very high spectral efficiencies.

As can be seen, comparably high data rates with not only high spectral efficiencies, but also over long distances are transmittable when a soliton dense wavelength division multiplexing (DWDM) transmission is used with the help of an SiP transmitter. The spectral efficiency could be doubled by using this transmission scheme, when compared to other works. This is in addition to increased transmission distances and possible scalability of this scheme. Using this approach, modulation of not only the phase, but also the amplitude can be used, since only one eigenvalue is processed at a time. This is combined with a high number of eigenvalues in relatively short time frames of only 600 ps. This raises the question what can be achieved, if several solitons are transmitted on the same frequency by stacking the eigenvalues vertically [125] or different polarizations are to be used, but also what can be done at the receiver side to aid very high-order soliton reception.

Chapter 7

Conclusions

In this chapter, a summary and conclusion of this thesis shall be drawn. Additionally, other current research topics about the NFT shall be mentioned.

7.1 Summary

In this work, the transmission of solitons in the framework of the nonlinear Fourier transform was investigated. Compared to the conventional Fourier transform, the nonlinear Fourier transform produces two spectra that propagate linearly through the nonlinear fiber-optic channel. As shown in this work, strongly nonlinear transmission is only possible using the discrete spectrum, i.e. solitons. This has sparked a new interest in soliton transmission. Even though the NFT promises linear transmission through a nonlinear channel, there are still many obstacles to overcome. In the field of NFT-based soliton transmission, these include equalization and the generation of spectrally efficient high-order solitons.

After first introducing solitons on a physical basis in the field of fiber-optic transmission systems, the NFT was briefly introduced. Solitons and soliton modulation in the framework of the NFT, as well as different methods of multiplexing solitons were presented. To fill large bandwidths with solitons, linear mutliplexing in the optical domain is necessary. The capabilities and limitations of linear multiplexing were demonstrated and compared with the nonlinear, digital Darboux method.

A photonic chip was designed to enable linear multiplexing taking into account constraints, which were established in the scope of this work. This chip allowed very precise control over the parameters of a soliton-based DWDM transmission. As a result, soliton transmissions using up to four channels with very high spectral efficiencies (0.5 b/s/Hz) and bit rates (20 Gb/s) over long distances of up to 5400 km could be achieved in experiments. One challenge was the high Tx noise floor due to the overall high

attenuations within the chip. With larger driving voltages of the MZMs, this effect could be reduced, but the achieved Tx SNR was still much lower than that of commercial modulators.

The results were supported by developing multiple equalization schemes in the nonlinear Fourier domain. The equalizers were based on the MMSE scheme and nonlinear extensions, similar to well-known Volterra equalizers. In addition, equalizers based on neural networks were developed and examined.

7.2 Conclusion

To test NFT equalizers, first-order single channel solitons with higher-order modulation (4ASK-8PSK) were transmitted experimentally. The results showed that the performance of the MMSE equalizers increased with rising nonlinear complexity. However, the performance improved only minimally by employing orders of nonlinearity larger than three. Hence, minding the exponentially increasing number of equalizer taps, using higher orders than the third was found out to not be optimum.

The equalizers were then tested using a dual-polarisation transmission scheme with second-order solitons. The two eigenvalues were QPSK modulated in both polarisations. Due to the low modulation order, the performance of the non-linear equalizers was only minimally improved compared to the linear equalizer. However, the non-linear equalizers were able to improve the performance by exploiting the cross-correlations between the eigenvalues, while the linear equalizer could not exploit these.

The neural networks showed very good results across the board. They performed best with one highly modulated eigenvalue as well as with two eigenvalues with lower order modulation when trained accordingly. Overall, the amount of needed training solitons was comparable to the requirements of nonlinear MMSE equalizers. Additionally, the hyper-parameters of the neural networks could be kept relatively constant (two layers were always sufficient), which enabled a fast implementation for different transmission scenarios.

The silicon PIC showed promising results with regards to spectral efficiencies and bit rates. However, multiple issues were identified which need more in-depth research or revisions of the PIC as discussed below. It has been shown that the solitons did not completely maintain their shape during transmission, but tended to widen when all four channels were used and multiplexed densely in frequency domain. This resulted in lower optimal transmission powers as expected from theory. In general, the solitons were more stable in experimental transmissions. One reason for this could be collision effects resulting from lumped amplification. To increase the collision distance, denser multiplexing in the frequency domain with temporally wider solitons is one option. This would keep the spectral efficiency constant. However, this was not possible due to input filters in the chip that were designed to be too large. Denser

multiplexing hence lead to energy shifts into the neighboring channels. This was an oversight in the design phase of the chip, which could be revised in a new tape out.

An additional limitation was the number of electrical amplifiers used on the transmitting side. With additional amplifiers, a 6 dB increase in output power could have been achieved, as calculated and shown in experiments with only two channels. However, the power had to be divided since only four amplifiers of the same type were present. In retrospect, additional amplifiers could possibly have been used. This was not done initially, as it would have entailed a different amplification of the comb laser lines. However, since four different lasers were ultimately used, they could have been adjusted according to the used amplifiers, resulting in an overall increased output power.

Still one of the biggest bottlenecks of soliton transmission, despite tight multiplexing to increase spectral efficiencies, is the conventional lumped amplification scheme or rather non-constant ratio of dispersion and nonlinearities. Constant power within the fiber spans with the help of Raman amplifiers could enable very broadband soliton systems in particular and remains an issue to be investigated in greater depth.

On the NFT processing side, receiving two channels and calculating the NFT of a higher order soliton was generally inferior to receiving and processing first order solitons only. This reduced the efficiency of downstream equalizers, since possible cross-correlation effects could not be considered.

7.3 Outlook

In order to use all degrees of freedom of the NFT, the continuous spectrum must be used in addition to the second polarisation, which is not further discussed here. It is possible, for example, to modulate the NFT spectrum with the result of a common Fourier transform of a modulated time-domain signal or with OFDM signals. This is referred to as NFDM in the literature and can drastically increase spectral efficiencies compared to conventional soliton transmissions. For example, so far spectral efficiencies of up to 7.2 b/s/Hz (in simulations [126]) and 4 b/s/Hz (in experiment [127]) can be achieved if only the continuous spectrum is used, which can be further increased by using the discrete spectrum. The problem, however, is that too much power in the continuous spectrum can lead to very long tails in the time domain, which can slow down the baud rate considerably. To get around this, pure b-modulation has to be used. If a signal generated by an IFFT is time limited, a signal generated by a b-modulated INFT is also time limited [63][128]. However, the maximum power is limited because $|b(\lambda)|$ must not be greater than 1 in order to calculate $a(\lambda)$ and consequently $q_c(\lambda)$[129]. Thus it is not possible to perform transmissions in the strongly nonlinear regime with a correct normalization.
Thus, to move the overall power of the signal into the non-linear regime, solitons must be considered. With a high number of solitons, however, this can lead to numerical problems as well as problems in the

digital-to-analog and electrical to optical conversion, as has already been discussed in this thesis [54].

Another way to use the NFT is a one-step digital back-propagation (DBP) in the receiver. By calculating an NFT of any signal in the receiver, linearly back-propagating it and then calculating an INFT, the computational effort can be reduced compared to a conventional DBP based on the split-step Fourier method (SSFM) with the same performance [130]. However, in order to be able to use very high powers here as well, the discrete eigenvalues of the NFT spectrum must urgently be taken into account. As already shown in Chapter 3.4 (Fig. 3.7), solitons already account for a large part of the signal energy at relatively low transmission powers as soon as a somewhat longer signal is considered. Thus, it is necessary to calculate all discrete eigenvalues very precisely, which can greatly increase the computational effort of an NFT. This can negate the advantage of a one-step DBP, which is why SSFM DBPs can again gain the upper hand here.

However, all of the above transmission systems also require a non-linear WDM solution to a) account for all XPM effects between channels at the receiver and b) enable routing. As already shown in Fig. 6.1, linear de-/multiplexing and a subsequent non-linear calculation by e.g. the NFT does not lead to the correct result. In order to be able to take broadband XPM effects between channels into account, very broadband receivers must be developed that can process several channels at once. One solution could be a stitching receiver [131], where multiple laser lines of a comb source drive multiple coherent receivers and thus detect a very broad band. Due to the constant spacing between the received spectral slices, a linear addition leads to an equivalent broad band receivers output. This could enable NFT processing of multiple channels and hence the linearization of XPM effects.

A completely different approach to making use of the transmission properties of NFT is the estimation of nonlinear fiber parameters. If non-linearities are to be compensated for in the future, by whatever means, a precise knowledge of the non-linearity of the fiber is advantageous. To measure this, the knowledge of the positions of the discrete eigenvalues at the transmitting end can be used to determine the mean nonlinear coefficient of the transmission path at the receiving end [22][132][133]. To do this, the dispersion is first determined, which is a trivial task. Then, on the receiver side, the ratio of the dispersion parameter and the non-linear parameter γ is swept in the normalization step. Only with correct normalization are the received eigenvalues at the same position as at the transmitter. In this way, the non-linear parameter can be determined. A great advantage compared to other methods such as estimation using the SSFM is the independence of the phase and very precise synchronisation, as these have no influence on the eigenvalue positions. Furthermore, in the case of an NFDM transmission with known discrete eigenvalues, this process could take place online and with an information bearing signal. This can ensure

permanent, parallel monitoring of the links' nonlinearities, which might change due to power fluctuations.

List of Figures

List of Tables

Acronyms

ADC analog-to-digital converter

APSK amplitude phase-shift keying

AWG arbitrary waveform generator

BER bit error rate

CAGR compound annual growth rates

CLP continuous layer-peeling

CROW coupled (ring-) resonator optical waveguide

CW continuous wave

DAC digital-to-analog converter

DCF dispersion compensating fiber

DD direct detection

DSF dispersion shifted fiber

DSP digital signal processing

DWDM dense wavelength division multiplexing

EDF Erbium-doped fiber

EDFA Erbium-doped fiber amplifier

FFE feed forward equalizer

FFT fast Fourier transformation

FWHM full width at half maximum

FWM four-wave mixing

GLME Gelfand-Levitan-Marchenko integral equations

HD-FEC hard-decision forward error correction

IL insertion loss

INFT inverse nonlinear Fourier transformation

IST inverse scattering transform

KdV Korteweg-de Vries

LO local-oscillator

ML machine learning

MMI multi-mode interference coupler

MMSE minimum mean squared error

MSE mean squared error

MTBF manually tunable bandpass filter

MZI Mach-Zehnder interferometer

MZM Mach-Zehnder modulator

NFC nonlinear Fourier coefficient

NN neural network

NFT nonlinear Fourier transform

NLSE nonlinear Schrödinger equation

NZDSF non-zero dispersion shifted fiber

OADM optical add-drop multiplexers

OOK on-off keying

OSA optical spectrum analyzer

OSNR optical signal-to-noise ratio

PAPR peak-to-average power ratio

PIC photonic integrated circuit

PD photo-diode

PSD power spectral density

QoT quality of transmission

Rx receiver

SD-FEC soft-decision forward error correction

SDM space-division multiplexing

SiP silicon photonics

SNR signal-to-noise ratio

SPM self-phase modulateion

SSMF standard single-mode fiber

SSR solitonic-signal-ratio

TIB Toeplitz inner bordering

Tx transmitter

WS WaveShaper 4000S

WDM wavelength division multiplexing

XPM cross-phase modulation

ZSP Zakharov-Shabat problem

Bibliography

[1] K. C. Kao and G. A. Hockham, "Dielectric-fibre surface waveguides for optical frequencies," *Proceedings of the Institution of Electrical Engineers*, vol. 113, no. 7, pp. 1151–1158, 1966. [Online]. Available: http://dx.doi.org/10.1049/piee.1966.0189

[2] S. Pachnicke, "Lecture notes optical communications," Kiel, 2021.

[3] P. J. Winzer, D. T. Neilson, and A. R. Chraplyvy, "Fiber-optic transmission and networking: The previous 20 and the next 20 years [invited]," *Optics Express*, vol. 26, no. 18, p. 24190, 2018.

[4] Cisco, "Cisco visual networking index: forecast and trends, 2017-2022." [Online]. Available: https://www.ieee802.org/3/ad_hoc/bwa2/public/calls/19_0624/nowell_bwa_01_190624.pdf

[5] R.-J. Essiambre and R. W. Tkach, "Capacity trends and limits of optical communication networks," *Proceedings of the IEEE*, vol. 100, no. 5, pp. 1035–1055, 2012. [Online]. Available: http://dx.doi.org/10.1109/jproc.2012.2182970

[6] DE-CIX Management GmbH, "Frankfurt traffic statisctics." [Online]. Available: https://www.de-cix.net/en/locations/frankfurt/statistics

[7] P. J. Winzer and D. T. Neilson, "From scaling disparities to integrated parallelism: A decathlon for a decade," *Journal of Lightwave Technology*, vol. 35, no. 5, pp. 1099–1115, 2017. [Online]. Available: http://dx.doi.org/10.1109/jlt.2017.2662082

[8] van Uden, R. G. H., R. A. Correa, E. A. Lopez, F. M. Huijskens, C. Xia, G. Li, A. Schülzgen, H. de Waardt, A. M. J. Koonen, and C. M. Okonkwo, "Ultra-high-density spatial division multiplexing with a few-mode multicore fibre," *Nature Photonics*, vol. 8, no. 11, pp. 865–870, 2014. [Online]. Available: https://www.nature.com/articles/nphoton.2014.243

[9] René-Jean Essiambre, Gerhard Kramer, Peter J. Winzer, Gerard J. Foschini, and Bernhard Goebel, "Capacity limits of optical fiber networks," *Journal of Lightwave Technology*, vol. 28, no. 4, pp. 662–701, 2010. [Online]. Available: https://www.researchgate.net/profile/rene-jean-essiambre/publication/224118421_capacity_limits_of_optical_fiber_networks

[10] M. I. Yousefi and F. R. Kschischang, "Information transmission using the nonlinear fourier transform, part i: Mathematical tools," *IEEE Transactions on Information Theory*, vol. 60, no. 7, pp. 4312–4328, 2014.

[11] S. K. Turitsyn, J. E. Prilepsky, S. T. Le, S. Wahls, L. L. Frumin, M. Kamalian, and S. A. Derevyanko, "Nonlinear fourier transform for optical data processing and transmission: Advances and perspectives," *Optica*, vol. 4, no. 3, p. 307, 2017.

[12] Egor V. Sedov, Alexey A. Redyuk, Mikhail P. Fedoruk, Andrey A. Gelash, Leonid L. Frumin, and Sergey K. Turitsyn, "Soliton content in the standard optical ofdm signal," *Optics Letters*, vol. 43, no. 24, pp. 5985–5988, 2018.

[13] G. P. Agrawal, *Fiber-optic communication systems with cd*, 4th ed., ser. Wiley series in microwave and optical engineering. New York: Wiley, 2010, vol. 222.

[14] R. Engelbrecht, *Nichtlineare Faseroptik: Grundlagen und Anwendungsbeispiele.* Berlin: Springer Vieweg, 2014. [Online]. Available: http://dx.doi.org/10.1007/978-3-642-40968-4

[15] A. Hasegawa, "Soliton-based optical communications: An overview," *IEEE Journal of Selected Topics in Quantum Electronics*, vol. 6, no. 6, pp. 1161–1172, 2000. [Online]. Available: http://dx.doi.org/10.1109/2944.902164

[16] L. F. Mollenauer, S. G. Evangelides, and J. P. Gordon, "Wavelength division multiplexing with solitons in ultra-long distance transmission using lumped amplifiers," *Journal of Lightwave Technology*, vol. 9, no. 3, pp. 362–367, 1991. [Online]. Available: http://dx.doi.org/10.1109/50.70013

[17] L. F. Mollenauer, P. V. Mamyshev, and M. J. Neubelt, "Demonstration of soliton wdm transmission at up to 8 × 10 gbit/s, error-free over transoceanic distances," *Optical Fiber Communication Conference*, p. PD22, 1996. [Online]. Available: https://www.osapublishing.org/viewmedia.cfm?id=114382&seq=0

[18] S. Pachnicke, *Fiber-optic transmission networks: Efficient design and dynamic operation*, ser. Signals and communication technology. Heidelberg: Springer, 2012.

[19] J. Koch, A. Moscoso-Mártir, J. Müller, A. Tabatabaei Mashayekh, A. D. Das, F. Merget, S. Pachnicke, and J. Witzens, "Experimental demonstration of a silicon-photonics wdm nft soliton transmitter," *Optical Fiber Communication Conference*, p. W6A.34, 2021.

[20] A. Moscoso-Martir, J. Koch, J. Muller, A. Tabatabaei Mashayekh, A. D. Das, F. Merget, S. Pachnicke, and J. Witzens, "Silicon photonics integrated circuits for nonlinear fourier transform based transmission," in *2021 European Conference on Optical Communication (ECOC)*, 2021.

[21] Pascal De Koster, Jonas Koch, Olaf Schulz, Stephan Pachnicke, and Sander Wahls, "Experimental validation of nonlinear fourier transform-based kerr-nonlinearity identification over a 1600 km ssmf link," 2022.

[22] P. de Koster, J. Koch, S. Pachnicke, and S. Wahls, "Experimental investigation of nonlinear fourier transform based fibre nonlinearity characterisation," in *2021 European Conference on Optical Communication (ECOC)*, 2021.

[23] Simon Ohlendorf, "Experimental demonstration of flexible modulation formats for optical data center interconnects," Dissertation, Kiel University, Kiel, 2021.

[24] Keysight, "M8196a 92 gsa/s arbitrary waveform generators." [Online]. Available: https://www.keysight.com/de/de/product/M8196A/92-gsa-s-arbitrary-waveform-generators.html

[25] S. Ohlendorf, R. Joy, S. Pachnicke, and W. Rosenkranz, "Flexible pam in dwdm transmission with kramers-kronig dsp," in *44th European Conference on Optical Communication (ECOC)*, 2018.

[26] Antonio Mecozzi, Cristian Antonelli, and Mark Shtaif, "Kramers–kronig receivers," *Advances in Optics and Photonics*, vol. 11, no. 3, pp. 480–517, 2019.

[27] M. J. Deen and S. Kumar, *Fiber optic communications: Fundamentals and applications / Shiva Kumar and M. Jamal Deen, Department of Electrical and Computer Engineering, McMaster University, Canada*, [new edition] ed. Chichester, West Sussex, United Kingdom: Wiley, 2014.

[28] Donald R. Zimmerman and Leo H. Spiekman, "Amplifiers for the masses:edfa, edwa, and soa amplets for metro and access applications," *Journal of Lightwave Technology*, vol. 22, no. 1, p. 63, 2004.

[29] B. J. Ainslie, "A review of the fabrication and properties of erbium-doped fibers for optical amplifiers," *Journal of Lightwave Technology*, vol. 9, no. 2, pp. 220–227, 1991. [Online]. Available: http://dx.doi.org/10.1109/50.65880

[30] G. P. Agrawal, *Nonlinear fiber optics*, 3rd ed., ser. Optics and photonics. San Diego: Academic Press, 2001.

[31] J. Schroder, M. A. F. Roelens, L. B. Du, A. J. Lowery, and B. J. Eggleton, "Lcos based waveshaper technology for optical signal processing and performance monitoring," in *17th Opto-Electronics and Communications Conference*, 2012.

[32] II-VI Incorporated, "Waveshaper: Series a family of programmable optical processors." [Online]. Available: https://ii-vi.com/product/waveshaper-1000a-programmable-optical-filter/

[33] EXFO, "Xta-50: Tunable filter with adjustable bandwidth." [Online]. Available: https://www.exfo.com/umbraco/surface/file/download/?ni=17922&cn=en-US&pi=17923

[34] M. J. Ablowitz and H. Segur, *Solitons and the Inverse Scattering Transform*. Society for Industrial and Applied Mathematics, 1981.

[35] D. J. Korteweg and G. de Vries, "Xli. on the change of form of long waves advancing in a rectangular canal, and on a new type of long stationary waves," *The London, Edinburgh, and Dublin Philosophical Magazine and Journal of Science*, vol. 39, no. 240, pp. 422–443, 1895. [Online]. Available: http://dx.doi.org/10.1080/14786449508620739

[36] N. J. Zabusky and M. D. Kruskal, "Interaction of "solitons" in a collisionless plasma and the recurrence of initial states," *Physical Review Letters*, vol. 15, no. 6, pp. 240–243, 1965. [Online]. Available: http://dx.doi.org/10.1103/physrevlett.15.240

[37] C. S. Gardner, J. M. Greene, M. D. Kruskal, and R. M. Miura, "Method for solving the korteweg-devries equation," *Physical Review Letters*, vol. 19, no. 19, pp. 1095–1097, 1967. [Online]. Available: http://dx.doi.org/10.1103/physrevlett.19.1095

[38] P. D. Lax, "Integrals of nonlinear equations of evolution and solitary waves," *Communications on Pure and Applied Mathematics*, vol. 21, no. 5, pp. 467–490, 1968. [Online]. Available: http://dx.doi.org/10.1002/cpa.3160210503

[39] V. E. Zakharov and A. B. Shabat, "Exact theory of two-dimensional self-focusing and one-dimensional self-modulation of waves in nonlinear medi," *Soviet J. Exp. Theory Phys. (JETP)*, vol. 34, no. 1, pp. 62–69, 1972.

[40] M. J. Ablowitz, D. J. Kaup, A. C. Newell, and H. Segur, "Nonlinear-evolution equations of physical significance," *Physical Review Letters*, vol. 31, no. 2, pp. 125–127, 1973. [Online]. Available: http://dx.doi.org/10.1103/physrevlett.31.125

[41] Mark J. Ablowitz, David J. Kaup, Alan C. Newell, and Harvey Segur, "The inverse scattering transform-fourier analysis for nonlinear problems," *Studies in Applied Mathematics*, vol. 53, no. 4, pp. 249–315, 1974.

[42] Akira Hasegawa and Frederick Tappert, "Transmission of stationary nonlinear optical pulses in dispersive dielectric fibers. i. anomalous dispersion," *Applied Physics Letters*, vol. 23, no. 3, p. 142, 2003.

[43] S. K. Turitsyn, J. E. Prilepsky, S. T. Le, S. Wahls, L. L. Frumin, M. Kamalian, and S. A. Derevyanko, "Nonlinear fourier transform for optical data processing and transmission: Advances and perspectives: supplementary material," *Optica*, vol. 4, no. 3, p. 307, 2017.

[44] M. I. Yousefi and F. R. Kschischang, "Information transmission using the nonlinear fourier transform, part iii: Spectrum modulation," *IEEE Transactions on Information Theory*, vol. 60, no. 7, pp. 4346–4369, 2014.

[45] Morteza Kamalian, Anastasiia Vasylchenkova, Dmitry Shepelsky, Jaroslaw E. Prilepsky, and Sergei K. Turitsyn, "Signal modulation and processing in nonlinear fibre channels by employing the riemann–hilbert problem," *Journal of Lightwave Technology*, vol. 36, no. 24, pp. 5714–5727, 2018.

[46] Morteza Kamalian-Kopae, Anastasiia Vasylchenkova, Dmitry Shepelsky, Jaroslaw E. Prilepsky, and Sergei K. Turitsyn, "Full-spectrum periodic nonlinear fourier transform optical communication through solving the riemann-hilbert problem," *Journal of Lightwave Technology*, vol. 38, no. 14, pp. 3602–3615, 2020.

[47] M. I. Yousefi and F. R. Kschischang, "Information transmission using the nonlinear fourier transform, part ii: Numerical methods," *IEEE Transactions on Information Theory*, vol. 60, no. 7, pp. 4329–4345, 2014.

[48] M. Yousefi and X. Yangzhang, "Linear and nonlinear frequency-division multiplexing," *IEEE Transactions on Information Theory*, vol. 66, no. 1, pp. 478–495, 2020. [Online]. Available: http://dx.doi.org/10.1109/tit.2019.2941479

[49] V. Aref, *Control and Detection of Discrete Spectral Amplitudes in Nonlinear Fourier Spectrum*, 2016.

[50] S. Hari and F. R. Kschischang, "Bi-directional algorithm for computing discrete spectral amplitudes in the nft," *Journal of Lightwave Technology*, vol. 34, no. 15, pp. 3529–3537, 2016. [Online]. Available: http://dx.doi.org/10.1109/jlt.2016.2577702

[51] Leonid L. Frumin, Oleg V. Belai, Eugeny V. Podivilov, and David A. Shapiro, "Efficient numerical method for solving the direct zakharov–shabat scattering problem," *J. Opt. Soc. America B*, vol. 32, no. 2, pp. 290–296, 2015.

[52] Mansoor Isvand Yousefi and Xianhe Yangzhang, "Nonlinear frequency-division multiplexing," *IEEE Transactions on Information Theory*, vol. PP, no. 99, 2016. [Online]. Available: https://www.researchgate.net/profile/mansoor-isvand-yousefi/publication/298790559_nonlinear_frequency-division_multiplexing

[53] S. Wahls and H. V. Poor, "Fast inverse nonlinear fourier transform for generating multi-solitons in optical fiber," in *IEEE International Symposium on Information Theory (ISIT)*. IEEE, 2015.

[54] V. Aref, S. T. Le, and H. Buelow, "Modulation over nonlinear fourier spectrum: Continuous and discrete spectrum," *Journal of Lightwave Technology*, vol. 36, no. 6, pp. 1289–1295, 2018. [Online]. Available: http://dx.doi.org/10.1109/jlt.2018.2794475

[55] S. Wahls and H. V. Poor, "Introducing the fast nonlinear fourier transform," in *IEEE International Conference on Acoustics, Speech and Signal Processing*, 2013.

[56] ——, "Fast numerical nonlinear fourier transforms," *IEEE Transactions on Information Theory*, vol. 61, no. 12, pp. 6957–6974, 2015. [Online]. Available: http://dx.doi.org/10.1109/tit.2015.2485944

[57] S. Chimmalgi, P. J. Prins, and S. Wahls, "Fast nonlinear fourier transform algorithms using higher order exponential integrators," *IEEE Access*, vol. 7, pp. 145 161–145 176, 2019. [Online]. Available: http://dx.doi.org/10.1109/access.2019.2945480

[58] S. Medvedev, I. Vaseva, I. Chekhovskoy, and M. Fedoruk, "Exponential fourth order schemes for direct zakharov-shabat problem," *Optics Express*, vol. 28, no. 1, p. 20, 2020.

[59] Sergey Medvedev, Igor Chekhovskoy, Irina Vaseva, and Mikhail Fedoruk, "Conservative multi-exponential scheme for solving the direct zakharov–shabat scattering problem," *Optics Letters*, vol. 45, no. 7, pp. 2082–2085, 2020.

[60] V. Vaibhav and S. Wahls, "Introducing the fast inverse nft," in *Optical Fiber Communication Conference (OFC)*. OSA, 2017.

[61] S. Wahls, S. T. Le, J. E. Prilepsk, H. V. Poor, and S. K. Turitsyn, "Digital backpropagation in the nonlinear fourier domain," in *16th International Workshop on Signal Processing Advances in Wireless Communications (SPAWC)*, 2015.

[62] Leonid L. Frumin, Oleg V. Belai, Eugeny V. Podivilov, and David A. Shapiro, "Efficient numerical method for solving the direct zakharov–shabat scattering problem," *J. Opt. Soc. America B*, vol. 32, no. 2, pp. 290–296, 2015.

[63] S. Wahls, "Generation of time-limited signals in the nonlinear fourier domain via b-modulation," in *43rd European Conference on Optical Communication (ECOC)*, 2017.

[64] J. P. Gordon and H. A. Haus, "Random walk of coherently amplified solitons in optical fiber transmission," *Optics Letters*, vol. 11, no. 10, pp. 665–667, 1986.

[65] J. P. Gordon, "Theory of the soliton self-frequency shift," *Optics Letters*, vol. 11, no. 10, pp. 662–664, 1986.

[66] Akira Hasegawa, Shiva Kumar, and Yuji Kodama, "Reduction of collision-induced time jitters in dispersion-managed soliton transmission systems," *Optics Letters*, vol. 21, no. 1, pp. 39–41, 1996.

[67] M. Zitelli, F. Favre, D. Le Guen, and S. Del Burgo, "Numerical and experimental investigation of power and wavelength margins for a 20-gb/s dispersion-managed soliton transmission system on standard fiber," *IEEE Photonics Technology Letters*, vol. 11, no. 7, pp. 904–906, 1999. [Online]. Available: http://dx.doi.org/10.1109/68.769747

[68] L. F. Mollenauer, P. V. Mamyshev, J. Gripp, M. J. Neubelt, N. Mamysheva, Lars Grüner-Nielsen, and Torben Veng, "Demonstration of massive wavelength-division multiplexing over transoceanic distances by use of dispersion-managed solitons," *Optics Letters*, vol. 25, no. 10, pp. 704–706, 2000.

[69] Masataka Nakazawa, Hirokazu Kubota, Kazunori Suzuki, Eiichi Yamada, and Akio Sahara, "Recent progress in soliton transmission technology," *Chaos: An Interdisciplinary Journal of Nonlinear Science*, vol. 10, no. 3, p. 486, 2000.

[70] D. Le Guen, S. Del Burgo, M. L. Moulinard, D. Grot, M. Henry, F. Favre, and T. Georges, "Narrow band 1.02 tbit/s (51×20 gbit/s) soliton dwdm transmission over 1000 km of standard fiber with 100 km amplifier spans," *Optical Fiber Communication Conference*, p. PD4, 1999.

[71] V. Bajaj, S. Chimmalgi, V. Aref, and S. Wahls, "Exact nonlinear frequency division multiplexing in lossy fibers," in *45th European Conference on Optical Communication (ECOC)*, 2019.

[72] Vinod Bajaj, Shrinivas Chimmalgi, Vahid Aref, and Sander Wahls, "Exact nfdm transmission in the presence of fiber-loss," *Journal of Lightwave Technology*, vol. 38, no. 11, pp. 3051–3058, 2020.

[73] A. Hasegawa and T. Nyu, "Eigenvalue communication," *Journal of Lightwave Technology*, vol. 11, no. 3, pp. 395–399, 1993. [Online]. Available: http://dx.doi.org/10.1109/50.219570

[74] H. Terauchi and A. Maruta, "Eigenvalue modulated optical transmission system based on digital coherent technology," in *18th OptoElectronics and Communications Conference held jointly with 2013 International Conference on Photonics in Switching*. OSA, 2013.

[75] S. Hari, F. Kschischang, and M. Yousefi, "Multi-eigenvalue communication via the nonlinear fourier transform," in *27th Biennial Symposium on Communications (QBSC)*, 2014.

[76] S. Hari, M. I. Yousefi, and F. R. Kschischang, "Multieigenvalue communication," *Journal of Lightwave Technology*, vol. 34, no. 13, pp. 3110–3117, 2016. [Online]. Available: http://dx.doi.org/10.1109/jlt.2016.2551638

[77] H. Bulow, "Experimental demonstration of optical signal detection using nonlinear fourier transform," *Journal of Lightwave Technology*, vol. 33, no. 7, pp. 1433–1439, 2015. [Online]. Available: http://dx.doi.org/10.1109/jlt.2015.2399014

[78] V. Aref, H. Bulow, K. Schuh, and W. Idler, "Experimental demonstration of nonlinear frequency division multiplexed transmission," in *41st European Conference on Optical Communication (ECOC)*, 2015.

[79] A. Geisler, C. G. Schaeffer, "Experimental nonlinear frequency division multiplexed transmission using eigenvalues with symmetric real part," in *42nd European Conference on Optical Communication (ECOC)*, 2016.

[80] A. Geisler, C. G. Schaeffer, Ed., *Influence of input power mismatch on time domain detection of solitonic components: Beiträge der, 2017, Hochschule für Telekommunikation*, ser. ITG-Fachbericht, vol. 272. Berlin: VDE Verlag GmbH, 2017.

[81] T. Gui, T. H. Chan, C. Lu, A. P. T. Lau, and P.-K. A. Wai, "Alternative decoding methods for optical communications based on nonlinear fourier transform," *Journal of Lightwave Technology*, vol. 35, no. 9, pp. 1542–1550, 2017. [Online]. Available: http://dx.doi.org/10.1109/jlt.2017.2654493

[82] Tao Gui, Chao Lu, Alan Pak Tao Lau, and P. K. A. Wai, "High-order modulation on a single discrete eigenvalue for optical communications based on nonlinear fourier transform," *Optics Express*, vol. 25, no. 17, pp. 20 286–20 297, 2017.

[83] A. Maruta and Y. Matsuda, "Polarization division multiplexed optical eigenvalue modulation," in *International Conference on Photonics in Switching (PS)*, 2015.

[84] S. Gaiarin, A. M. Perego, E. P. da Silva, F. Da Ros, and D. Zibar, "Dual-polarization nonlinear fourier transform-based optical communication system," *Optica*, vol. 5, no. 3, pp. 263–270, 2018.

[85] A. Span, V. Aref, H. Bulow, and S. ten Brink, "Efficient precoding scheme for dual-polarization multi-soliton spectral amplitude modulation," *IEEE Transactions on Communications*, vol. 67, no. 11, pp. 7604–7615, 2019. [Online]. Available: http://dx.doi.org/10.1109/tcomm.2019.2935716

[86] K. Chan, A. Geisler, J. Leibrich, and C. G. Schaeffer, "Experimental demonstration of differential coding gain for dual polarization two-eigenvalue signals," *IEEE Photonics Technology Letters*, vol. 31, no. 24, pp. 1913–1916, 2019.

[87] J. Koch, R. Weixer, and S. Pachnicke, "Equalization of soliton transmission based on nonlinear fourier transform using neural networks," in *45th European Conference on Optical Communication (ECOC)*, 2019.

[88] K. Chan, J. Leibrich, A. Geisler, and C.G. Schaeffer, "Joint detection equalization on nonlinear fourier transform based optical communication," in *45th European Conference on Optical Communication (ECOC)*, 2019.

[89] Ken Mishina, Shingo Sato, Shohei Yamamoto, Yuki Yoshida, Daisuke Hisano, and Akihiro Maruta, "Demodulation of eigenvalue modulated signal based on eigenvalue-domain neural network," *Optical Fiber Communication Conference*, p. W3D.1, 2020.

[90] J. Koch, K. Chan, C. G. Schaeffer, and S. Pachnicke, "Signal processing techniques for optical transmission based on eigenvalue communication," *IEEE Journal of Selected Topics in Quantum Electronics*, vol. 27, no. 3, 2020.

[91] A. Span, V. Aref, H. Bulow, and S. ten Brink, "On time-bandwidth product of multi-soliton pulses," in *2017 IEEE International Symposium on Information Theory (ISIT)*, 2017.

[92] S. Li, J. Koch, and S. Pachnicke, "Optical signal processing in the discrete nonlinear frequency domain," in *Optical Fiber Communication Conference (OFC)*, 2018.

[93] J. Koch, S. Li, and S. Pachnicke, "Transmission of higher order solitons created by optical multiplexing," *Journal of Lightwave Technology*, vol. 37, no. 3, pp. 933–941, 2019. [Online]. Available: http://dx.doi.org/10.1109/jlt.2018.2883826

[94] G. Weerasekara and A. Maruta, "Eigenvalue based analysis of soliton fusion phenomenon in the frame work of nonlinear schrödinger equation," *IEEE Photonics Journal*, vol. 9, no. 3, pp. 1–12, 2017. [Online]. Available: http://dx.doi.org/10.1109/jphot.2017.2697902

[95] Morteza Kamalian, Jaroslaw E. Prilepsky, Son T. Le, and Sergei K. Turitsyn, "On the design of nft-based communication systems with lumped amplification," *Journal of Lightwave Technology*, vol. 35, no. 24, pp. 5464–5472, 2017.

[96] D.J. Kaup, "A perturbation expansion for the zakharov–shabat inverse scattering transform," *SIAM Journal on Applied Mathematics*, vol. 31, no. 1, pp. 121–133, 1976.

[97] Y. S. Kivshar and B. A. Malomed, "Dynamics of solitons in nearly integrable systems," *Reviews of Modern Physics*, vol. 61, no. 4, pp. 763–915, 1989. [Online]. Available: http://dx.doi.org/10.1103/revmodphys.61.763

[98] E. Meron, M. Feder, and M. Shtaif, "On the achievable communication rates of generalized soliton transmission systems," in *arXiv:1207.0297 [cs.IT]*.

[99] F. J. Garcia-Gomez and V. Aref, "Statistics of the nonlinear discrete spectrum of a noisy pulse," *Journal of Lightwave Technology*, vol. 37, no. 14, pp. 3563–3570, 2019. [Online]. Available: http://dx.doi.org/10.1109/jlt.2019.2917996

[100] M. Pankratova, A. Vasylchenkova, and J. E. Prilepsky, "Noise-induced signal corruption in nonlinear fourier-based optical transmission system in the presence of discrete eigenvalues," *The International Conference on Optical Communication Systems*, 2019.

[101] G. Zhou, *Digital signal processing in nonlinear frequency division multiplexing systems.* Hong Kong Polytechnic University, 2021.

[102] J. Koch, K. Chan, S. Kuhl, C. G. Schaeffer, and S. Pachnicke, "Neural networks based equalization of experimental transmission using the nonlinear fourier transformation," in *2020 European Conference on Optical Communications (ECOC)*, 2020.

[103] K.-D. Kammeyer and M. Bossert, Eds., *Nachrichtenübertragung*, 5th ed., ser. Studium. Wiesbaden: Vieweg + Teubner, 2011.

[104] Koch, J., Müller, J., Moscoso-Martir, A., Witzens, J. and Pachnicke, S., "Dwdm soliton transmission enabled by integrated photonics and nonlinear fourier transform," in *Photonic Networks; 20th ITG-Symposium*, 2019.

[105] M. Schetzen, *The Volterra and Wiener Theories of Nonlinear Systems.* New York: Wiley, 1980.

[106] Roi Rath, "Investigation of digital signal processing techniques for compensation of linear and nonlinear impairments in fiber-optic communication systems," Dissertation, Kiel University, Kiel, 2019.

[107] S. P. Lars Kruse, Ed., *EDFA Soft-Failure Detection and Lifetime Prediction based on Spectral Data using 1-D Convolutional Neural Network*, 2021.

[108] R. Weixer, J. Koch, P. Plany, S. Ohlendorf, and S. Pachnicke, "Mitigation of nonlinear impairments by using support vector machine and nonlinear volterra equalizer," *Applied Sciences*, vol. 9, no. 18, p. 3800, 2019. [Online]. Available: https://www.mdpi.com/532224

[109] R. Koch, S. Kuhl, R. M. Morais, B. Spinnler, W. Schairer, B. Sommernkorn-Krombholz, and S. Pachnicke, "Reinforcement learning for generalized parameter optimization in elastic optical networks," *Journal of Lightwave Technology*, vol. 40, no. 3, pp. 567–574, 2022. [Online]. Available: http://dx.doi.org/10.1109/jlt.2021.3123271

[110] Mihail Balanici and Stephan Pachnicke, "Hybrid electro-optical intra-data center networks tailored for different traffic classes," *Journal of Optical Communications and Networking*, vol. 10, no. 11, pp. 889–901, 2018.

[111] F. Musumeci, C. Rottondi, A. Nag, I. Macaluso, D. Zibar, M. Ruffini, and M. Tornatore, "An overview on application of machine learning techniques in optical networks," *IEEE Communications Surveys & Tutorials*, vol. 21, no. 2, pp. 1383–1408, 2019. [Online]. Available: http://dx.doi.org/10.1109/comst.2018.2880039

[112] T. A. Eriksson, H. Bulow, and A. Leven, "Applying neural networks in optical communication systems: Possible pitfalls," *IEEE Photonics Technology Letters*, vol. 29, no. 23, pp. 2091–2094, 2017. [Online]. Available: http://dx.doi.org/10.1109/lpt.2017.2755663

[113] Ian Goodfellow and Yoshua Bengio and Aaron Courville, *Deep Learning*. MIT Press, 2016.

[114] Christopher M. Bishop, *Pattern Recognition and Machine Learning*. New York: Springer, 2006.

[115] R. A. Minasian, "Photonic signal processing of microwave signals," *IEEE Transactions on Microwave Theory and Techniques*, vol. 54, no. 2, pp. 832–846, 2006. [Online]. Available: http://dx.doi.org/10.1109/tmtt.2005.863060

[116] ——, "Ultra-wideband and adaptive photonic signal processing of microwave signals," *IEEE Journal of Quantum Electronics*, vol. 52, no. 1, pp. 1–13, 2016. [Online]. Available: http://dx.doi.org/10.1109/jqe.2015.2499729

[117] A. Martir, J. Koch, O. Schulz, J. Mueller, A. Tabatabaei Mashayekh, A. Dipta Das, F. Merget, S. Pachnicke, and J. Witzens, "Silicon photonics integrated circuits for soliton based long haul optical communication," *Journal of Lightwave Technology*, p. 1, 2022. [Online]. Available: http://dx.doi.org/10.1109/jlt.2022.3170250

[118] Olaf Schulz, Jonas Koch, Alvaro Moscoso-Mártir, Jeremy Witzens, Stephan Pachnicke, "8-apsk transmission over 5400 km using a silicon photonics wdm nft soliton transmitter and nn-based equalization," in *27th OptoElectronics and Communications Conference/International Conference on Photonics in Switching and Computing*, 2022.

[119] Abdelsalam A. Aboketaf, Ali W. Elshaari, and Stefan F. Preble, "Optical time division multiplexer on silicon chip," *Optics Express*, vol. 18, no. 13, pp. 13 529–13 535, 2010.

[120] Jochem Verbist, Michael Vanhoecke, Mads Lillieholm, Srinivasan Ashwyn Srinivasan, Peter De Heyn, Joris Van Campenhout, Michael Galili, Leif K. Oxenløwe, Xin Yin, Johan Bauwelinck, and

Gunther Roelkens, "4:1 silicon photonic serializer for data center interconnects demonstrating 104 gbaud ook and pam4 transmission," *J. Lightwave Technol.*, vol. 37, no. 5, pp. 1498–1503, 2019.

[121] Leimeng Zhuang and Arthur J. Lowery, "Picosecond optical pulse processing using a terahertz-bandwidth reconfigurable photonic integrated circuit," *Nanophotonics*, no. 5, pp. 837–852, 0113. [Online]. Available: https://www.degruyter.com/document/doi/10.1515/nanoph-2017-0113/html

[122] H. Buelow et al, "Transmission of waveforms determined by 7 eigenvalues with psk-modulated spectral amplitudes," in *42nd European Conference on Optical Communication (ECOC)*, 2016.

[123] S. Gaiarin, F. Da Ros, N. de Renzis, E. P. da Silva, and D. Zibar, "Dual-polarization nfdm transmission using distributed raman amplification and nft-domain equalization," *IEEE Photonics Technology Letters*, vol. 30, no. 22, pp. 1983–1986, 2018. [Online]. Available: http://dx.doi.org/10.1109/lpt.2018.2874204

[124] G. Zhou, T. Gui, C. Lu, A. P. T. Lau, and P.-K. A. Wai, "Improving soliton transmission systems through soliton interactions," *Journal of Lightwave Technology*, vol. 38, no. 14, pp. 3563–3572, 2020. [Online]. Available: http://dx.doi.org/10.1109/jlt.2019.2932332

[125] J. Koch, S. Li, and S. Pachnicke, "Separation of bounded higher-order solitons by exploiting collisions in wdm transmission systems." in *44th European Conference on Optical Communication (ECOC)*, 2018.

[126] X. Yangzhang, V. Aref, S. T. Le, H. Bulow, and P. Bayvel, "400 gbps dual-polarisation non-linear frequency-division multiplexed transmission with b-modulation," in *44th European Conference on Optical Communication (ECOC)*, 2018.

[127] X. Yangzhang, S. T. Le, V. Aref, H. Buelow, D. Lavery, P. Bayvel, "Experimental demonstration of dual-polarization nfdm transmission with b-modulation," *IEEE Photonics Technology Letters*, vol. 31, no. 11, 2019.

[128] Tao Gui, Gai Zhou, Chao Lu, Alan Pak Tao Lau, and Sander Wahls, "Nonlinear frequency division multiplexing with b-modulation: Shifting the energy barrier," *Optics Express*, vol. 26, no. 21, pp. 27 978–27 990, 2018.

[129] S. Chimmalgi and S. Wahls, "Bounds on the transmit power of b-modulated nfdm systems in anomalous dispersion fiber," *Entropy*, vol. 22, no. 6, p. 639, 2020. [Online]. Available: https://www.mdpi.com/738072

[130] S. Wahls, S. T. Le, J. E. Prilepsk, H. V. Poor, and S. K. Turitsyn, "Digital backpropagation in the nonlinear fourier domain," in *16th International Workshop on Signal Processing Advances in Wireless Communications (SPAWC)*, 2015.

[131] A. Zazzi, J. Muller, M. Weizel, J. Koch, D. Fang, A. Moscoso-Martir, A. Tabatabaei Mashayekh, A. D. Das, D. Drays, F. Merget, F. X. Kartner, S. Pachnicke, C. Koos, J. C. Scheytt, and J. Witzens, "Optically enabled adcs and application to optical communications," *IEEE Open Journal of the Solid-State Circuits Society*, vol. 1, pp. 209–221, 2021. [Online]. Available: http://dx.doi.org/10.1109/ojsscs.2021.3110943

[132] P. De Koster, S. Wahls, "Dispersion and nonlinearity identification for single-mode fibers using the nonlinear fourier transform," *Journal of Lightwave Technology*, vol. 38, no. 12, pp. 3252–3260, 2020.

[133] P. De Koster, J. Koch, O. Schulz, S. Pachnicke, and S. Wahls, "Experimental validation of nonlinear fourier transform-based kerr-nonlinearity identification over a 1600 km ssmf link," in *Optical Fiber Communications Conference*, 2022.

Veröffentlichungen des Autors mit Angaben über die Höhe des Eigenanteils bei Publikationen/Manuskripten mit mehreren Autoren

Optical signal processing in the discrete nonlinear frequency domain, Optical Fiber Communication Conference (OFC), San Diego, 2018.

Autoren: S. Li, J. Koch, S. Pachnicke

Konzeptionierung	Planung	Durchführung	Manuskripterstellung
Mittel	Mittel	Hoch	Mittel

Separation of Bounded Higher-Order Solitons by Exploiting Collisions in WDM Transmission Systems, 44th European Conference on Optical Communication (ECOC), Rom, 2018.

Autoren: J. Koch, S. Li, S. Pachnicke

Konzeptionierung	Planung	Durchführung	Manuskripterstellung
Hoch	Mittel	Hoch	Mittel

Transmission of Higher Order Solitons Created by Optical Multiplexing, J. Lightwave Technol. vol. 37 no. 3, pp. 933–941, 2019, DOI: 10.1109/jlt.2018.2883826.

Autoren: J. Koch, S. Li, S. Pachnicke

Konzeptionierung	Planung	Durchführung	Manuskripterstellung
Mittel	Mittel	Hoch	Mittel

Equalization of Soliton Transmission Based on Nonlinear Fourier Transform using Neural Networks, 45th European Conference on Optical Communication (ECOC), Dublin, 2019.

Autoren: J. Koch, R. Weixer, S. Pachnicke

Konzeptionierung	Planung	Durchführung	Manuskripterstellung
Hoch	Hoch	Hoch	Hoch

Mitigation of Nonlinear Impairments by Using Support Vector Machine and Nonlinear Volterra Equalizer, Applied Sciences vol. 9 no. 18, 2019, DOI: 10.3390/app9183800.

Autoren: R. Weixer, J. Koch, P. Plany, S. Ohlendorf, S. Pachnicke

Konzeptionierung	Planung	Durchführung	Manuskripterstellung
Niedrig	Niedrig	Mittel	Niedrig

DWDM Soliton Transmission enabled by Integrated Photonics and Nonlinear Fourier Transform, Photonic Networks; 20th ITG-Symposium, Leipzig, 2019.

Autoren: J. Koch, J. Müller, A. Moscoso-Martir, J. Witzens, S. Pachnicke

Konzeptionierung	Planung	Durchführung	Manuskripterstellung
Hoch	Mittel	Hoch	Hoch

Neural Networks based Equalization of Experimental Transmission using the Nonlinear Fourier Transformation, 46th European Conference on Optical Communications (ECOC), Online, 2020.

Autoren: J. Koch, K. Chan, S. Kühl, C. G. Schäffer, S. Pachnicke

Konzeptionierung	Planung	Durchführung	Manuskripterstellung
Hoch	Hoch	Mittel	Hoch

Silicon Photonics DWDM NLFT Soliton Transmitter Implementation and Link Budget Assessment, European Conference on Integrated Optics (ECIO), Paris, France, 2020.

A. Moscoso-Martir, J. Koch, J. Müller, S. Sharif Azadeh, S. Pachnicke, J. Witzens

Konzeptionierung	Planung	Durchführung	Manuskripterstellung
Niedrig	Niedrig	Mittel	Niedrig

(Invited) Experimental Demonstration of Nonlinearity Compensation by Using SVM and Nonlinear Volterra Equalizer for 80 GBd DP-16-QAM, International Conference on Transparent Optical Networks (ICTON), Bari, Italy, 2020.

Autoren: R. Weixer, J. Koch, S. Ohlendorf, S. Pachnicke

Konzeptionierung	Planung	Durchführung	Manuskripterstellung
Niedrig	Niedrig	Mittel	Niedrig

Silicon Photonics DWDM NLFT Soliton Transmitter, Photonic Networks; 21st ITG-Symposium, Leipzig, 2020.

Autoren: J. Koch, A. Moscoso-Martir, J. Mueller, S. Pachnicke, J. Witzens

Konzeptionierung	Planung	Durchführung	Manuskripterstellung
Hoch	Hoch	Mittel	Hoch

(Invited) Signal Processing Techniques for Optical Transmission Based on Eigenvalue Communication, IEEE J. Sel. Top. Quant. Elect. (JSTQE), vol. 27, no. 3, May-June 2021, DOI: 10.36227/techrxiv.14258426.

Autoren: J. Koch, K. Chan, C. G. Schaeffer, S. Pachnicke

Konzeptionierung	Planung	Durchführung	Manuskripterstellung
Hoch	Hoch	Mittel	Mittel

Optically enabled ADCs and application to optical communications, IEEE Open J. Solid-State Circuits Society (OJ-SSCS), vol. 1, pp. 209-221, 2021.

Autoren: A. Zazzi, J. Müller, M. Weizel, J. Koch, D. Fang, A. Moscoso-Mártir, A. T. Mashayekh, A. D. Das, D. Drayß, F. Merget, F. X. Kärtner, S. Pachnicke, C. Koos, J. C. Scheytt, J. Witzens

Konzeptionierung	Planung	Durchführung	Manuskripterstellung
Niedrig	Niedrig	Niedrig	Niedrig

Experimental Demonstration of a Silicon-Photonics WDM NFT Soliton Transmitter, Optical Fiber Communication Conference (OFC), San Francisco, USA, June 2021.

Autoren: J. Koch, A. Moscoso-Mártir, J. Müller, A. Tabatabaei Mashayekh, A. D. Das, F. Merget, S. Pachnicke, J. Witzens

Konzeptionierung	Planung	Durchführung	Manuskripterstellung
Hoch	Hoch	Mittel	Hoch

(Invited) Silicon Photonics Integrated Circuits for Nonlinear Fourier Transform Based Transmission, 47th European Conference on Optical Communication (ECOC), Bordeaux, France, September 2021.

Autoren: A. Moscoso-Mártir, J. Koch, J. Müller, A. Tabatabaei Mashayekh, A. D. Das, F. Merget, S. Pachnicke, J. Witzens

Konzeptionierung	Planung	Durchführung	Manuskripterstellung
Mittel	Niedrig	Mittel	Niedrig

Experimental Investigation of Nonlinear Fourier Transform Based Fibre Nonlinearity Characterisation, 47th European Conference on Optical Communication (ECOC), Bordeaux, France, September 2021.

Autoren: P. de Koster, J. Koch, S. Pachnicke, S. Wahls

Konzeptionierung	Planung	Durchführung	Manuskripterstellung
Niedrig	Niedrig	Mittel	Niedrig

(Invited) Silicon Photonics Integrated Circuits for Soliton Based Long Haul Optical Communication, IEEE J. Lightw. Technol. (JLT), 2022.

Autoren: A. Moscoso-Mártir, J. Koch, O. Schulz, J. Müller, A. Tabatabaei Mashayekh, A. D. Das, F. Merget, S. Pachnicke, J. Witzens

Konzeptionierung	Planung	Durchführung	Manuskripterstellung
Mittel	Mittel	Mittel	Mittel

Experimental validation of nonlinear Fourier transform-based Kerr-nonlinearity identification over a 1600km SSMF link, Optical Fiber Communication Conference (OFC), San Diego, USA, March 2022.

Autoren: P. de Koster, J. Koch, O. Schulz, S. Pachnicke, S. Wahls

Konzeptionierung	Planung	Durchführung	Manuskripterstellung
Niedrig	Niedrig	Mittel	Niedrig

8-APSK Transmission over 5400 km using a Silicon Photonics WDM NFT Soliton Transmitter and NN-based Equalization, Optoelectronics and Communications Conference (OECC 2022), Toyama, Japan, July 2022.

Autoren: O. Schulz, J. Koch, A. Moscoso-Mártir, J. Witzens, S. Pachnicke

Konzeptionierung	Planung	Durchführung	Manuskripterstellung
Mittel	Mittel	Mittel	Niedrig